Modelling of a Small Electric Aircraft Pipistrel Velis Electro

by

Lekha Dasari Murugappa

A thesis

presented to the University of Waterloo

in fulfillment of the

thesis requirement for the degree of

Master of Applied Science

in

Electrical and Computer Engineering

Waterloo, Ontario, Canada, 2026

© Lekha Dasari Murugappa 2026

Author's Declaration

This thesis consists of material all of which I authored or co-authored: see Statement of Contributions included in the thesis. This is a true copy of the thesis, including any required final revisions, as accepted by my examiners.

I understand that my thesis may be made electronically available to the public.

Statement of Contributions

The flight data of the Pipistrel Velis Electro used in Chapters 3 and 4 were contributed by the Waterloo Wellington Flight Center. I developed and implemented the methodology, built the models, conducted the simulations, and generated the results. This thesis and the associated conference papers were written by me under the supervision of Dr. Mehrdad Kazerani.

Abstract

Transportation electrification has become an active area of research and development in academia and industry, with a strong focus on decarbonizing the sector to move toward a more sustainable environment. As an important player in the global sustainable transportation movement, the aviation industry is also witnessing accelerated efforts towards electrification. This transition comes with many challenges in terms of battery performance, aircraft flight range, and operational safety. Therefore, development of comprehensive simulation models, that replicate the behavior of an actual aircraft, is essential for studying the system's overall performance. Such models provide invaluable insights into battery health, methods to extend range, and ways to improve flight missions for more efficient battery usage. This thesis aims to develop a mathematical model of the aircraft propeller and a simulation model of the electric powertrain consisting of the battery pack, inverter, and motor. The aircraft under study is the Pipistrel Velis Electro, a two-seater, type-certified, fully electric aircraft. Two methods are proposed to model the propeller behavior: one based on the aircraft equations of motion and the other based on the motor power command. Both methods compute the thrust, motor rotational speed, and load torque for each phase of the flight using different input sets, and these outputs are supplied to the powertrain model. Two modes of operation are considered for the powertrain: an autopilot flight mode and a pilot-controlled mode, with phase detection between powered and glide phases. The simulations are validated by comparing the results with actual Velis Electro flight data obtained from the Waterloo Wellington Flight Center.

Acknowledgements

First and foremost, I would like to express my sincere and deepest gratitude to my supervisor, Professor Mehrdad Kazerani, for his constant guidance, insightful advice, and unwavering support throughout my MASc studies at the University of Waterloo. His technical expertise, trust in my work, and thoughtful mentorship have been instrumental in shaping this research. I am truly extremely grateful and fortunate for the opportunity to learn under his supervision, both academically and professionally.

I would also like to acknowledge the Waterloo Wellington Flight Center for providing the flight data used in this study, which made the experimental validation of this research possible.

I extend my heartfelt thanks to my colleagues, Nasrin Einabadi and Miswar A. Syed, for their valuable discussions, constructive suggestions, and continued cooperation during this work. I am also grateful to all my friends for their encouragement and companionship in my endeavors.

Finally, I owe my deepest gratitude to my parents, Mr. Murugappa Dasari Mani and Mrs. Narmadha Dasari Murugappa, and to my brother, Harrish, for their unconditional love, patience, and constant support. Their belief in me has been my greatest source of strength and motivation. It is my sincere hope to make them proud in all that I pursue.

Dedication

This work is dedicated to:

- My parents, whose love, resilience, and quiet sacrifices form the foundation of everything I do.
- My brother, whose constant presence and unwavering faith in me mean more than words can express.
- My supervisor, Professor Mehrdad Kazerani, who believed in me and helped me pave the path toward my career in electric aviation, a field that has always been my ambition.
- My circle of friends, who stood beside me with patience, laughter, and steady support.
- Every individual who, in ways big and small, strengthened my spirit and shaped my path.

Table of Contents

Author's Declaration ii

Statement of Contributions iii

Abstract iv

Acknowledgements v

Dedication vi

List of Figures x

List of Tables xiii

List of Abbreviations xiv

Chapter 1 Introduction 1

1.1 Motivation 3

1.2 Research Objectives 5

1.3 Thesis Organization 5

Chapter 2 Literature Review and Background Overview 7

2.1 Literature Review 7

2.1.1 Introduction to Electric Aircrafts 7

2.1.2 Propulsion Architectures 8

2.1.3 Aerodynamic Propeller Based Modelling 10

2.1.4 Electric Powertrain and Battery 11

2.2 Background Overview 16

2.2.1 Aerodynamics Terms 16

2.2.2 Aircraft Equations of Motion (EOM) 20

2.2.3 Translational Motion 25

2.2.4 Rotational Motion 27

Chapter 3 Aircraft Aerodynamic Analysis 30
3.1 EOM-Based Approach 30
3.1.1 Methodology 30
3.1.2 Propeller Study 34
3.1.3 Dataset Description 38
3.2 Motor Power Command (MPC) Approach 47
3.2.1 Methodology 48
3.2.2 Simulation Results 52
3.2.3 RPM with Phase Regions 62
3.3 Conclusion 64
Chapter 4 Electric Powertrain Model 66
4.1 Pipistrel Velis Electro Powertrain Configuration 66
4.1.1 Battery Packs 66
4.1.2 Inverter 69
4.1.3 State of Health (SoH) Evaluation 69
4.1.4 Permanent Magnet Synchronous Motor (PMSM) 70
4.1.5 Field-Oriented Control 72
4.2 Methodology 74
4.2.1 Autopilot Flight Mode 75
4.2.2 Pilot-Controlled Mode 77
4.3 Simulation Results 78
4.3.1 Autopilot Flight Mode Simulation Results 78
4.3.2 Pilot-Controlled Mode Simulation Results 88
4.3.3 Pilot-Controlled Mode Simulation Results for an Additional Flight Mission 96

4.4 Conclusion 103
Chapter 5 Conclusions and Recommendations for Future Work 104
5.1 Conclusions 104
5.2 Recommendations for Future Work 105
References 106

List of Figures

Figure 2.1 Earth frame (stationary). 20
Figure 2.2 Body frame (attached to the aircraft). 21
Figure 2.3 Yaw angle. 22
Figure 2.4 Pitch angle. 23
Figure 2.5 Roll angle. 24
Figure 3.1 Flight stages. 31
Figure 3.2 Flight phase identification. 31
Figure 3.3 Propeller coefficients versus advance ratio. 35
Figure 3.4 Propeller efficiency versus aircraft speed in knots. 35
Figure 3.5 Rotational speed and torque estimation methodology. 37
Figure 3.6 Aircraft flying altitude with respect to the airport ground. 39
Figure 3.7 Magnitude of aircraft forward velocity (Indicated Air Speed, IAS). 39
Figure 3.8 Ground Speed. 40
Figure 3.9 Aircraft velocity along the x-axis (longitude). 40
Figure 3.10 Aircraft velocity along the y-axis (latitude). 41
Figure 3.11 Aircraft velocity along the z-axis (normal). 41
Figure 3.12 Pitch angle profile. 42
Figure 3.13 Roll angle profile. 42
Figure 3.14 Yaw angle profile. 43
Figure 3.15 Angle of attack. 43
Figure 3.16 Estimated propeller thrust. 45
Figure 3.17 Estimated propeller torque. 45
Figure 3.18 Estimated propeller and motor rotational speed. 46
Figure 3.19 Actual propeller and motor rotational speed. 46
Figure 3.20 Comparison between actual rotational speed and estimated rotational speed (after considering propeller efficiency). 47
Figure 3.21 Comparison between commanded and shaft power. 47
Figure 3.22 Pilot power command for normal flight. 53
Figure 3.23 Aircraft altitude for normal flight. 54
Figure 3.24 Aircraft's Indicated Air Speed (IAS) and True Air Speed (TAS) for normal flight. 54

Figure 3.25 Comparison between actual and estimated motor rotational speed for normal flight. 55
Figure 3.26 Estimated propeller thrust for normal flight. 56
Figure 3.27 Estimated and actual load torque for normal flight. 57
Figure 3.28 Pilot power command for touch-and-go flight. 58
Figure 3.29 Aircraft altitude for touch-and-go flight. 59
Figure 3.30 Aircraft IAS and TAS for touch-and-go flight. 59
Figure 3.31 Comparison between actual and estimated motor rotational speed for touch-and-go flight. 60
Figure 3.32 Estimated propeller thrust for touch-and-go flight. 61
Figure 3.33 Estimated and actual load torque for touch-and-go flight. 62
Figure 3.34 Normal flight RPM with phase distinction. 63
Figure 3.35 Touch-and-go flight RPM with phase distinction. 64
Figure 4.1 Battery model. 68
Figure 4.2 SoH model in Simulink. 70
Figure 4.3 Inverter and PMSM Simulink model. 72
Figure 4.4 Field-oriented control architecture. 74
Figure 4.5 Powertrain model integrated with aerodynamic model. 74
Figure 4.6 Autopilot Flight Mode Simulink Model. 76
Figure 4.7 Reference and simulated (estimated) motor speed in rpm. 79
Figure 4.8 Electromagnetic torque and load torque. 80
Figure 4.9 Front Battery Pack's SoC and OCV. 81
Figure 4.10 Rear Battery Pack's SoC and OCV. 82
Figure 4.11 DC link voltage. 84
Figure 4.12 Stator currents (I_q and I_d). 85
Figure 4.13 Inverter phase-to-phase voltages and currents. 86
Figure 4.14 SoH of front and rear battery packs. 87
Figure 4.15 Power commanded by the pilot in W. 88
Figure 4.16 Actual and simulated (estimated) motor speed in rpm. 89
Figure 4.17 Electromagnetic torque and load torque. 90
Figure 4.18 Actual and estimated SoC with OCV for both battery packs. 92
Figure 4.19 DC Link Voltage in pilot-controlled mode. 93

Figure 4.20 Inverter phase-to-phase voltages and currents in pilot-controlled mode. 94
Figure 4.21 SoH of front and rear battery packs in pilot-controlled mode..... 95
Figure 4.22 Aircraft altitude. 96
Figure 4.23 Aircraft indicated airspeed and true airspeed. 96
Figure 4.24 Power commanded by the pilot. 97
Figure 4.25 Estimated and actual RPM for additional profile. 97
Figure 4.26 Actual load torque and mean electromagnetic torque. 98
Figure 4.27 DC link voltage for additional profile. 98
Figure 4.28 SoC and OCV of front battery pack for additional profile. 99
Figure 4.29 SoC and OCV of rear battery pack for additional profile. 100
Figure 4.30 Inverter voltages and current for additional profile. 101
Figure 4.31 SoH of front and rear battery packs for additional flight. 102

List of Tables

Table 4.1 Battery Pack Specifications [50] 67
Table 4.2 Velis Electro PMSM Specifications [50]. 71
Table 4.3 Controller Parameters in Autopilot Flight Mode..... 75

List of Abbreviations

EOM Equations of Motion

FOC Field-Oriented Control

IAS Indicated Airspeed

GS Ground Speed

MPC Motor Power Command

OCV Open Circuit Voltage

PMSM Permanent Magnet Synchronous Motor

QNH Altimeter Setting (Pressure at Mean Sea Level)

RPM Motor Rotational Speed in Revolutions per Minute

SoC State of Charge

SoH State of Health

SVM Space Vector Modulation

TAS True Airspeed

Chapter 1
Introduction

Although aviation only contributes to about 3% of the global CO_2 emissions, the industry's total effects on the climate are much larger. Climate change is caused not only by CO_2, but also other greenhouse gases and non-CO_2 effects (e.g., nitrogen oxides, water vapor at altitude, contrails) that accelerate global warming [1]. The expected growth in air travel worldwide, especially in emerging economies, raises potential for aviation emissions to triple by 2050, a projection that has raised concerns amongst climate scientists, environmental groups, and international policymakers [2].

According to the Intergovernmental Panel on Climate Change (IPCC), this is one of the most challenging sectors to decarbonize. Long-distance flights require so much energy to operate that cannot be fulfilled due to the limitations in the scalable, low-carbon technology alternatives that are presently available. Aviation is unique, in that it is international, requiring a globally coordinated strategy.

In this regard, some efforts have been initiated internationally. The International Civil Aviation Organization (ICAO), a member of the United Nations, has played an important role in the efforts made to address emissions reductions. In 2017, ICAO established the Carbon Offsetting and Reduction Scheme for International Aviation (CORSIA) to maintain net CO_2 emissions from international flights at the same level as the year 2020. Under this policy, airlines will need to purchase carbon credits to offset emissions that exceed the baseline [3]. CORSIA is voluntary until 2026 (initial phases have already occurred) and will become mandatory for most nations in 2027.

In addition, the ICAO introduced the world’s first international aircraft CO_2 emissions certification standard in 2020 for new aircraft type designs, with compliance extended to in-production aircraft from 2023 onward [4]. This regulation establishes performance-based limits on fuel burn and CO_2 emissions per unit of transport work, while allowing manufacturers flexibility in meeting the standard through alternative technologies and design improvements. Aviation emissions are also capped in the EU's Emissions Trading System (ETS), limiting the total amount of emissions by requiring airlines to purchase allowances that are the same as emissions generated [5].

In efforts such as the Fit for 55 package and the European Green Deal [6], the EU has requested further reduced emission limits, a gradual reduction in free allowances, and requests for the use of sustainable aviation fuel (SAF). The US Environmental Protection Agency (EPA) released its first GHG emissions standards for aircraft in 2021, directly modeled on some of ICAO's practices and general protocol for

baseline requirements [2]. The EPA implemented a federal measure that is consistent with global standards and may serve as a foundation for tightening domestic policies in future revisions.

In addition, international climate agreements such as the Paris Agreement, which establish a framework for coordinated action across related nations, contribute to climate action by drawing attention to the need for decarbonization in this sector. Although the Paris agreement does not specify emissions from international aviation in national targets back to a base year within the framework, there is growing recognition for the international aviation sector as a contributor to climate change. Therefore, the expectation is for countries to include emissions from international aviation in their broader national climate commitment planning [6].

As part of the movement to reduce aviation emissions, there has been increasing interest in electric propulsion systems. Past advancements in electric propulsion systems generated a prototype called the More Electric Aircraft (MEA), which harnesses electric power for non-propulsive applications while replacing hydraulic and pneumatic systems [12]. Whereas MEA architectures are concerned with electrifying individual systems, such as flight controls, de-icing, and cabin pressure systems, fully electric aircraft are an engineered solution where the entire propulsion system is replaced by an electric motor and powered by batteries [9]. This eliminates combustion emissions during flight and reduces mechanical complexity [7], [10].

The electric motors used in aviation typically operate at very high efficiencies (well above 90%) compared with efficiencies of 30-40% for internal combustion engines. Assuming the electric motor is sized properly, electric motors do not have to work as hard as internal combustion engines, and they do not need to contain subsystems including fuel delivery, exhaust, and ignition, which reduces maintenance demands and weight [7], [14]. Given these features, electric propulsion systems are positioned to advantageously replace internal combustion engines for small-scale, low-energy demand (i.e., short range) flights where electric infrastructure could be accommodated, and where charging operations would not disrupt scheduling.

However, battery technology continues to be the limiting factor. Commercially available lithium-ion cells are typically used in aviation and offer specific energy levels of 250-300 Wh/kg (watt-hours per kilogram), which is very limited compared with what aviation fuels offer [11], [13]. Electric aircrafts are now limited by total time in flight, payload, and operational mission flexibility. Thermal management and charging time also represent practical limitations in scaling operations beyond local

or scheduled usage. Up to this point, most fully electric aircrafts developed for certification and operation have only been in the light aircraft category due to size and weight restrictions. Light aircraft platforms commonly employ fixed-pitch propellers coupled to a single electric motor, a configuration that remains mechanically simple and aligns well with the typical torque characteristics of electric propulsion systems. While variable pitch propellers are used in larger or more complex aircrafts, they will not be considered in this study [13], [14].

Typical electric propulsion configuration consists of a battery pack, an inverter, an electric motor, and a propeller, along with support systems including a battery management system and thermal management system. Researchers have explored distributed electric propulsion (DEP) with more than one motor placed along the fuselage to optimize both aerodynamic efficiency and control authority [8], [11]. However, most certified operational electric aircrafts use a single motor for mechanical simplicity and reliability [13].

1.1 Motivation

Modeling electric aircraft accurately, over a complete mission profile, is important for capturing the coupled dynamics of the electric motor, power electronic converters and battery pack, and assessing their effect on the battery state of charge (SoC) and state of health (SoH). In [15], a co-simulation framework was proposed to support analysis of an electric aircraft with distributed propulsion modeled from the NASA X-57 Maxwell. The system includes average and detailed switching models of the motor, inverter, battery and propeller, and connects them all with a simplified flight dynamics model. The model calculated both thrust and load torque for a motor but fixed the coefficients for thrust and torque of the propeller. As the thrust and torque coefficients are functions of flight condition, and most notably the advance ratio, this is a limitation in accurately capturing the dynamic behavior of the propeller, particularly when subjected to varying aerodynamic loads.

In [16], an experimentally validated hybrid electric propulsion system (HEPS) was created with a test bench setup with a parallel ICE-electric configuration. A Simulink model of the physical system was produced and validated with measured data. The experimental setup and simulation platform showed similar characteristic behaviour in predicting powertrain energy flow and motor response. However, this model focuses on steady-state powertrain-level analysis and does not include aerodynamic forces or how flight dynamics influence propulsion demand. The result is that it cannot predict how changes in mission profiles lead to battery depletion or torque requirements.

A contrasting approach taken in [17] was to size batteries and estimated energy for small all-electric and electric vertical take-off and landing (eVTOL) aircraft using real airport operational data. This analysis models each of the discrete phases of flight, which include takeoff, climb, cruising, descent, and reserve, to estimate energy demand based on a reference aircraft model. While this approach captures the high energy demands of takeoff, it assumes that the aircraft is operating from a steady-state condition within a phase and does not model transitions. The combined CC-CV battery charging model and power estimates provide the ability to assess charging infrastructure needs, but it does not enable transient-level propulsion system analysis and dynamic flight characteristics.

In [18], a similar approach was taken in developing a trajectory-based energy management simulation. A six-degree-of-freedom flight dynamics model was combined with surrogate models of the propulsion system. The study estimated SoC, thermal states, and energy usage for an electric aircraft over full mission trajectories using the Pipistrel Velis Electro as a reference. Nevertheless, the motor, inverter, and propeller were not modeled from first principles; rather, the motor speed and torque were modeled with a response surface surrogate model that was produced from flight data. While this approach allowed fast computation, the omission of a physics-based propeller model limited the accuracy of torque and thrust estimation, especially during maneuvering or unsteady conditions where aerodynamic coupling becomes more significant.

These studies highlight the need for a more integrated modeling approach that couples aerodynamic and powertrain behavior in a mission-specific context. The co-simulation model presented in [15] included the integration of flight and electrical systems, but it assumed constant aerodynamic coefficients. The experimental validation in [16] informs the powertrain level results; however, it cannot utilize flight dynamics. The energy analysis aspect in [17] is useful for sizing and infrastructure planning but also assumes steady-state conditions. The trajectory simulation in [18] captures a dynamic motion model unlike the previous efforts; however, it also relies on surrogate estimations for the propulsion quantities presented for analysis. This motivates the development of an integrated approach that uses aerodynamic modeling to compute thrust, load torque, and rotational speed from real flight data, enabling more accurate analysis of powertrain behavior and battery usage across mission scenarios.

1.2 Research Objectives

- To develop mathematical models for estimating propeller behavior.
    - Create an aerodynamic model using aircraft equations of motion with inputs of altitude, velocity, and orientation angles.
    - Implement a second method based on the motor power command together with altitude and velocity.
    - Use both methods to estimate thrust, load torque, and propeller rotational speed.
- To build an electric powertrain model of the aircraft in MATLAB Simulink.
    - Simulate the powertrain in two modes of operation:
        - Autopilot mode: give the reference rotational speed and load torque from the aerodynamic model to the powertrain controllers.
        - Pilot-controlled mode: use the motor power command from flight data and the load torque from the aerodynamic model. Include a mode detection step to identify powered or glide operation and set the speed reference accordingly.
- To study battery performance across the mission.
    - Examine the state of charge, voltage, and current for all segments of the simulation.
- To compare the simulated results with actual flight data.
- Assess how accurately the propeller models and the powertrain model replicate the real behavior of the aircraft.

1.3 Thesis Organization

- Chapter 1 presents the introduction, motivation, and objectives of the study and outlines the overall structure of the thesis.
- Chapter 2 reviews the literature on electric propulsion, propeller modelling, powertrain simulation, and battery performance studies. It also provides a background overview of aircraft aerodynamics.
- Chapter 3 describes the mathematical models used for the propeller analysis. It explains the equations of motion, the methodology used for the aerodynamic and power command approaches, and presents the simulation results for two flight profiles. These include a normal flight and a touch-and-go flight.

- Chapter 4 presents the electric powertrain model developed in MATLAB Simulink. It explains the two modes of operation, namely the autopilot mode and the pilot-controlled mode, and includes the simulation results for a normal flight profile in both modes.
- Chapter 5 provides the conclusions of the study along with recommendations for future work.

Chapter 2
Literature Review and Background Overview

This chapter provides an overview of the literature and background relevant to electric aircraft propulsion. It introduces the development of electric and hybrid propulsion architectures, emphasizing their role in improving efficiency and reducing emissions compared to conventional systems. Previous studies on aerodynamic and propeller-based modelling are discussed to establish the foundation for estimating thrust, torque, and rotational speed. The review also highlights research on electric powertrain and battery technologies that enable sustainable flight. In addition, the fundamental concepts of aircraft dynamics, including aerodynamic terminologies and equations of motion governing translational and rotational movement, are summarized. Together, these sections provide the theoretical and contextual basis for the modelling and analysis presented in the following chapters.

2.1 Literature Review

2.1.1 Introduction to Electric Aircrafts

The aerospace industry is moving toward electrification mainly to reduce emissions, improve fuel economy, and lower running costs, with the side benefit of lowering noise. One of the first steps in this direction has been replacing mechanical, hydraulic, and pneumatic subsystems with electrical ones. This is what is generally meant by the More Electric Aircraft (MEA) concept. As the degree of electrification increases, systems such as actuation, environmental control, de-icing, and braking are electrified and their dependence on traditional methods are reduced. At the same time, the architecture of the aircraft power system itself has been changing. Older constant-voltage, constant-frequency networks (400 Hz) are being phased out and replaced by constant-voltage, variable-frequency supplies in the range of 115–230 V and 350–800 Hz. The benefit is that the heavy mechanical gearbox can be removed, although this comes at the cost of much greater dependence on power electronics to handle conversion and regulation [21].

MEA is not the final stage of electrification but rather an intermediate step. It can reduce the overall weight of the aircraft, simplify the system layout, and improve reliability and ease of maintenance. For example, hydraulic actuators are now being replaced by electro-hydrostatic or electromechanical actuators. These eliminate central hydraulic lines and in practice provide better fault tolerance [21]. The

Boeing 787 is often cited in this context because of using electrically driven compressors for cabin pressurization, starter-generators for the main engine instead of pneumatics, and remote distribution units that reduce wiring, weight, and maintenance requirements. The Airbus A350 shows a similar trend, making use of electrical braking and an advanced electrical environmental control system [19][20].

Research and development efforts are also focused on Hybrid-Electric Aircraft (HEA) and All-Electric Aircraft (AEA). In a hybrid arrangement, the engines still provide thrust but also generate electrical power for motors. In an all-electric design, propulsion is provided entirely by motors powered from onboard energy storage. These directions also introduce the concept of distributed propulsion, meaning that multiple electric propellers can be positioned along the wing to improve aerodynamic performance [20]. Still, moving from concept demonstrations to large commercial aircraft is not straightforward. Battery energy density is still too low to make long-range all-electric flight realistic, and both electric machines and power converters face limitations in terms of their power density and reliability [21][22]. Work is ongoing to address these issues; this includes the use of wide-bandgap semiconductor materials such as SiC and GaN, along with modular multiphase drives and smarter power distribution systems (PDS) [19][21].

2.1.2 Propulsion Architectures

In general, aircraft propulsion systems can be divided into two main categories: conventional combustion engine-based and electrified powertrain-based. Electrified powertrain-based propulsion systems can be further classified based on their powertrain configuration and the role of electricity in generating thrust. The main types include all-electric, turbo-electric, and hybrid-electric propulsion. The all-electric configuration relies entirely on batteries or fuel cells as the source of electrical energy, whereas the hybrid-electric configuration combines batteries or fuel cells with gas turbine engines, allowing both systems to contribute to propulsion. The turbo-electric configuration, on the other hand, consists of a gas turbine coupled with an electric generator that converts the fuel's chemical energy first into mechanical power and then into electrical energy to drive the electric propulsors [23].

Hybrid-electric systems can be arranged in series or parallel forms depending on how the electrical and mechanical energy sources are connected. In recent years, new developments such as distributed electric propulsion (DEP) and boundary layer ingestion have been introduced, both of which have shown potential for improving propulsive efficiency. While both hybrid-electric and all-electric

configurations depend on batteries, which are still limited by the current stage of battery energy density research, the turbo-electric system does not rely on batteries for propulsion. This makes it more attractive for near term applications since it offers a practical path toward electrified aviation while battery technology continues to advance [24].

The work in [8] reviews the recent progress in (DEP) systems, focusing on turboelectric, hybrid electric, and all-electric configurations. It highlights the main advantages of DEP, such as improved aerodynamic efficiency, noise reduction, and flexibility in integrating technologies like boundary-layer ingestion. The authors also discuss electrical architectures, cryogenic systems, and energy-storage challenges. While presenting a comprehensive understanding of DEP developments, the review notes ongoing issues related to system weight, battery limitations, and high-voltage power management that must be addressed for large-scale adoption.

The authors of [25] investigate the aerodynamic performance of a general aviation aircraft equipped with multiple distributed electric propellers mounted along the wing's leading edge. Using computational simulations, they examine how the propeller slipstream affects lift and drag characteristics and references the NASA X-57 Maxwell as a benchmark for DEP design. The results show that distributed propulsion enhances lift and improves the lift-to-drag ratio, especially during take-off and landing. However, the work is limited to steady-state numerical analysis and does not account for structural or energy-system integration, which are key challenges for practical implementation.

In [26], the authors develop and validate a six-degree-of-freedom dynamic model for a small unmanned aircraft featuring distributed electric propulsion. The @AIR platform uses several wing-mounted electric motors to analyze aerodynamic interactions and control performance. Flight tests confirmed that DEP can improve control responsiveness and fault tolerance. Nonetheless, the study is constrained by low-fidelity modelling and limited aerodynamic coupling, indicating the need for higher-accuracy simulations and broader flight testing to better represent DEP dynamics.

The study reported in [16] develops an experimentally validated hybrid electric propulsion model that combines a small internal combustion engine with an electric motor operating in a parallel configuration. The authors emphasize a realistic modelling approach by deriving system parameters from laboratory measurements of engine fuel consumption, motor efficiency, and battery response instead of relying on idealized assumptions. This gives the model practical value and demonstrates how

the power sources share load power during different modes of operation such as motor assist, engine only, and regenerative charging. The validation using a short mission profile confirms that the simulation can reproduce observed behaviour with reasonable accuracy.

The novelty of the work reported in [16] lies in its systematic integration of experimental data into a complete propulsion framework rather than treating each component separately. However, the model remains restricted to steady operating conditions, and its transient response during rapid power transitions is not explored. The experimental setup does not include the influence of cooling variations or longer endurance cycles, both of which can affect performance and efficiency. Extending validation to cover wider ranges of torque and speed variations, and incorporating temperature-dependent effects would make the model more comprehensive and representative of real hybrid aircraft operations.

2.1.3 Aerodynamic Propeller Based Modelling

In [27], a comprehensive dynamic model was developed for an electric propulsion system consisting of a battery, an electronic speed controller, a brushless DC motor, and a propeller. Each component was represented by its governing physical equations, allowing transient electrical and mechanical behaviors to be simulated in an integrated framework. The propeller was modeled using thrust and torque coefficients dependent on motor speed and airspeed, providing an effective steady-state load representation. However, the formulation assumes quasi-steady aerodynamic response and does not dynamically update the torque with changing flight conditions. Implementing a continuously updated thrust–torque balance that solves for motor speed from aerodynamic equilibrium, would enhance the model's accuracy for transient powertrain simulations.

The authors of [28] introduced an analytical method to estimate thrust, torque, and efficiency of micro-scale propellers operating at low Reynolds numbers. The model is computationally efficient and provides reasonable thrust predictions using simplified aerodynamic relationships. Although it offers good performance for small-scale applications, it treats thrust and torque as independent aerodynamic quantities, neglecting the influence of propeller load on motor speed and power demand. The absence of this coupling limits the predictive accuracy for systems featuring interdependent motor dynamics and aerodynamic behavior.

Reference [29] proposed a mathematical model and control strategy for an electric aircraft in which propeller aerodynamics are directly linked to motor torque control through nonlinear functions of the advance ratio. The formulation demonstrated high accuracy in thrust control and rapid response due to

the electric motor's fast torque adjustment capability. The results confirmed that the dynamic coupling between motor torque and propeller thrust enhances response smoothness compared to conventional systems. Nevertheless, the aerodynamic modeling remains simplified, as airspeed and altitude variations are not fully integrated into the coefficient calculations. Including dynamic updates of thrust and torque coefficients with airspeed variation would make the approach more robust across multiple flight phases.

A combined propulsion concept is introduced in [30] that employs both an electrically driven propeller and powered wheels to maintain total thrust during ground acceleration. The coordinated control between the two systems demonstrated improved acceleration uniformity and traction stability on low-friction surfaces. However, the aerodynamic portion of the model remains basic, using constant propeller coefficients that do not reflect variations in load torque or rotational speed. This restricts the model's ability to represent the changing aerodynamic demand placed on the motor during acceleration. Developing a variable-coefficient representation that captures load variation with rotational speed would enhance its accuracy in predicting power distribution and thrust balance.

A nonlinear six-degree-of-freedom model for a propeller-driven cargo aircraft is developed in [31] by combining aerodynamic data derived from empirical correlations and wind tunnel experiments. The study successfully integrates aerodynamic and stability derivatives to evaluate aircraft behavior under steady conditions. However, the propeller performance is modeled through static thrust coefficients without establishing a dynamic relationship between torque, propeller speed, and aerodynamic loading. This limitation reduces the model's ability to reflect changes in propeller behavior under varying flight conditions or power demand.

2.1.4 Electric Powertrain and Battery

The authors in [32] present a detailed model of a multi-phase, multilevel powertrain designed specifically for full electric aircraft. The architecture integrates multiple inverter stages feeding independent motor phases, enabling redundancy and fault tolerance while improving power distribution efficiency. The paper emphasizes a modular modeling approach that couples DC energy sources with high-frequency pulse width modulation (PWM) inverters and field-oriented-controlled permanent magnet motors. The proposed control framework ensures smooth torque sharing among phases, improving reliability in fault conditions. This approach provides valuable insight into how distributed-phase systems can maintain propulsion stability even under inverter or phase failure scenarios. A key

strength of this model lies in its focus on maintaining torque symmetry and minimizing current ripple across multi-level converters.

A complete permanent magnet synchronous motor (PMSM) with electrical and mechanical equations, Park and Clarke transforms, and a field-oriented control (FOC) scheme driven by space vector modulation is modelled and simulated in Simulink [33]. The model is validated by signal injection and shows good tracking of commanded torque and speed, which is useful for sizing controllers that must follow a measured dataset. The authors also document the simplifying assumptions used to keep the PMSM tractable, which makes the control behavior easy to reproduce in a propulsion model. A practical extension for propulsion would be to excite the model with time series of bus voltage, torque command, and airspeed derived from a flight segment and then report a point-by-point comparison of predicted motor speed, current, and electrical power.

The work in [34] implements a battery, an inverter, and a three-phase motor, with control in dq domain, in a hardware in the loop setup, so that torque and speed commands can be exercised in real time. The model includes battery state equations, dq frame motor dynamics, and PWM gating, with transient currents and voltages reported under acceleration and regenerative braking modes of operation. Although the target application is automotive, the structure is directly useful for an aircraft powertrain controller because it dissociates the controller from the physical motor while preserving timing, gating, and current loop behavior. Replacing the road load with a thrust and torque law based on advance ratio would let the same real time bench replay a flight profile and compare predicted speed to measured data.

The study in [35] fuses pitot tube airspeed and inertial measurement unit data through body and navigation frame equations to estimate velocity and attitude in real time. The observer uses aerodynamic relationships to correct drift and produce stable airspeed, pitch, and roll estimates during maneuvers. While this is not a propulsion model, the formulation is directly useful to drive a propeller load law and to reconstruct advance ratio from measured states. That allows a powertrain model to compute propeller torque consistently with the estimated airspeed and altitude. The paper’s emphasis on body frame definitions, transformation consistency, and measured air data makes it a strong reference when building the signal path that links flight states to propulsion load.

The authors of [36] connect a proton exchange membrane fuel cell stack, a lithium battery, and the propulsion drive through DC/DC conversion and an energy management system (EMS). The controller

allocates power between sources to maintain bus voltage and motor demand while improving endurance. The motor side uses FOC with a speed command, so the study contains the core elements needed to replay a mission and record power flow among sources. The modeling is system level, and degradation or slow dynamics of the fuel cell are treated in a simplified form, which is reasonable for control synthesis. A useful extension would be to incorporate time-aligned bus current, source powers, and motor speed for a few named mission segments so that a data matching study can confirm that the EMS responds correctly to measured demand sequences.

In [37], a complete electric aircraft model is developed that combines the aerodynamic, propulsive, and electrical subsystems into a single simulation environment. The aerodynamic section is constructed using the coordinate axis systems and the standard dynamic equations of motion that describe the aircraft's translational and rotational behaviour under the influence of lift, drag, thrust, and weight. These equations are solved alongside the control loops for altitude, velocity, and flight path angle, each governed by PID controllers. The thrust command is generated by the velocity controller and passed to the propeller model, which determines the propeller torque and thrust using the aerodynamic coefficients of lift and drag. The propeller is linked to the motor model, while the resulting electrical power demand is connected to the energy storage system, allowing the overall energy consumption to be studied for different flight conditions.

The powertrain portion, which includes the propeller, motor, and battery, is modelled using analytical equations rather than full component-level models. The motor behaviour is represented by mathematical expressions relating voltage, current, and torque, without incorporating detailed inverter switching or dynamic electromagnetic effects. Similarly, the battery is treated as a simple energy source that outputs a voltage and current based on power demand, without considering internal resistance or temperature effects. The study evaluates several aircraft types, with detailed focus on the Pipistrel Alpha Electro, where the advance ratio is assumed to remain constant at an optimal value of 0.6. This simplification helps maintain computational efficiency but leads to inaccuracies because the advance ratio, and consequently the propeller thrust and torque coefficients, vary continuously with changes in airspeed and rotational speed. Despite these limitations, the structure of the model clearly demonstrates how energy flow can be assessed across flight segments, though greater accuracy would be achieved by allowing the aerodynamic coefficients to vary dynamically with velocity.

The research work reported in [38] presents a comprehensive model of the Pipistrel Velis Electro, extended with a dual-DC-port inverter architecture that allows integration of a fuel-cell stack alongside the existing lithium-ion battery system. The model includes an explicit parameterization of the battery pack, where the open circuit voltage–state of charge curve is fitted from experimental data to represent nonlinear behaviour during charging and discharging. This level of detail gives realistic battery voltage response under varying load and enables consistent coupling between the fuel cell and the motor drive. The dual-port inverter uses space vector modulation to control energy sharing between the fuel cell and the battery while maintaining the required DC-link voltage for the motor inverter. The electrical and control subsystems are represented using dynamic equations that track current, voltage, and torque in real time, and the study reports good correlation between the simulated and measured power flow.

The mechanical side of the model is simplified. The motor drives a propeller load described by algebraic torque and thrust relations without the use of aerodynamic coefficients such as the thrust or torque coefficient, and the propeller dynamics are reduced to a static relationship between torque and speed. The authors note that the original propeller parameters caused excessive transient torque, which they mitigated by reducing the propeller inertia so that the motor speed could settle within 0.1 seconds. While this adjustment improves numerical stability, it limits physical fidelity because the real propeller inertia strongly influences acceleration and torque demand, especially during mission transients. The study does not vary the advance ratio or simulate multiple flight phases, focusing instead on steady-state operation at matched airspeeds. These simplifications make the electrical results easier to interpret but restrict the model's ability to predict torque and power behaviour under changing aerodynamic conditions. Incorporating experimentally derived propeller coefficients and running the model under realistic flight profiles would yield a more accurate reflection of the Velis Electro's integrated performance.

Reference [39] builds a trajectory energy management environment that couples a six degree of freedom flight dynamics model with a simplified powertrain model and a set of pilot facing displays. Battery behavior is captured with a Thevenin equivalent that uses an open circuit voltage curve fitted to state of charge, and a solver computes the current needed to satisfy the power requested by the flight dynamics code. Motor and inverter behavior for the Velis Electro are represented through an efficiency map of the propulsion unit as a function of torque and speed, while temperatures for battery, motor, and inverter follow first order thermal models driven by I^2R losses. The trajectory module searches feasible routes and trims the vehicle segment by segment, then passes the required power to the powertrain

model and checks limits such as component temperatures, bus power, and state of charge. The authors demonstrate the method on Velis Electro and a lift plus cruise concept, including two Los Angeles routes where the tool reports time histories of temperature, state of charge, and instantaneous endurance, and develop display concepts that range from simple state of charge and power readouts to moving map visualizations with predicted range and guidance.

Several modeling choices keep the system practical but introduce gaps that affect propulsion accuracy for fixed wing electric aircraft. The motor and inverter are not simulated with closed loop current control; thus, transient torque and speed are inferred from maps rather than solved with electrical dynamics, and the propeller load is not computed from aerodynamic coefficients or advance ratio. For Velis Electro, the method trims the aircraft and requests power from maps but does not recalculate propeller thrust and torque as airspeed and rotational speed change, which limits fidelity during climb, descent, and step changes in power. The battery model is appropriate for mission level studies, yet state of energy and state of available power still depend on assumptions about operating limits and estimation accuracy, and the paper itself shows that endurance indications can fluctuate and confuse the pilot unless the averaging window is chosen carefully. The environment validates general behavior against earlier surrogate models and flight test summaries rather than using point by point matching of motor speed, propeller speed, bus current, and power through named mission segments. Replacing map-based propulsion blocks with a propeller coefficient model coupled to a permanent magnet motor with FOC and explicit pulse width modulation, and reporting time aligned traces for speed, torque, current, and state of charge over reference missions, would address these limitations while preserving the trajectory planning features highlighted by the authors.

In [40], the authors focus on trajectory planning for NASA's X-57 Maxwell electric aircraft by linking aerodynamic and electrical models with temperature-dependent constraints on key components. The aircraft motion is represented using two-dimensional equations of flight dynamics, where lift, drag, and thrust forces determine the velocity and altitude evolution. The propulsion system includes simplified analytical models for the battery, inverter, and motor, each described through efficiency-based relations and energy balance equations. The battery is represented by an equivalent circuit that captures open circuit voltage variation with state of charge, and the propeller thrust is obtained from empirical data, allowing the simulation to estimate total power demand along a predefined flight path. The optimization routine adjusts airspeed, power output, and altitude to achieve maximum range or minimum flight time while keeping component temperatures below their operational limits.

The paper shows how thermal constraints influence achievable flight performance, particularly during continuous high-power segments such as climb. However, the model does not account for transient electrical behavior, as current and voltage responses are not dynamically solved. The absence of inverter switching and motor control equations limits the ability to evaluate short-term power fluctuations or torque variations. Additionally, the assumption of steady operating conditions prevents analysis of unsteady power demand during rapid trajectory changes.

Across the reviewed studies, most researchers modeled electric aircraft propulsion by combining aerodynamic, propulsive, and electrical subsystems through analytical equations rather than full dynamic component models. Common limitations include assuming fixed propeller parameters such as constant advance ratio and using simplified expressions for torque and thrust that do not change with airspeed. Several works also represented the motor and inverter using static efficiency relations instead of detailed PMSM FOC structure, preventing accurate analysis of transient current and speed responses. Similarly, the battery models often relied on simplified algebraic equations or ideal voltage sources, overlooking realistic state-of-charge variations during mission transitions.

In the work reported in this thesis, these limitations are addressed by building a complete electric propulsion model that combines the full aircraft equations of motion with a dynamically varying aerodynamic and propeller representation. The advance ratio and aerodynamic coefficients change with flight speed and motor rotational speed, allowing the model to respond realistically to different mission profiles. The powertrain includes a detailed PMSM model with FOC and an inverter modeled with space vector pulse width modulation (SVPWM) in Simulink, ensuring that current and torque responses match actual physical behavior. Simulations are performed across multiple flight missions to study the interactions between propulsion dynamics and overall battery performance, providing a more accurate and integrated understanding of the Pipistrel Velis Electro's operation.

2.2 Background Overview

2.2.1 Aerodynamics Terms

Understanding key aerodynamic terms is essential for analyzing the performance of an electric aircraft and its propeller system. This section outlines the main parameters that describe aerodynamic behavior and are fundamental to quantifying lift, drag, and other forces acting on the aircraft, forming the analytical base for the subsequent evaluation of aerodynamic and propeller performance.

i. Lift (L) and Lift Coefficient (C_L):

Lift is the aerodynamic force generated by an aircraft's wing or aerofoil that acts perpendicular to the oncoming airflow. It is primarily caused by pressure differences between the upper and lower surfaces of the wing, which depend on the aerofoil shape, angle of attack, and airflow velocity. The efficiency of lift generation determines the aircraft's ability to sustain flight. The lift coefficient (C_L) is a dimensionless parameter that relates the lift to the dynamic pressure and the wing area, and it is expressed as

$$C_L = \frac{2L}{\rho V^2 A} \tag{2.1}$$

where L is the lift (N), ρ the air density (kg/m³), V the forward velocity of the aircraft (m/s), and A is the wing area (m²).

ii. Drag (D) and Drag Coefficient (C_D):

Drag is the aerodynamic resistance that acts opposite to the direction of motion of the aircraft through air. It has two major components:

- Parasitic drag, which results from surface friction and increases with the square of velocity.
- Induced drag, which is associated with the generation of lift and is inversely proportional to the square of velocity.

The drag coefficient (C_D) represents the drag normalized by the dynamic pressure and reference area. The zero-lift drag coefficient is given by

$$C_{D0} = \frac{2D}{\rho V^2 A} \tag{2.2}$$

The total drag can also be written as

$$D = \frac{\rho V^2 f}{2} + \frac{2}{V^2 \rho \pi e}\left(\frac{mg}{s}\right)^2 \tag{2.3}$$

where f is the equivalent flat plate area (m²), s the wingspan (m), and e the Oswald's wing efficiency factor.

iii. Oswald's Wing Efficiency Factor (e):

Oswald's efficiency factor is a dimensionless parameter that measures how effectively a wing generates lift relative to the induced drag [41]. It accounts for deviations from the ideal elliptical lift distribution and is calculated using

$$e = 1.78\,(1 - 0.045\,AR^{0.68}) - 0.64 \tag{2.4}$$

where AR is the aspect ratio, defined as the square of the wingspan divided by the wing area.

iv. Advance Ratio (J):

Advance ratio is a key parameter used to describe the relationship between the forward velocity of the aircraft and the rotational speed of the propeller. It is expressed as

$$J = \frac{V}{nd} \tag{2.5}$$

where V is the forward velocity (m/s), n is the propeller's rotational speed (rev/s), and d is the propeller diameter (m). This parameter is widely used in propeller performance analysis, as thrust and efficiency are often expressed as functions of J.

v. Reynolds Number (Re):

Reynolds number is a dimensionless quantity that characterizes the type of flow around an object by comparing inertial and viscous forces. It helps identify whether the flow is laminar, transitional, or turbulent, and is given by

$$Re = \frac{\rho V L_c}{\mu} \tag{2.6}$$

where L_c is the characteristic length (typically the chord length, m) and μ is the dynamic viscosity of the air (Pa·s). In aerodynamic testing, maintaining Reynolds number similarity ensures that model-scale experiments accurately represent full-scale aircraft behavior.

vi. Equivalent Flat Plate Area (f):

Equivalent flat plate area is a simplified representation of an aircraft's drag characteristics. It refers to the area of a hypothetical flat plate that would produce the same amount of drag as the actual aircraft in a given flight condition.

vii. Pitch (p):

The pitch of a propeller refers to the theoretical distance it would move forward in one complete revolution through a solid medium. It can be calculated using

$$p = 2\pi r * \tan(\beta) \tag{2.7}$$

where r is the propeller radius (m) and β is the pitch angle.

viii. Pitch Ratio (B):

Pitch ratio describes the relationship between the propeller's pitch and its diameter. It is given by

$$B = \frac{p}{d} \tag{2.8}$$

where p is the propeller pitch (m) and d is the propeller diameter (m).

ix. Angle of Attack (AoA):

Angle of attack is the angle between the wing's reference line (usually the chord line) and the oncoming airflow. It plays a major role in determining lift. As the angle of attack increases, lift also increases up to a certain limit known as the critical angle. Beyond this point, airflow separation occurs, and the wing stalls.

x. Angle of Sideslip (AoS):

Angle of sideslip is the angle between the aircraft's longitudinal axis and the relative airflow projected onto the horizontal plane. It indicates the sideways motion of the aircraft relative to the wind and influences yaw stability and directional control.

xi. Indicated Airspeed (IAS):

Indicated airspeed is the value shown directly on the aircraft's airspeed indicator. Although indicated airspeed is not corrected for air density variations, it remains directly related to the dynamic pressure acting on the airframe, and therefore provides a practical measure of the aerodynamic forces experienced by the aircraft. Pilots rely on indicated airspeed for controlling the aircraft and for maintaining operation within prescribed performance and structural limits. When IAS is measured in knots (nautical miles per hour), then it is known as knots indicated airspeed (KIAS).

xii. True Airspeed (TAS):

True airspeed represents the actual speed of the aircraft relative to the surrounding air mass. It is derived by correcting the indicated airspeed for variations in air density that arise from changes in altitude and temperature. At higher altitudes, where air density is lower, the same IAS corresponds to a higher TAS. This forms the basis for navigation computations, flight performance evaluations, and aerodynamic analyses, as it reflects the real velocity of the aircraft through the air.

xiii. Ground Speed (GS):

Ground speed is the aircraft's horizontal velocity relative to the Earth's surface. It is obtained by adjusting the true airspeed for the wind component along the flight path: a tailwind increases the ground speed, while a headwind reduces it. Ground speed determines how quickly the aircraft covers distance over the ground and is therefore essential for estimating flight duration, fuel consumption, and navigational accuracy.

xiv. Pressure Altitude:

Pressure altitude is the altitude above the standard reference level where atmospheric pressure equals 1013.25 hPa (29.92 inHg). It is read from the aircraft's altimeter when set to this standard pressure value.

2.2.2 Aircraft Equations of Motion (EOM)

There are two primary frames of reference used to describe the motion of an aircraft: the Earth frame and the body frame [42]. The Earth frame (also called the inertial or ground frame) is fixed in space and is used as the reference for measuring an aircraft's position and overall motion. In this coordinate system, the X_E axis is directed toward the geographic north, the Y_E axis toward the east, and the Z_E axis vertically downward toward the center of the Earth. Because the Earth frame does not move with the aircraft, it is treated as an inertial reference frame for the flight dynamics analysis. The body frame, on the other hand, is a coordinate system rigidly attached to the aircraft. Its origin is located at the aircraft's center of gravity (CG). The x_B axis is oriented along the longitudinal axis of the fuselage and points forward, the y_B axis extends laterally toward the right wing, and the z_B axis points downward and is perpendicular to both x_B and y_B. This moving reference frame is used to express the aerodynamic and propulsive forces, moments, and velocity components that act on the aircraft. The Earth and body frames are shown in Figures 2.1 and 2.2, respectively.

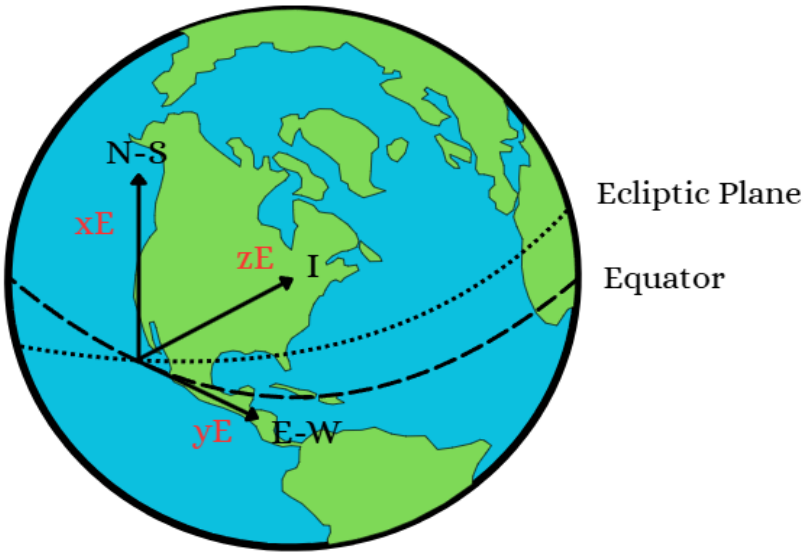


Figure 2.1 Earth frame (stationary).

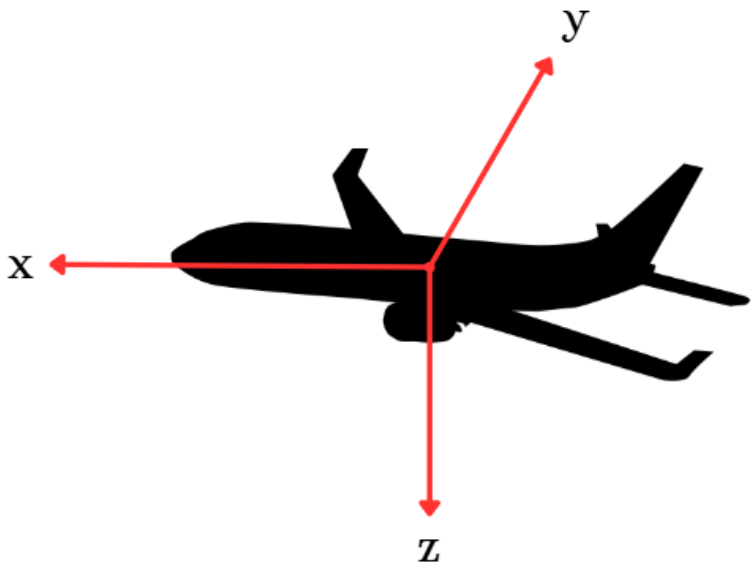


Figure 2.2 Body frame (attached to the aircraft).

The orientation of the aircraft relative to the Earth frame is described using Euler angles. These angles represent a sequence of rotations required to align the Earth frame with the body frame. There are three Euler angles: yaw (ψ), pitch (θ), and roll (φ) [43].

i. Yaw (Heading) Angle Rotation:

Yaw describes the rotation of the aircraft around its vertical axis (z-axis), which runs up and down through the aircraft. This motion affects the aircraft's heading or the direction it is pointing horizontally. When the aircraft yaws, its nose moves left or right. Figure 2.3 and Equations (2.9)-(2.11) describe yaw angle.

$$x_1 = x_E \cos\Psi + y_E \sin\Psi \quad (2.9)$$

$$y_1 = -x_E \sin\Psi + y_E \cos\Psi \quad (2.10)$$

$$z_1 = z_E \quad (2.11)$$

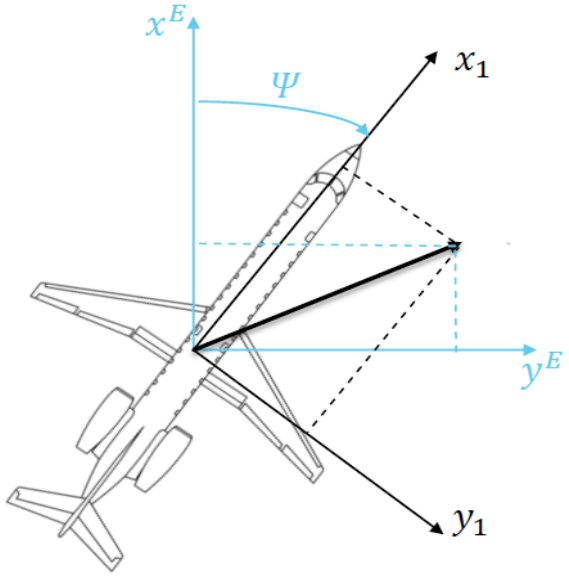


Figure 2.3 Yaw angle.

ii. Pitch Angle Rotation:

Pitch describes the rotation of the aircraft around its lateral axis (y-axis), which runs from wingtip to wingtip. This motion determines whether the aircraft's nose is tilted up or down. Changing pitch affects the altitude of the aircraft. Figure 2.4 and Equations (2.12)-(2.14) describe pitch angle.

$$x_2 = x_1\cos\theta - z_1\sin\theta \quad (2.12)$$

$$y_2 = y_1 \quad (2.13)$$

$$z_2 = x_1\sin\theta + z_1\cos\theta \quad (2.14)$$

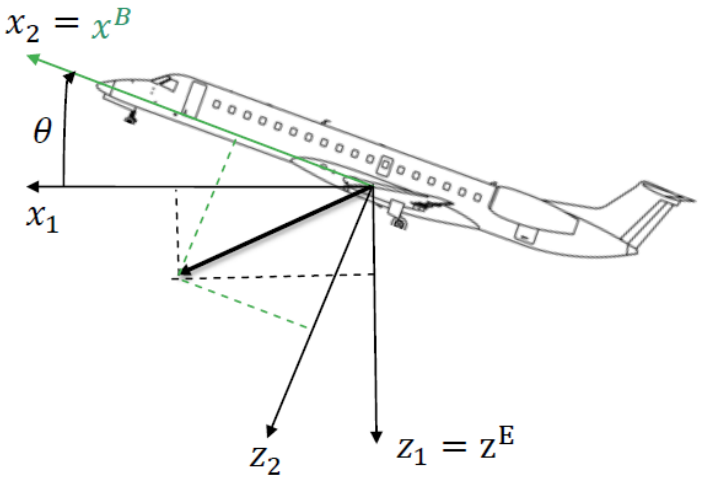


Figure 2.4 Pitch angle.

iii. Roll (Bank) Angle Rotation:

Roll describes the rotation of the aircraft around its longitudinal axis (x-axis), which runs from the nose to the tail. When the aircraft rolls, one wing moves up while the other moves down, and it tilts the aircraft sideways. Roll is important for banking turns; when an aircraft rolls, it changes the direction it turns by tilting toward the direction of the turn. Figure 2.5 and Equations (2.15)-(2.17) describe roll angle.

$$x_B = x_2 \tag{2.15}$$

$$y_B = y_2 \cos\phi + z_2 \sin\phi \tag{2.16}$$

$$z_B = -y_2 \sin\phi + z_2 \cos\phi \tag{2.17}$$

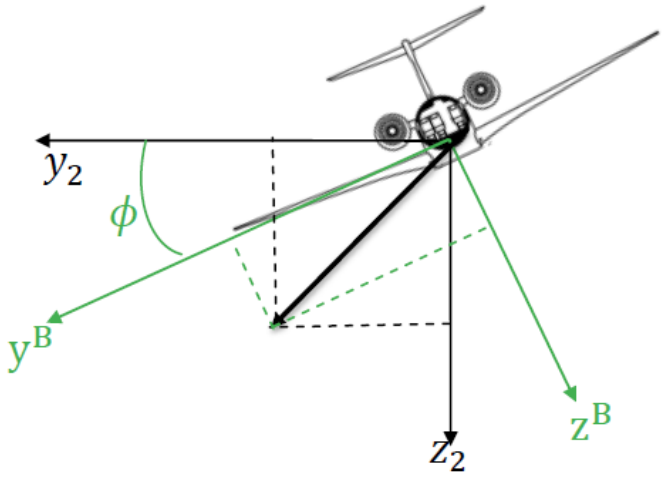


Figure 2.5 Roll angle.

These three angles together describe the complete orientation of the aircraft in the three-dimensional space and form the basis for transforming quantities between the Earth and body coordinate systems.

To relate quantities expressed in different reference frames, it is necessary to define rotation transformations. These transformations describe how a vector or force component changes when viewed from the Earth frame, body frame, or stability frame [44]. The rotations are typically represented using direction cosine matrices derived from the Euler angles.

$$\text{Roll: } R1(\phi) = \begin{bmatrix} 1 & 0 & 0 \\ 0 & \cos\phi & \sin\phi \\ 0 & -\sin\phi & \cos\phi \end{bmatrix} \tag{2.18}$$

$$\text{Pitch: } R2(\theta) = \begin{bmatrix} \cos\theta & 0 & -\sin\theta \\ 0 & 1 & 0 \\ \sin\theta & 0 & \cos\theta \end{bmatrix} \tag{2.19}$$

$$\text{Yaw: } R3(\psi) = \begin{bmatrix} \cos\psi & \sin\psi & 0 \\ -\sin\psi & \cos\psi & 0 \\ 0 & 0 & 1 \end{bmatrix} \tag{2.20}$$

The complete rotation from the Earth frame to the body frame involves three successive rotations. The inverse transformation converts body-axis quantities back to the Earth frame.

a. Earth to Body Transformation:

$$\overrightarrow{F_{Body}} = R1(\phi)R2(\theta)R3(\psi)\,\overrightarrow{F_{Earth}} \tag{2.21}$$

$$\overrightarrow{F_{Body}} = \begin{bmatrix} \cos\theta\cos\varphi & \cos\theta\sin\varphi & -\sin\theta \\ \sin\emptyset\sin\theta\cos\varphi - \cos\emptyset\sin\varphi & \cos\emptyset\cos\varphi + \sin\emptyset\sin\theta\sin\varphi & \sin\emptyset\cos\theta \\ \cos\emptyset\sin\theta\cos\varphi + \sin\emptyset\sin\varphi & -\sin\emptyset\cos\varphi + \cos\emptyset\sin\theta\sin\varphi & \cos\emptyset\cos\theta \end{bmatrix} \overrightarrow{F_{Earth}} \tag{2.22}$$

b. Body to Earth Transformation:

$$\overrightarrow{F_{Earth}} = R3^{-1}(\psi)R2^{-1}(\theta)R1^{-1}(\phi)\overrightarrow{F_{Body}} \tag{2.23}$$

The stability axis, also known as the stability frame, is another coordinate system aligned with the aircraft's relative airflow. Its x-axis points along the direction of the free-stream velocity, while its z-axis lies in the plane of symmetry, pointing downward. This frame is particularly useful in aerodynamic analysis because the major aerodynamic forces, which are lift and drag, act primarily along stability frame's principal axes.

The relationship between the stability axis and the body axis can be represented by a single rotation about the lateral (y)-axis through the angle of attack (α).

$$\overrightarrow{F_{Body}} = R2(\alpha)\ \overrightarrow{F_{Stabılıty}} \tag{2.24}$$

$$R2(\alpha) = \begin{bmatrix} \cos\alpha & 0 & -\sin\alpha \\ 0 & 1 & 0 \\ \sin\alpha & 0 & \cos\alpha \end{bmatrix} \tag{2.25}$$

2.2.3 Translational Motion

Translational motion refers to the movement of the aircraft's center of mass along the three principal axes, which are the longitudinal, lateral, and vertical axes [45]. These axes define the body reference frame and are associated with the aircraft's linear velocity components. The longitudinal axis corresponds to forward motion; the lateral axis corresponds to sideways motion; and the vertical axis corresponds to motion in the upward or downward direction. The position of the aircraft changes continuously due to the combined influence of aerodynamic, propulsive, and gravitational forces.

The general form of Newton's second law governing translational motion is given as

$$\sum \vec{F} = m\frac{d\vec{V}}{dt} \tag{2.26}$$

where

$\vec{F}$ is the total force acting on the aircraft (N),

M is the mass of the aircraft (kg), and

$\frac{d\vec{V}}{dt}$ is the rate of change of velocity (acceleration).

To describe translational motion in the body reference frame, the external forces acting on the aircraft are resolved along the body axes. This formulation accounts for both linear and rotational effects since the aircraft experiences rotation about its center of gravity in addition to translation. The expression for translational motion in the body frame is derived as follows

$$\frac{d\vec{V}}{dt} = \vec{V}_{Body} + \vec{\omega}_{Body} \times \vec{V}_{Body} \tag{2.27}$$

where, $\vec{V}_{Body} = \boldsymbol{U}\hat{\imath} + \boldsymbol{V}\hat{\jmath} + \boldsymbol{W}\hat{k}$ and $\vec{\omega}_{Body} = \boldsymbol{P}\hat{\imath} + \boldsymbol{Q}\hat{\jmath} + \boldsymbol{R}\hat{k}$.

Multiplying the acceleration with mass of the aircraft gives the translational equations of motion (EOM) in component form:

$$m\begin{bmatrix} \dot{\boldsymbol{U}} + \boldsymbol{QW} - \boldsymbol{RV} \\ \dot{\boldsymbol{V}} + \boldsymbol{RU} - \boldsymbol{PW} \\ \dot{\boldsymbol{W}} + \boldsymbol{PV} - \boldsymbol{QU} \end{bmatrix} = \begin{bmatrix} Fx \\ Fy \\ Fz \end{bmatrix} \tag{2.28}$$

where

$\boldsymbol{U}$, $\boldsymbol{V}$, and $\boldsymbol{W}$ are velocity components in the X, Y, Z directions (m/s).

$\boldsymbol{P}$, $\boldsymbol{Q}$, and $\boldsymbol{R}$ are angular velocity components in roll, pitch, and yaw (rad/s).

Fx, Fy, Fz are Forces in the X, Y, Z directions (N).

The equations can be separated into two categories for analytical purposes: longitudinal motion and lateral directional motion.

Longitudinal Motion (XZ Plane):

Longitudinal motion occurs in the XZ plane and involves movement along the forward and vertical directions. It is primarily influenced by thrust, drag, lift, and the weight of the aircraft. Longitudinal motion determines the variation of velocity, pitch, and altitude during flight.

a) X-axis Force: $m(\dot{\boldsymbol{U}} + \boldsymbol{QW} - \boldsymbol{RV}) = -mg\sin\theta + (-D\cos\alpha + L\sin\alpha) + T\cos\phi_T$ (2.29)

b) Z-axis Force: $m(\dot{\boldsymbol{W}} + \boldsymbol{PV} - \boldsymbol{QU}) = mg\cos\phi\cos\theta + (-D\sin\alpha - L\cos\alpha) - T\sin\phi_T$ (2.30)

Lateral Directional Motion (Y-Axis):

Lateral directional motion occurs in the YZ plane and describes the sideward and yawing behavior of the aircraft. It is governed by side forces and the aerodynamic moments that act about the roll and yaw axes. Lateral directional motion affects the aircraft's stability and control during maneuvers such as turns or when operating in crosswind conditions.

a) Y-axis Force: $m(\dot{\boldsymbol{V}} + \boldsymbol{RU} - \boldsymbol{PW}) = mg\sin\phi\cos\theta + Fy$ (2.31)

Here, θ is the pitch angle, α the angle of attack, ϕ the roll/bank angle and ϕ_T the thrust component angle.

The kinematic equations shown below are used to relate the aircraft's angular velocity components in the body frame to the Euler angles and their respective time derivatives, known as Euler rates. These equations provide the transformation between the rotational motion expressed in the body axes and the rate of change of the aircraft's orientation in space.

$$\begin{bmatrix} \boldsymbol{P} \\ \boldsymbol{Q} \\ \boldsymbol{R} \end{bmatrix} = \begin{bmatrix} 1 & 0 & -\sin\theta \\ 0 & \cos\emptyset & \cos\theta\sin\emptyset \\ 0 & -\sin\emptyset & \cos\theta\cos\emptyset \end{bmatrix} \begin{bmatrix} \dot{\emptyset} \\ \dot{\theta} \\ \dot{\varphi} \end{bmatrix} \quad (2.32)$$

2.2.4 Rotational Motion

Rotational motion refers to the movement of the aircraft about its center of mass around the three principal axes that define its orientation in space, i.e., roll, pitch, and yaw [46]. These rotations describe how the aircraft's orientation changes with time as it maneuvers or responds to aerodynamic moments. Each rotational motion is associated with an angular velocity component and a corresponding rotational acceleration governed by the moments of inertia and the external moments acting on the aircraft.

The general form of the rotational equation of motion is given by

$$\sum \vec{M} = \frac{d\vec{H}}{dt} \quad (2.33)$$

where

$\vec{M}$ is the total moment acting on the aircraft (Nm).

$\vec{H}$ is the angular momentum ($I\vec{\omega}$, where I is the moment of inertia tensor, and $\vec{\omega}$ is angular velocity).

In the body reference frame, the total external moment equals the sum of the moment required to produce angular acceleration and the additional coupling moment that arises due to the interaction between angular velocity components.

$$\sum \overrightarrow{\mathrm{M_{ext}}}^{\mathrm{B}} = \begin{bmatrix} I_{xx} & 0 & -I_{xz} \\ 0 & I_{yy} & 0 \\ -I_{zx} & 0 & I_{ZZ} \end{bmatrix} \begin{bmatrix} \dot{\boldsymbol{P}} \\ \dot{\boldsymbol{Q}} \\ \dot{\boldsymbol{R}} \end{bmatrix} + \begin{bmatrix} \boldsymbol{Q}(\boldsymbol{R}I_{ZZ} - \boldsymbol{P}I_{xz}) - \boldsymbol{R}\boldsymbol{Q}I_{yy} \\ \boldsymbol{R}(\boldsymbol{P}I_{xx} - \boldsymbol{R}I_{xz}) - \boldsymbol{P}(\boldsymbol{R}I_{ZZ} - \boldsymbol{P}I_{xz}) \\ \boldsymbol{P}\boldsymbol{Q}I_{yy} - \boldsymbol{Q}(\boldsymbol{P}I_{xx} - \boldsymbol{R}I_{xz}) \end{bmatrix} \quad (2.34)$$

Expanding the above matrix equation yields the rotational equations of motion in the body-axis system:

$$\dot{\boldsymbol{P}}\mathrm{Ixx} + \boldsymbol{QR}(\mathrm{Izz} - \mathrm{Iyy}) - (\dot{\boldsymbol{R}} + \boldsymbol{PQ})\mathrm{Ixz} = \boldsymbol{L} \quad (2.35)$$

$$\dot{\boldsymbol{Q}}\mathrm{Iyy} - \boldsymbol{PR}(\mathrm{Izz} - \mathrm{Ixx}) + (\boldsymbol{P^2} - \boldsymbol{R^2})\mathrm{Ixz} = \boldsymbol{M} \quad (2.36)$$

$$\dot{\boldsymbol{R}}\mathrm{Izz} + \boldsymbol{PQ}(\mathrm{Iyy} - \mathrm{Ixx}) + (\boldsymbol{QR} - \dot{\boldsymbol{P}})\mathrm{Ixz} = \boldsymbol{N} \quad (2.37)$$

where

P, ***Q***, and ***R*** are roll, pitch, and yaw rates,

L, ***M***, and ***N*** are rolling, pitching, and yawing moments,

Ixx, Iyy, and Izz are principal moments of inertia, and

Ixz is product of inertia.

These equations describe how the angular accelerations ($\dot{\boldsymbol{P}}, \dot{\boldsymbol{Q}}, \dot{\boldsymbol{R}}$) are influenced by the external moments, the aircraft's mass distribution, and the coupling between the rotations about different axes. The terms involving I_{xz} represent the coupling effects that occur in asymmetric aircraft, where the principal axes of inertia do not coincide exactly with the body axes. For most small, symmetric aircraft, I_{xz} is often negligible, which simplifies the equations.

In the context of this study, the rotational equations of motion are presented for completeness but are not further analysed due to the unavailability of detailed information on the aircraft's inertia properties and aerodynamic moment coefficients. The orientation of the aircraft is instead derived from measured flight data and considered as an input to the simulation models.

The background overview established the theoretical foundation necessary to analyze the aerodynamic and propulsive behavior of the electric aircraft. It began by defining the fundamental aerodynamic quantities and non-dimensional coefficients that govern lift, drag, and related forces acting on the

aircraft. These parameters describe the interaction between airflow and aerodynamic surfaces and are essential for assessing propeller performance and flight efficiency. The discussion then introduced the coordinate reference frames and the Euler angles that define aircraft orientation in three-dimensional space. Using these definitions, the translational and rotational equations of motion were presented to describe how forces and moments act on the aircraft and how its velocity and orientation evolve with time. Together, these formulations provide the mathematical framework for modeling aerodynamic forces, resolving them along appropriate axes, and linking measured flight quantities with theoretical performance predictions. The concepts introduced in this section serve as the basis for the methodology that follows, where they are applied to estimate propeller thrust and evaluate the aerodynamic performance of the electric aircraft across different flight phases.

Chapter 3
Aircraft Aerodynamic Analysis

In this chapter, the modeling and analysis of the propeller for the Pipistrel Velis Electro are presented. Two different approaches are taken to estimate the motor rotational speed and torque, and propeller thrust. The first approach derives thrust from the aircraft equations of motion (EOM) using velocity, altitude, and orientation angles as inputs, after which the propeller equations are applied to compute the corresponding rotational speed and torque. The second approach employs the motor power command (MPC) as the primary input, together with the aircraft velocity and altitude, to directly estimate the propeller thrust, as well as motor rotational speed and torque. The algorithms implemented for both methods are detailed, followed by simulations performed for normal and touch-and-go flight missions. Finally, the outcomes of both methods are evaluated to determine their agreement with experimental flight measurements and their suitability for subsequent integration with the electric powertrain model.

3.1 EOM-Based Approach

This section applies the equations of motion to determine the aerodynamic and propulsive forces acting on the aircraft during a complete flight mission. The analysis derives the required thrust and lift for each operating condition using formulations derived from the governing equations of motion. By evaluating these conditions separately, the variation in aerodynamic loading and power demand across the flight profile can be clearly represented.

3.1.1 Methodology

The flight mission is divided into four distinct phases: ground roll (taxiing) before takeoff and after landing, climb, cruise, and descent, as shown in Figure 3.1. The approach taken to identify different flight phases is presented in Figure 3.2. Each phase exhibits specific values of acceleration, orientation, and aerodynamic forces, and the balance among these quantities determines the motion and performance of the aircraft.

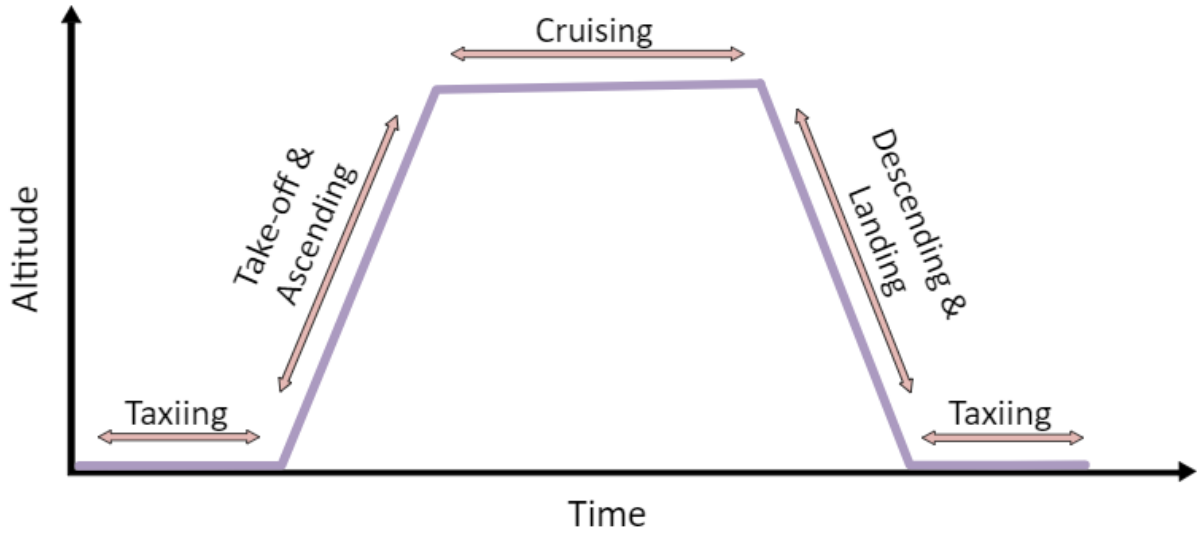


Figure 3.1 Flight stages.

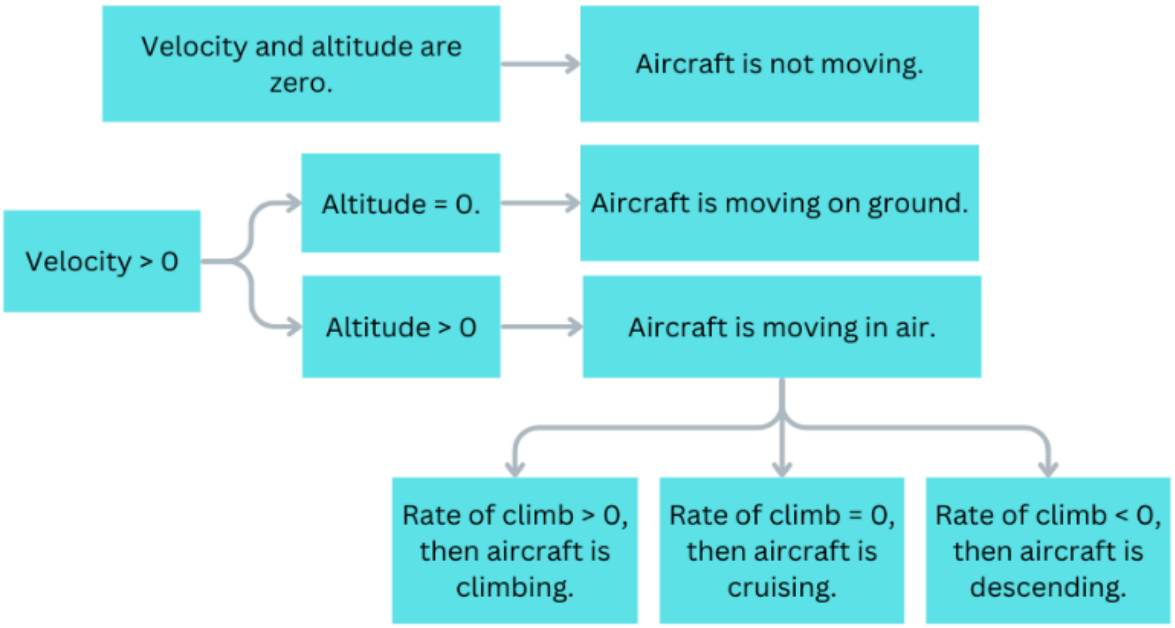


Figure 3.2 Flight phase identification.

A case-based formulation is used to determine thrust in each phase:

1. Ground Roll – Before Take-off:

$$T = D + \mu(W - L) + ma;\ a > 0 \tag{3.1}$$

where T is the thrust, D the drag, μ the rolling resistance coefficient, W the weight., L the lift, m the mass, and the longitudinal acceleration in m/s^2.

2. Steady Climb or Descent:

   When the velocity remains constant, the acceleration is zero ($\dot{\boldsymbol{U}}$ =$\dot{\boldsymbol{V}}$=$\dot{\boldsymbol{W}}$= 0), leading to the following relations:

$$T\cos\emptyset_T = D + mg\sin\theta \tag{3.2}$$

$$L = mg\cos\theta \tag{3.3}$$

In (3.2) and (3.3), T is thrust, $\emptyset_T$ thrust angle, D the drag, m the mass, g the gravitational acceleration, L the lift, and θ the pitch angle.

3. Steady Level Flight ($\dot{\boldsymbol{U}}$ =$\dot{\boldsymbol{V}}$=$\dot{\boldsymbol{W}}$= 0):

   For level motion without banking ($\boldsymbol{W}$ = 0, ϕ = 0)

$$T = D \tag{3.4}$$

$$L = mg \tag{3.5}$$

where T is the thrust, D the drag, L the lift, m the mass, and g the gravitational acceleration.

4. Coordinated Turn (Steady Bank):

   During a constant radius turn with a steady bank angle ϕ, the horizontal component of lift provides the required centripetal force

$$T\cos\emptyset_T = D \tag{3.6}$$

$$L\sin\emptyset = \frac{mV^2}{R_{turn}} \tag{3.7}$$

$$L\cos\emptyset = mg \tag{3.8}$$

where T is the thrust, $\emptyset_T$ the thrust angle, D the drag, L the lift, ∅ the roll angle, m the mass, V the aircraft velocity, R_{turn} the turn radius and g the gravitational acceleration.

The total lift is obtained from the square root of the sum of the squares of these components.

5. Non-Steady Flight:

   Where accelerations exist ($\dot{\boldsymbol{U}}, \dot{\boldsymbol{V}}, \dot{\boldsymbol{W}} \neq 0$), equations (3.29) and (3.30) are rearranged to compute thrust directly and lift is calculated as in case 4.

6. Ground Roll – After Landing:

$$T = D + \mu W + ma;\ a < 0 \tag{3.9}$$

where T is the thrust, D the drag, μ the rolling resistance coefficient, W the weight, m the mass, and a the longitudinal acceleration.

The velocity and calculated thrust are then used to find the best pair of advance ratio and thrust coefficient for efficient propeller operation. The propeller analysis is explained in the next section.

Certain quantities required for this analysis, including the yaw or heading rate ($\dot{\varphi}$), angle of attack (α), and turn radius (R_{turn}), are not available in the dataset and are therefore computed analytically. Before introducing these expressions, the load factor (n_{lf}), which represents the ratio of lift to aircraft weight, is given as

$$n_{lf} = \frac{L}{W} = \frac{1}{\cos\emptyset} \tag{3.10}$$

where n_{lf} is the load factor, L, the lift, W the weight, and ∅ the roll angle.

From (3.10), the yaw rate and turn radius are determined as

$$\dot{\varphi} = \frac{g\sqrt{n_{lf}^2 - 1}}{V} \tag{3.11}$$

$$R_{turn} = \frac{V^2}{g\sqrt{n_{lf}^2 - 1}} \tag{3.12}$$

where $\dot{\varphi}$ is the yaw rate, R_{turn} the turn radius, n_{lf} the load factor, V the aircraft velocity, and g the gravitational acceleration. Note that the angle of attack is taken to be equal to the pitch angle, consistent with the limitations of the available flight data.

3.1.2 Propeller Study

Several approaches have been developed to predict propeller performance based on aerodynamic theory. Among them are the blade element theory (BET), the blade element momentum theory (BEMT), and the vortex theory [47]. The BET divides the propeller blade into small radial elements and determines the aerodynamic forces acting on each section, which are then integrated to estimate the total thrust and torque. The BEMT refines this by combining the sectional analysis with momentum conservation across the propeller disk, improving predictions of induced flow and propeller efficiency. In the vortex theory, the airflow downstream of the propeller is modeled as a network of trailing vortices, allowing accurate capture of complex three-dimensional flow effects. For an existing aircraft such as the Pipistrel Velis Electro, these analytical methods are not required since the propeller geometry and performance have already been characterized through controlled experiments. The performance coefficients are usually determined from wind-tunnel testing or propeller stand measurements, where thrust, torque, and speed are recorded under known flow conditions. In [48], the author presented the experimentally derived plots of power coefficient (C_p) versus advance ratio (J) and propeller efficiency (η) versus aircraft speed for the Velis Electro. These datasets were extracted and used to construct the thrust and torque coefficient curves used in this study, as shown in Figure 3.3. In this figure, C_p is the power coefficient, C_t the thrust coefficient and C_q the torque coefficient.

Since no experimental points were available for lower advance ratios ($0 \leq J \leq 0.43$), the power coefficient curve was extended using curve fitting to cover that range smoothly. The efficiency curve was also extrapolated so that it passes through the origin, ensuring that efficiency approaches zero when the propeller is stationary. The resulting efficiency vs the knots indicated airspeed (KIAS) relationship is presented in Figure 3.4.

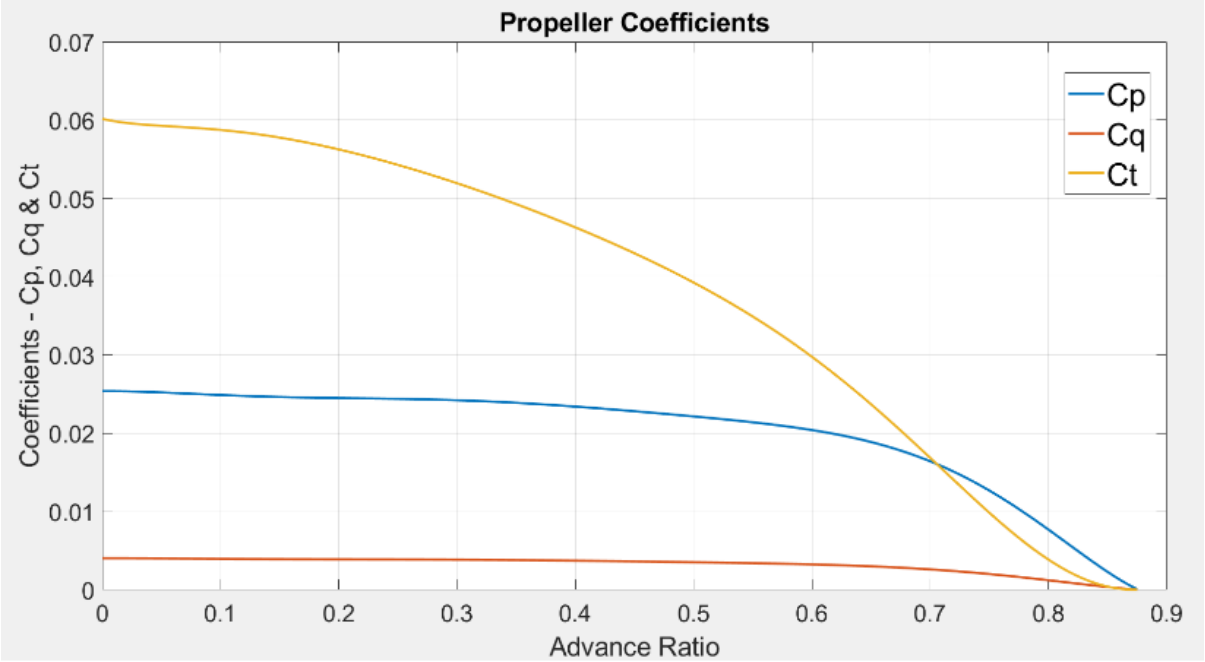


Figure 3.3 Propeller coefficients versus advance ratio.

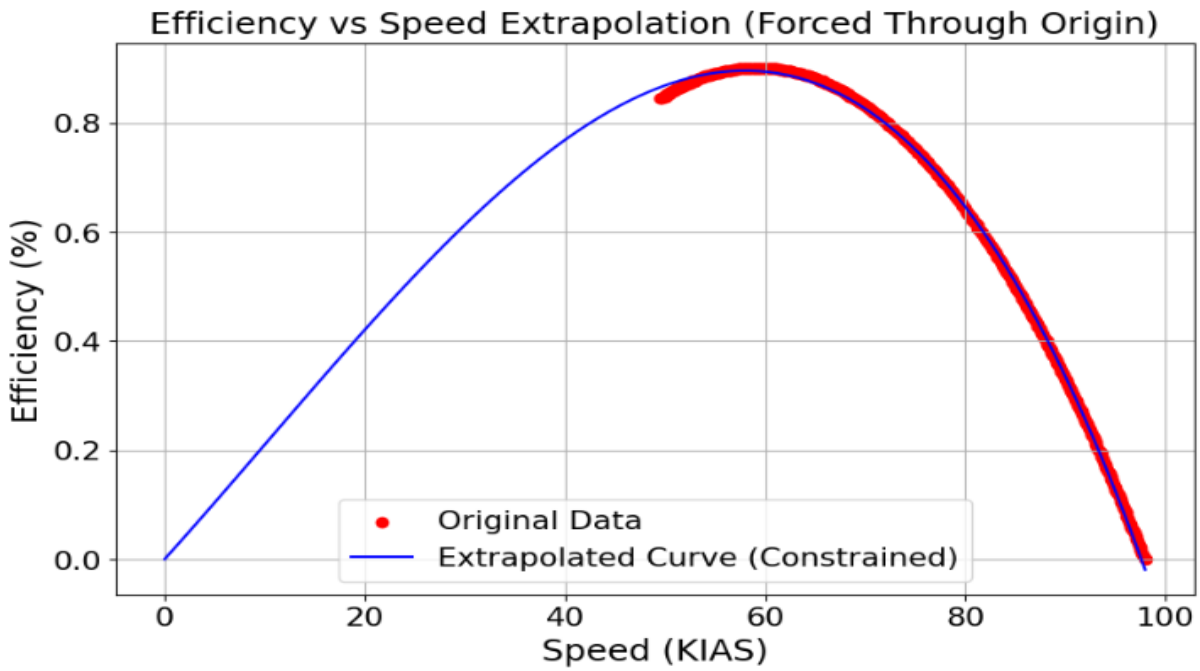


Figure 3.4 Propeller efficiency versus aircraft speed in knots.

The relationships among propeller performance coefficients are summarized below. These equations allow the calculation of thrust, torque, and power once any two parameters are known.

Propeller Efficiency:

$$\eta = \frac{C_t J}{C_p} \tag{3.13}$$

where η is the propeller efficiency, C_t the thrust coefficient, C_p the power coefficient and J the advance ratio.

Thrust Coefficient:

$$C_t = \frac{T}{\rho n^2 d^4} \tag{3.14}$$

where T is the thrust, C_t the thrust coefficient, ρ the air density, n the propeller rotational speed, and d the propeller diameter.

Power Coefficient:

$$C_p = \frac{P}{\rho n^3 d^5} \tag{3.15}$$

where P is the power, C_p the power coefficient, ρ the air density, n the propeller rotational speed, and d the propeller diameter.

Torque Coefficient:

$$C_q = \frac{C_p}{2\pi} = \frac{Q}{\rho n^2 d^5} \tag{3.16}$$

where Q is the torque, C_q the torque coefficient, ρ the air density, n the propeller rotational speed, and d the propeller diameter.

These coefficient plots are essential for determining the operating range and performance of the propeller. In this thesis, they are used to find the motor rotational speed and shaft torque. Due to the absence of a gearbox in the powertrain of Velis Electro aircraft, the motor output power is assumed to be fully converted to the propeller thrust. Other losses are considered negligible as well. The block diagram in Figure 3.5 shows how the rotational speed and torque are computed for each instant of the flight profile.

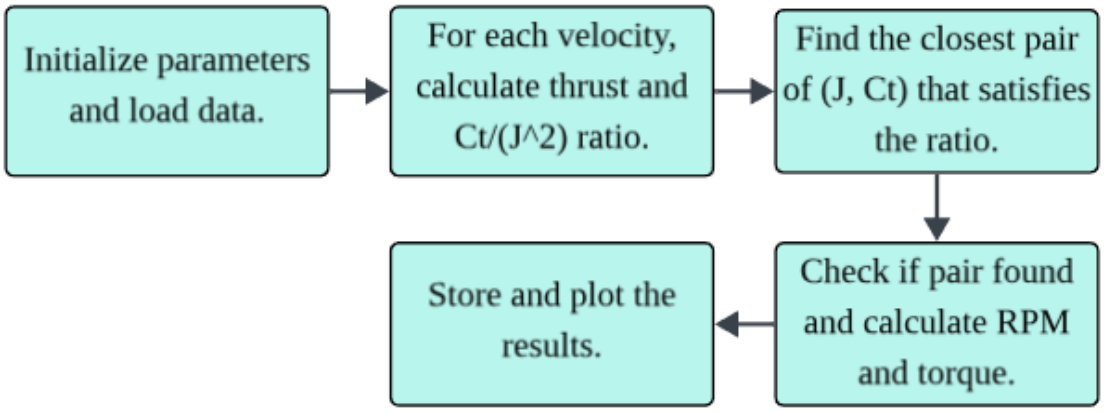


Figure 3.5 Rotational speed and torque estimation methodology.

After the thrust is computed for each velocity, the next step is to determine the operating condition of the propeller. This is done by combining the advance ratio and thrust coefficient relationships from equations (2.5) and (3.14).

Substituting (2.5) into (3.14) gives

$$C_t = \frac{TJ^2}{\rho V^2 d^2} \tag{3.17}$$

which can be rearranged as

$$\frac{C_t}{J^2} = \frac{T}{\rho V^2 d^2} \tag{3.18}$$

This ratio links the non-dimensional thrust characteristics of the propeller with the actual thrust and flight conditions. It is independent of rotational speed, making it an effective parameter for matching the estimated thrust with the propeller curves.

The value of the ratio obtained from the previous thrust computation is compared with the thrust coefficient plot in Figure 8. The point on the curve where the two values coincide defines the valid pair of J and C_t for that operating condition. Once this pair is identified, the same advance ratio is used on the torque coefficient plot to obtain C_q. With the known value of C_q, the load torque is evaluated from (3.16) and the rotational speed is determined using (2.5). Repeating this procedure for each velocity in the flight dataset produces a time series of rotational speed and torque for the complete mission profile.

3.1.3 Dataset Description

Real flight data of the Pipistrel Velis Electro were obtained from flight missions conducted in the Region of Waterloo, Ontario, Canada, through a research collaboration between the Waterloo Wellington Flight Centre (WWFC) and the University of Waterloo. The recorded dataset contains numerous variables; however, for the purposes of this study, only the following parameters were extracted and used as inputs to the mathematical model:

- Indicated Airspeed (IAS) and Ground Speed (GS), both originally measured in knots and converted to metres per second (m/s) during preprocessing as shown below.

$$V_{m/s} = V_{knots} \times 0.514444 \tag{3.19}$$

- Pressure Altitude (m), converted to true altitude relative to ground level as given below.

$$h = \max\left[(PA_m \times 3.28084 - 1050), 0\right] \times 0.3048, \tag{3.20}$$

  where h is the true altitude in meters, and PA_m the pressure altitude in meters.

- Time derivatives of altitude and IAS.

- Pitch, roll, and heading (yaw) angles (radians), along with the time derivatives of pitch and roll angles (radians per second).

- Velocity and acceleration components along the *x*, *y*, and *z* axes, where *x* denotes the longitudinal direction, *y* the lateral direction, and *z* the vertical (normal) direction, all defined with respect to the aircraft's body axis.

The recorded motor speed data are subsequently used to validate the rotational speed computed using the proposed methodology.

3.1.4 Simulation Results:

The simple flight mission profile represented by Figures (3.6) – (3.15) is used for testing the proposed model. The aircraft is stationary for most of in the first 11 minutes. The spike in velocity at around t = 8 mins could be attributed to moving to reach the runway. Take-off happens at around t = 12 mins following which the altitude starts increasing. The cruise period is from 15 to around 27 mins, with a slow decrease in altitude. The aircraft starts its descent at t = 27 mins and finally lands at t = 32 mins.

The ground roll after landing happens during the 32-35 mins period. The overall length of the flight is around 35 minutes.

The following flight profile is given to the developed model to estimate the thrust, rotational speed and torque of the propeller. From the torque and rotational speed, estimated power is computed, which is then compared with the actual power.

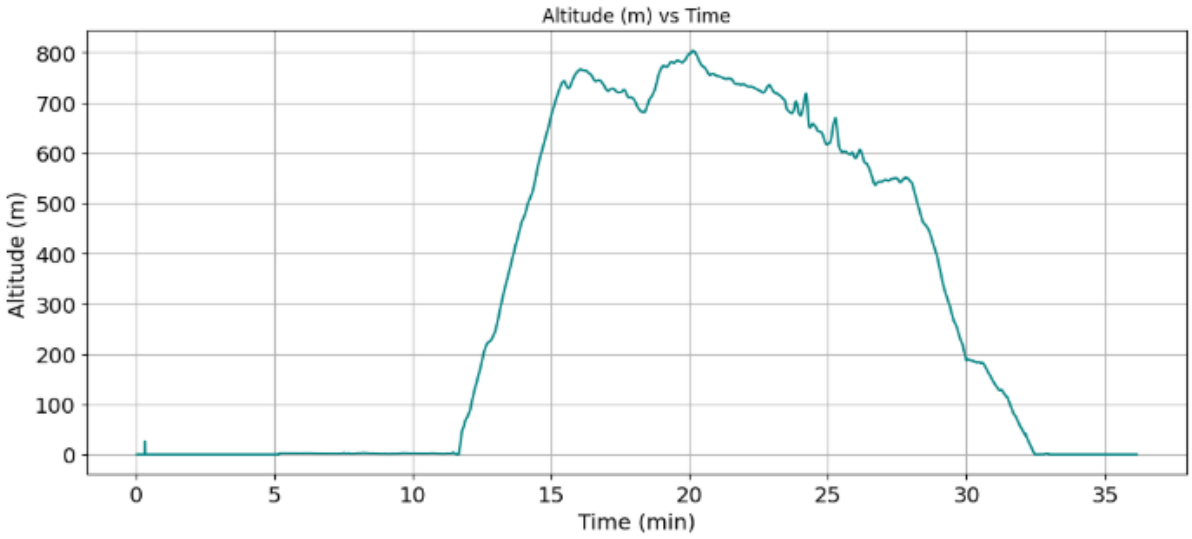


Figure 3.6 Aircraft flying altitude with respect to the airport ground.

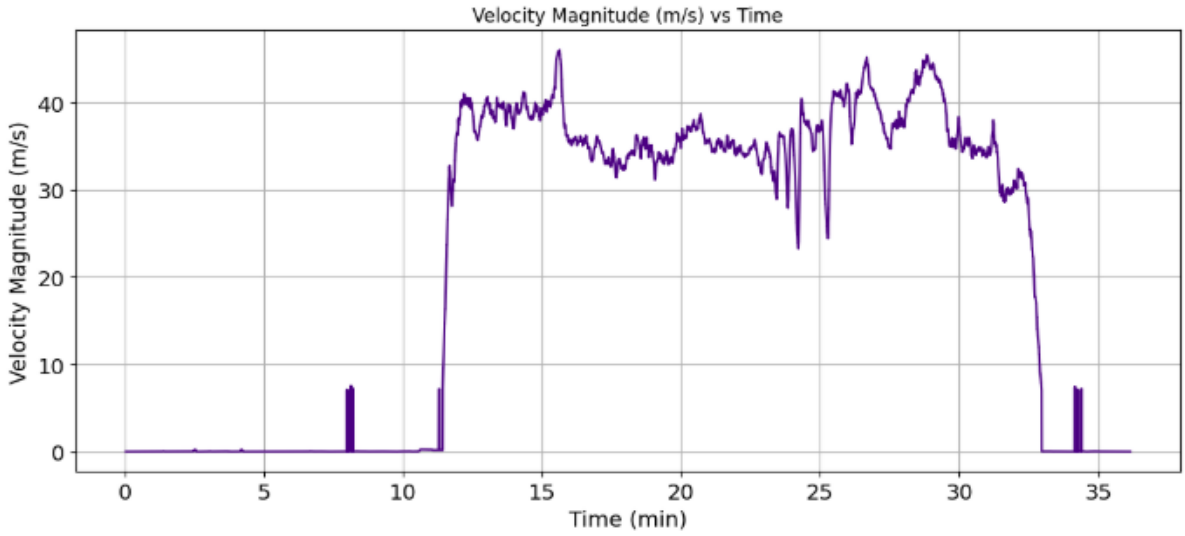


Figure 3.7 Magnitude of aircraft forward velocity (Indicated Air Speed, IAS).

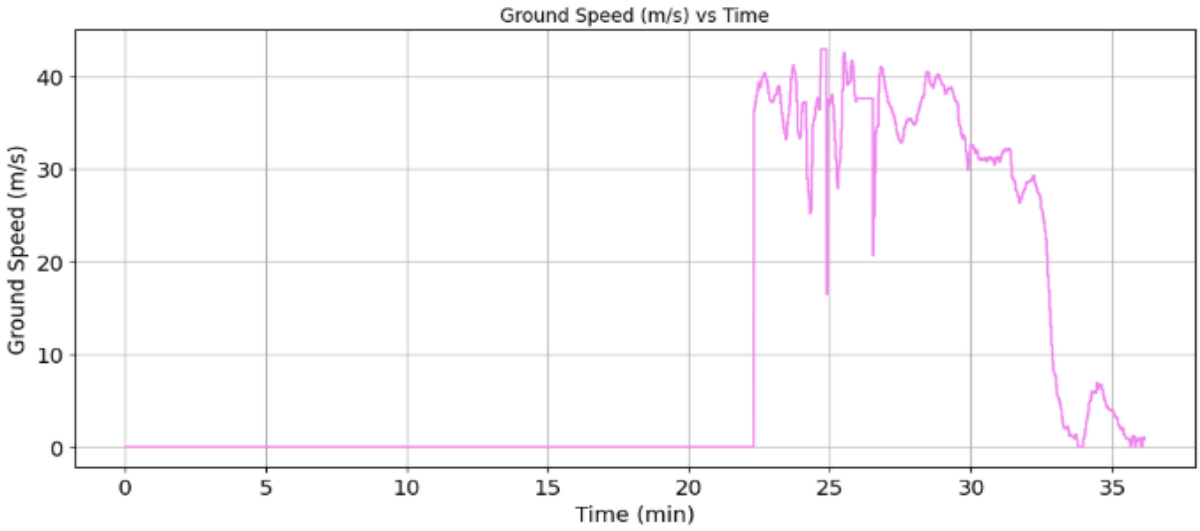


Figure 3.8 Ground Speed.

Note: The ground speed (GS) data remain zero during the initial period of the flight timeline because the recording was not started at that time. The absence of data in this segment is therefore due to the delayed initiation of logging rather than the aircraft being stationary.

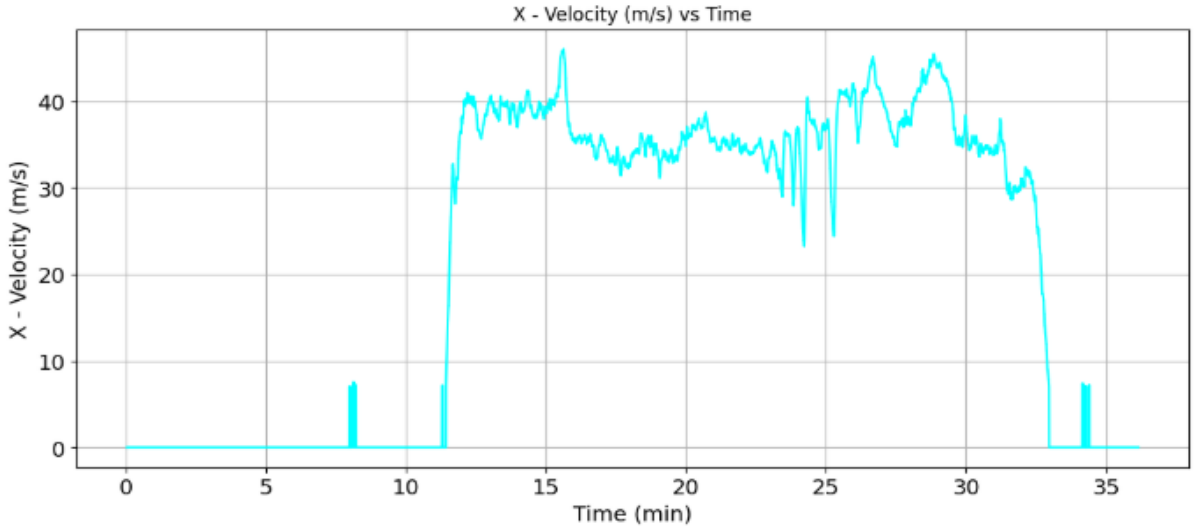


Figure 3.9 Aircraft velocity along the x-axis (longitude).

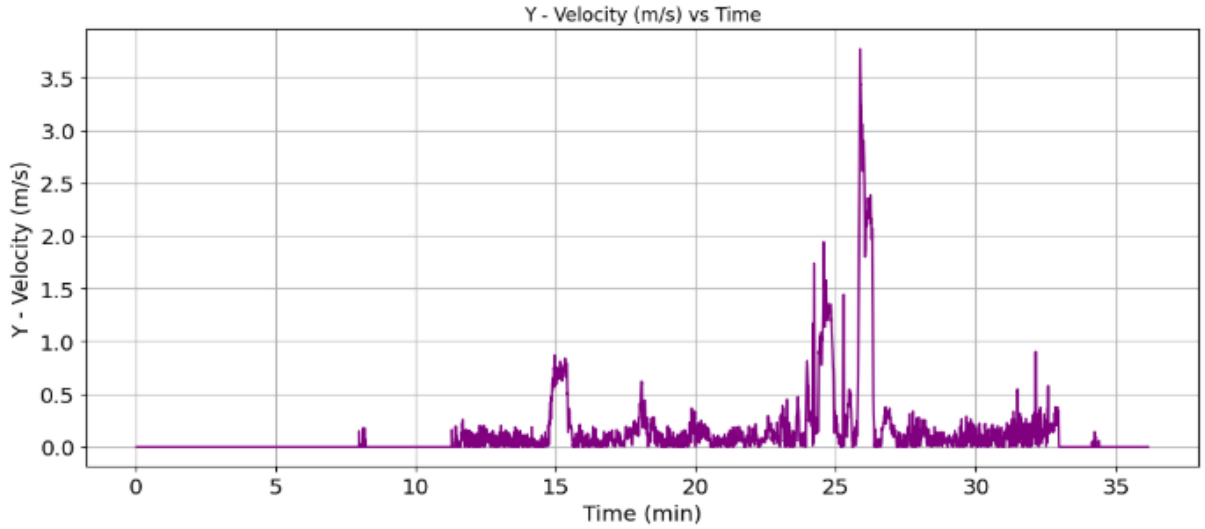


Figure 3.10 Aircraft velocity along the y-axis (latitude).

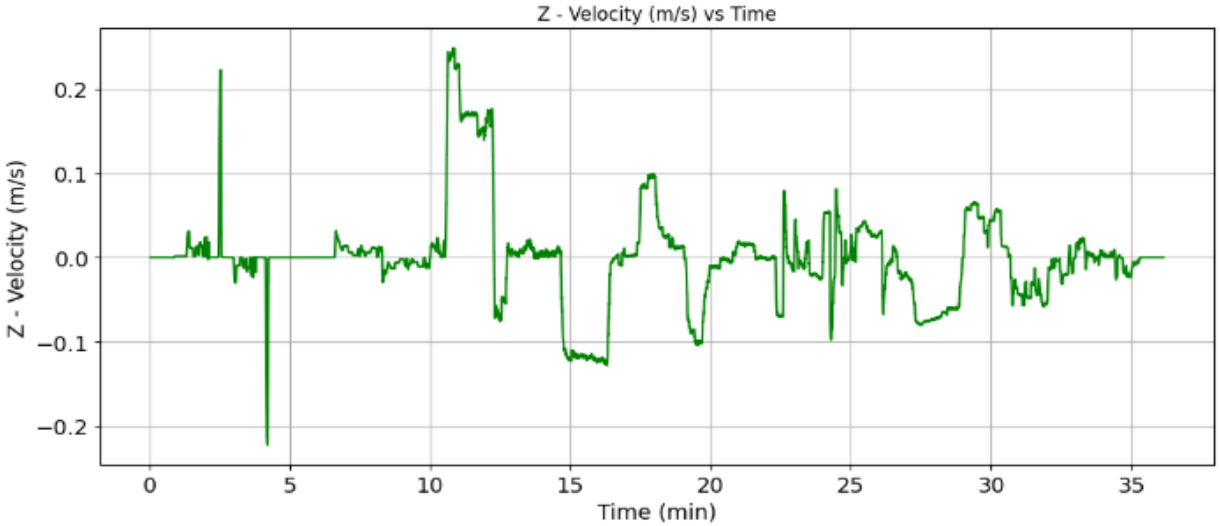


Figure 3.11 Aircraft velocity along the z-axis (normal).

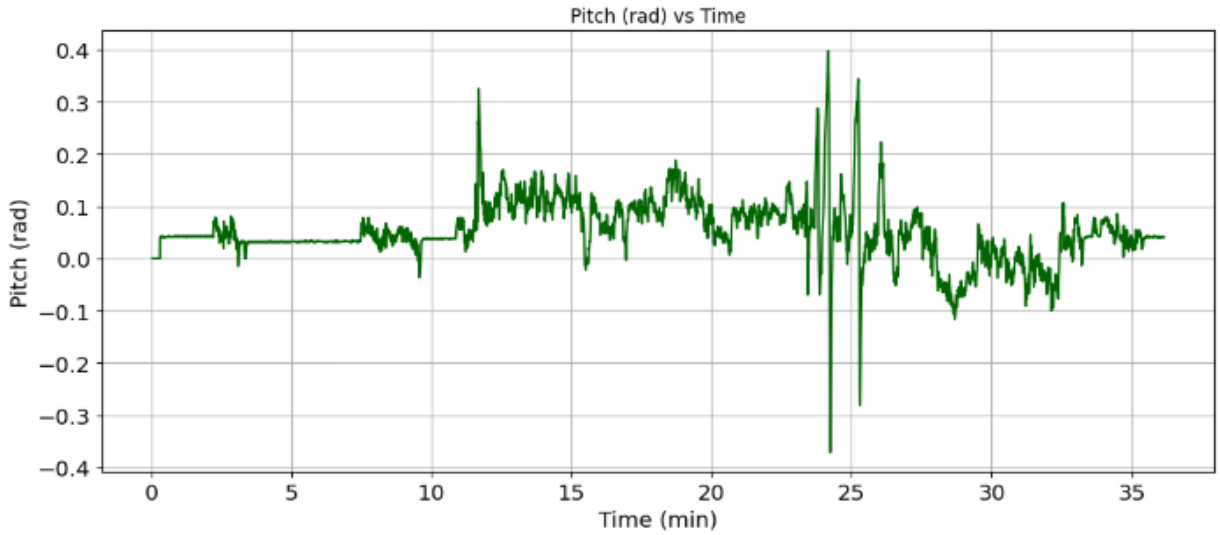


Figure 3.12 Pitch angle profile.

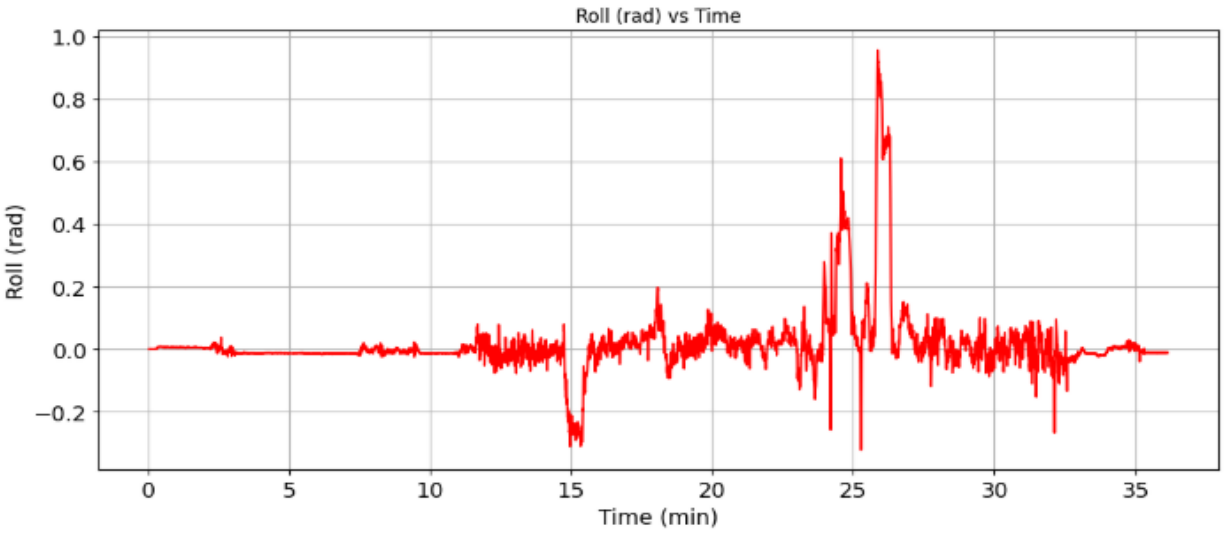


Figure 3.13 Roll angle profile.

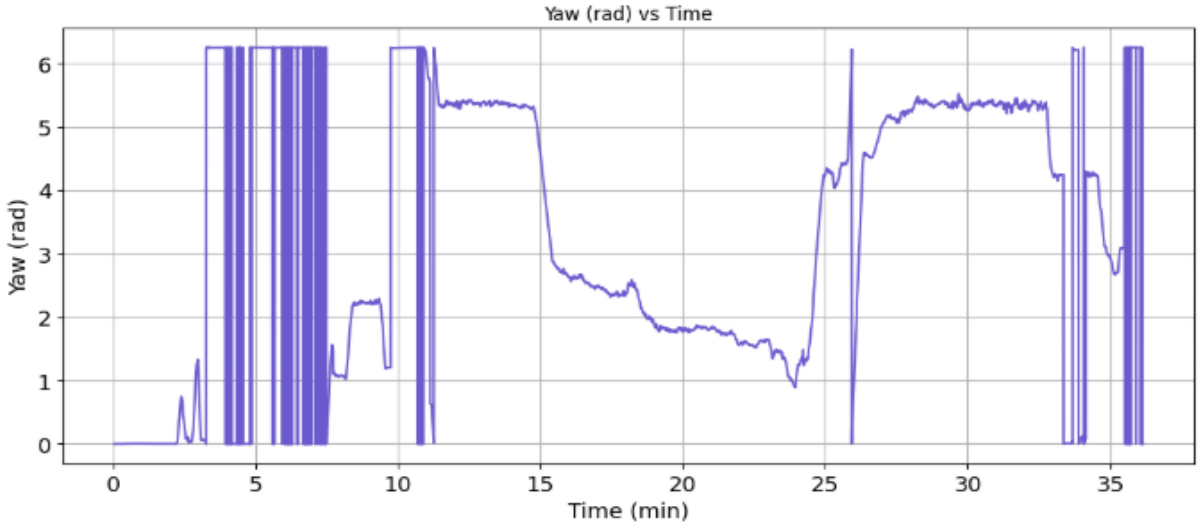


Figure 3.14 Yaw angle profile.

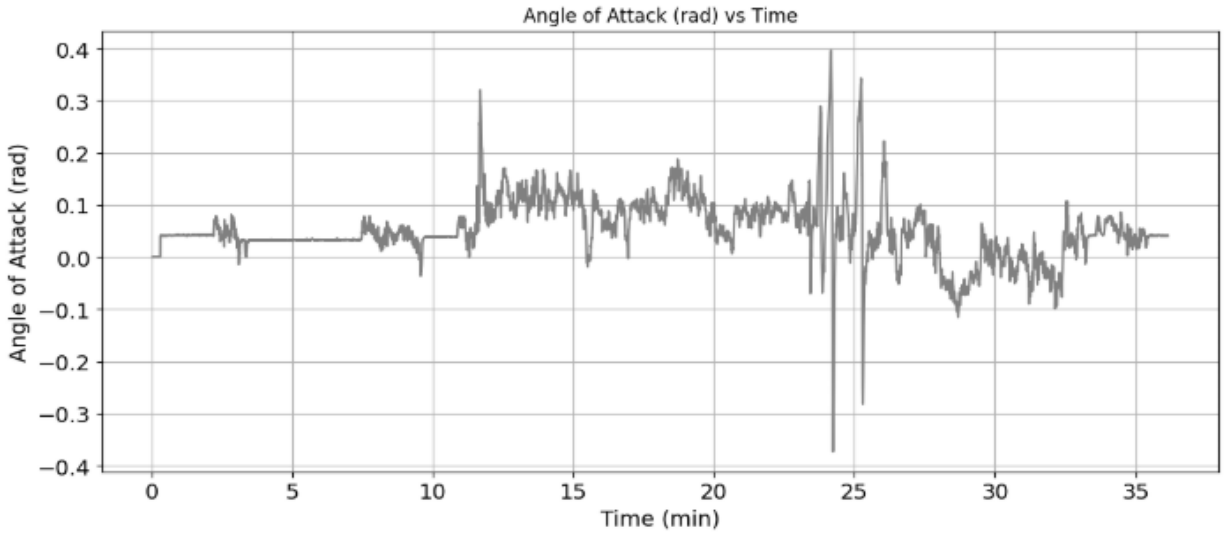


Figure 3.15 Angle of attack.

The results obtained are illustrated in Figures (3.16–3.21), along with the actual rotational speed and motor power extracted from the dataset. In the estimated thrust profile, the thrust peaks during take-off, when it must overcome drag and rolling resistance and provide the force necessary for acceleration and lift-off. It then decreases gradually during cruise and reaches zero once the aircraft comes to a stop after landing.

The rotational speed shows slight variations even when the aircraft is stationary, which can be attributed to pre-flight checks. As the aircraft begins to move, the rotational speed increases, peaks during take-off, and returns to zero after landing. The trends of the estimated and actual rotational speed profiles are similar; however, the estimated values exceed the motor speed limit of 2500 RPM because propulsive efficiency was not initially considered. The comparison between the estimated and measured rotational speeds is shown after incorporating the propeller efficiency correction. The efficiency of the Pipistrel Velis Electro propeller reaches a maximum of about 85%, as shown in Figure 9. For this analysis, an average propeller efficiency of 75% was considered. This efficiency was accounted for in terms of the effective propeller power, so that the computed rotational speed reflects the actual power transmitted through the propeller rather than the total motor output. When this efficiency correction was applied, the estimated rotational speed closely followed the measured motor RPM throughout the flight, confirming that the adjustment provides a realistic representation of propeller performance. The difference curve indicates moderate deviations from zero for most of the flight period, with larger variations observed during transitional segments such as power adjustments and descent.

The estimated torque profile generally follows the same pattern as the rotational speed. The torque reaches its peak during take-off and remains below the upper limit of 220 Nm for the rest of the flight. The power comparison plot illustrates the relationship between the commanded power and the shaft power. The commanded power represents the electrical power delivered to the motor, while the shaft power corresponds to the mechanical power output of the motor used to drive the propeller. The shaft power values are consistently lower than the commanded power due to the inclusion of the combined efficiency of the inverter and motor, which together yield an overall efficiency of approximately 86%. This means that only about 86% of the electrical power supplied to the motor is converted into mechanical output. Consequently, the difference observed between the two power curves reflects the influence of these efficiency factors. Despite this offset, the shaft power follows the same overall trend as the commanded power throughout the mission, demonstrating that the model accurately represents the power flow within the propulsion system.

Most of the oscillations observed in these plots arise from the inclusion of the aircraft's orientation angles in the computation. Since these angles vary continuously and often fluctuate significantly over short time periods, their influence introduces noticeable oscillations in the calculated parameters.

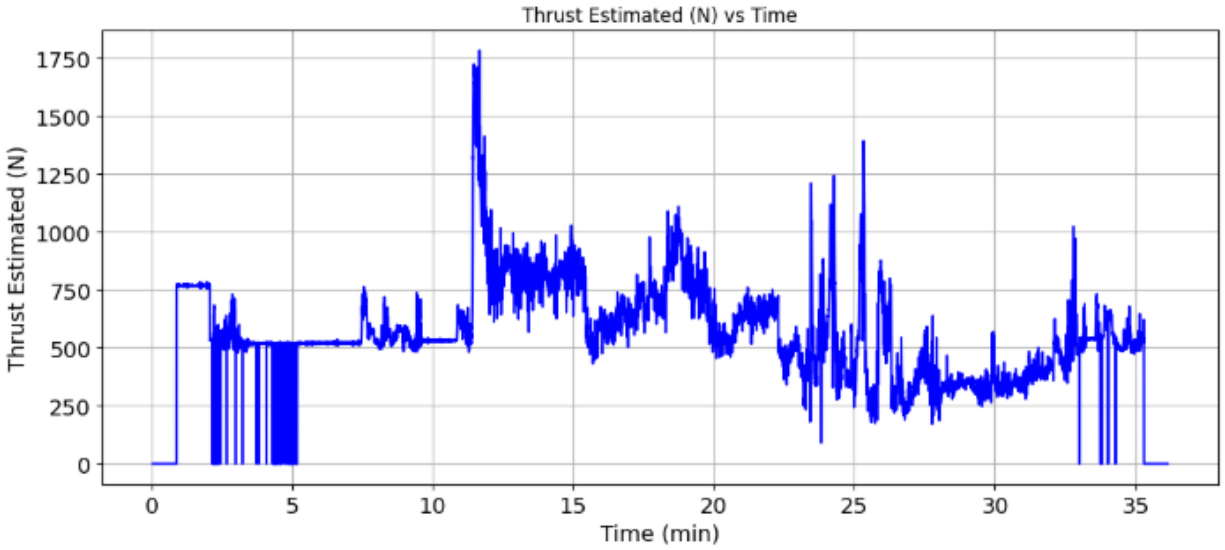


Figure 3.16 Estimated propeller thrust.

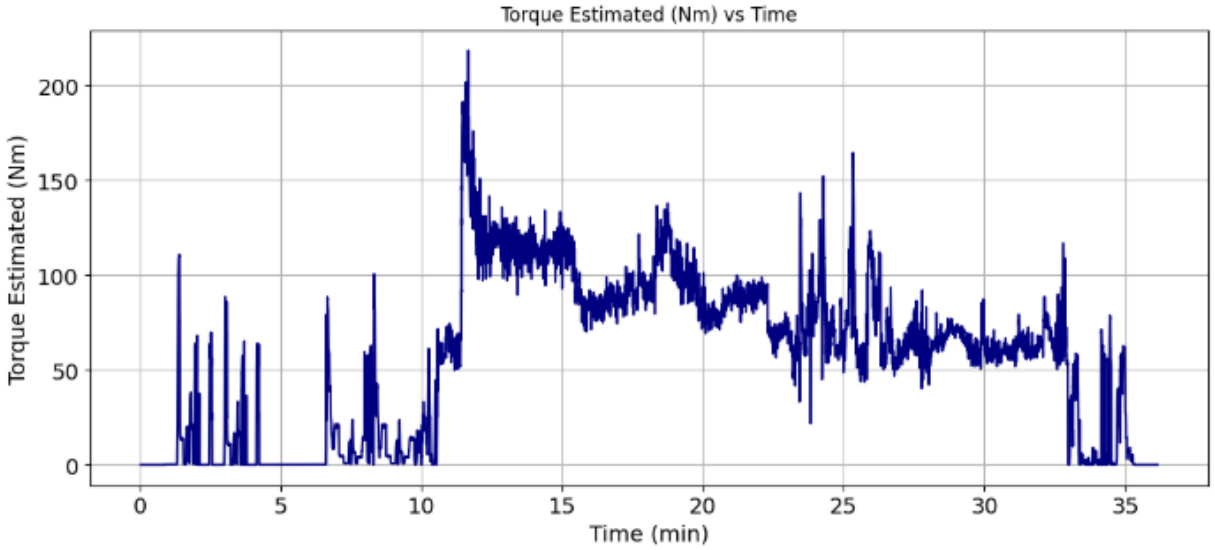


Figure 3.17 Estimated propeller torque.

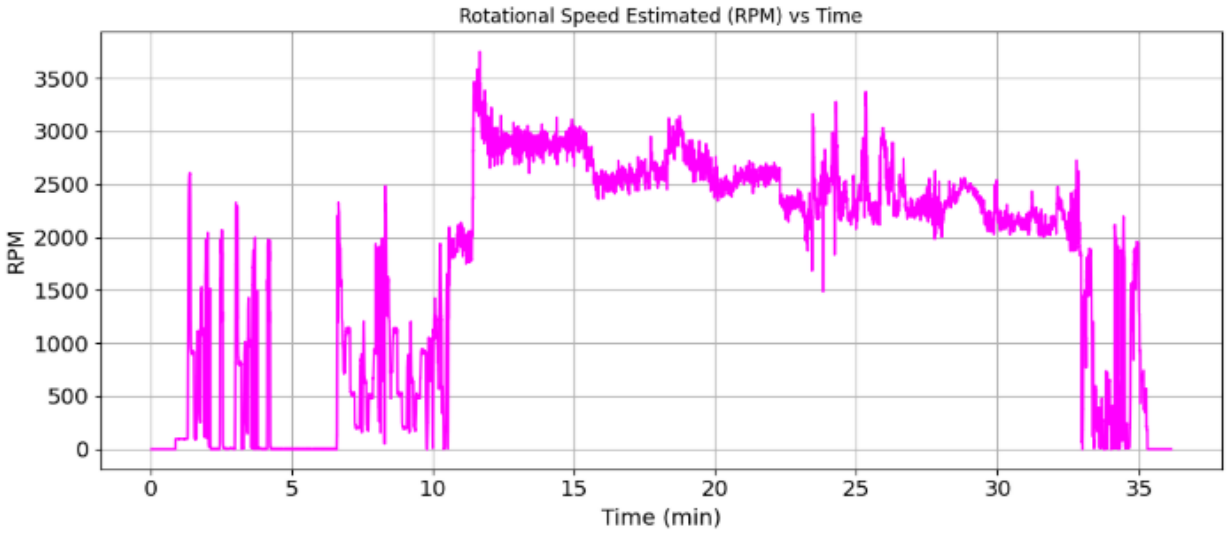


Figure 3.18 Estimated propeller and motor rotational speed.

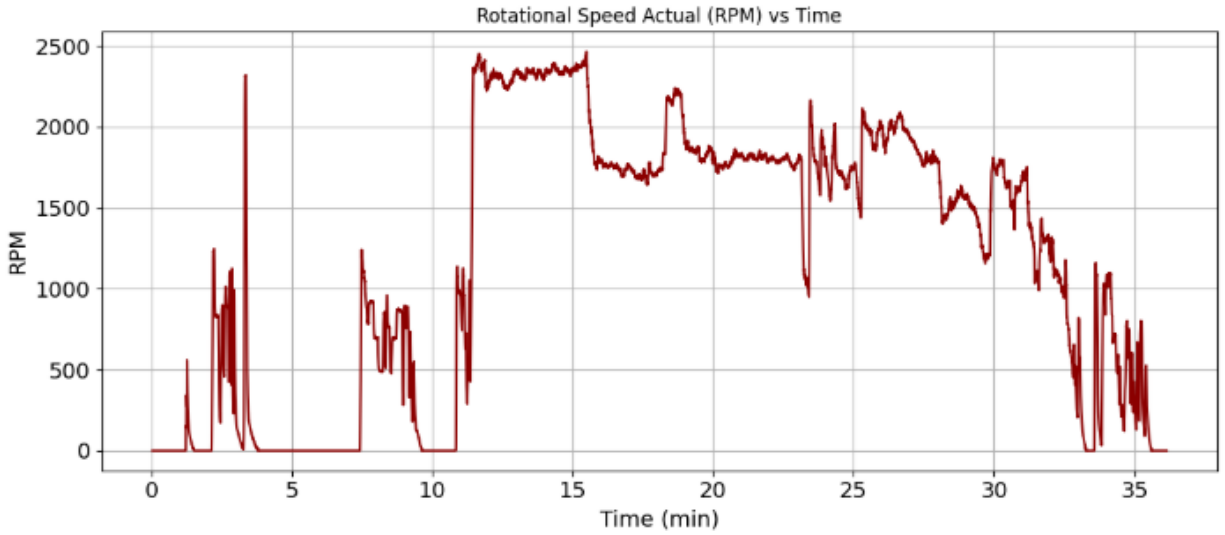


Figure 3.19 Actual propeller and motor rotational speed.

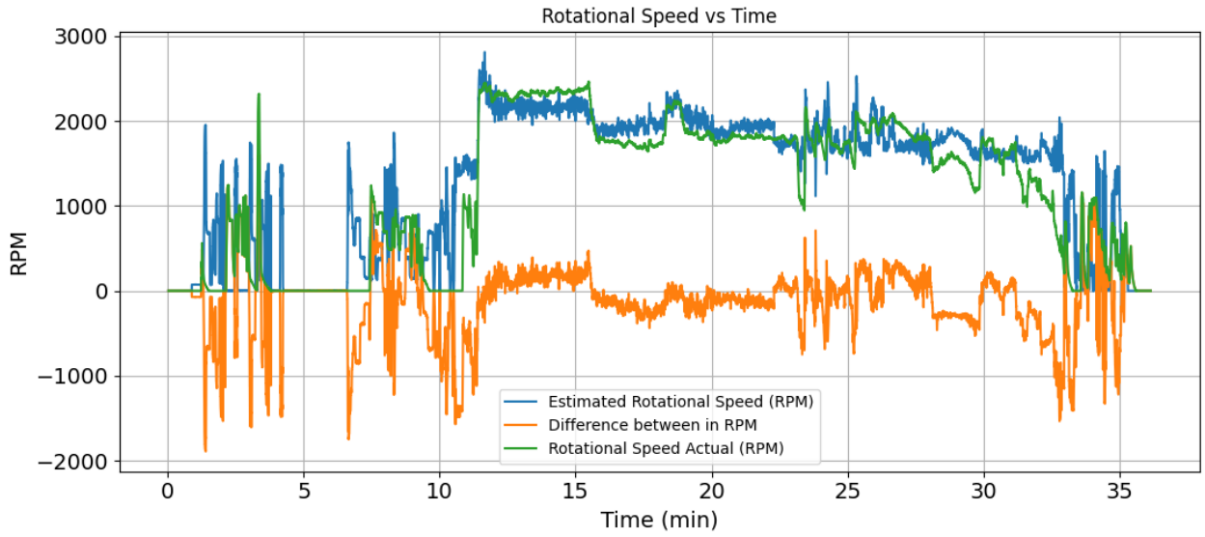


Figure 3.20 Comparison between actual rotational speed and estimated rotational speed (after considering propeller efficiency).

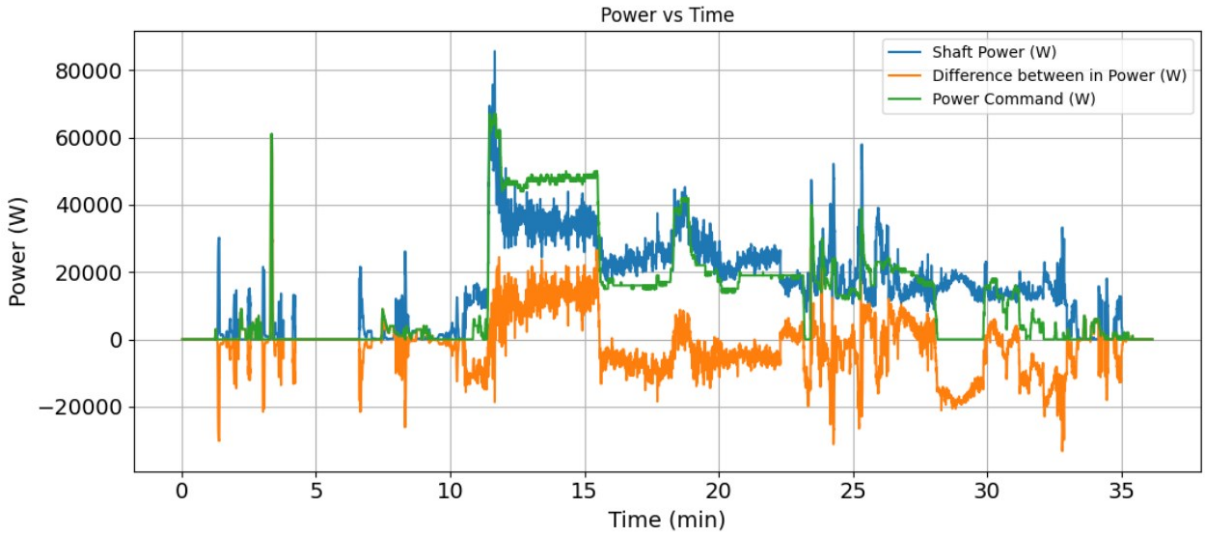


Figure 3.21 Comparison between commanded and shaft power.

3.2 Motor Power Command (MPC) Approach

The power command mode represents the condition in which the pilot directly controls the shaft power supplied to the motor through throttle input. This approach focuses on the response of the propeller under a specified power command, rather than determining the thrust from the overall aircraft motion.

The computations are therefore based on the commanded power, measured airspeed, and altitude-dependent air density, together with the tabulated propeller performance coefficients.

In this mode, only the thrust component acting along the longitudinal (x) axis, representing the forward propulsive force is considered. The pitch angle, which influences altitude change, is implicitly accounted for through the variation in altitude data, while the roll and yaw angles are not considered because they mainly affect lateral dynamics and lift distribution.

3.2.1 Methodology

This section describes the steps used to determine the propeller's rotational speed, thrust, and torque for each time sample of the flight data. The procedure begins with data corrections to ensure consistency of the inputs, followed by the numerical determination of rotational speed using Brent's Method, thrust evaluation from the coefficient plots, and the computation of aerodynamic torque and power.

1. Data Processing and Atmospheric Correction:

- The raw flight dataset was first pre-processed to ensure consistency of units and sampling. The pressure altitude (PA) was converted to the altitude with respect to the airport ground by subtracting a constant offset of 1050 ft from pressure altitude data to account for the local elevation above sea level as described in section 2.2.1. The result was then converted to meters.
- To compute the variation of air properties with altitude, an isothermal approximation is applied at each time step using the measured outside air temperature (OAT) provided in the dataset. This means that the temperature is treated as constant for the small altitude change corresponding to that time instant, allowing a simplified relation for pressure variation with height. The QNH (sea-level pressure) and OAT values from the dataset are used to determine the local static pressure and air density.

  The absolute temperature is calculated as:

$$T = \text{OAT} + 273.15\ \text{K}, \tag{3.21}$$

The pressure at altitude $h$is then determined using the hydrostatic relation:

$$p(h) = p_0 \exp\left(-\frac{gh}{RT}\right), p_0 = QNH \times 100 \tag{3.22}$$

where $R = 287.05$ J/(kg·K) is the specific gas constant for air and $g = 9.80665$ m/s² the gravitational acceleration.

Once the local pressure is obtained, the air density is computed using the ideal gas law:

$$\rho(h) = \frac{p(h)}{RT} \tag{3.23}$$

This method allows the aerodynamic parameters such as thrust, torque, and true airspeed to be evaluated using the actual flight conditions at each time step, ensuring that atmospheric effects on performance are accurately represented.

- The indicated airspeed (IAS) and ground speed (GS) were converted to meters per second. The true airspeed (TAS) was then obtained from the IAS using the density ratio:

$$TAS = IAS\sqrt{\frac{\rho_0}{p(h)}}, \rho_0 = 1.225\ kg/m^3 \tag{3.24}$$

These corrections ensure that the aerodynamic parameters are consistent with actual flight conditions.

2. Propeller Aerodynamic Model:

Propeller performance is described using dimensionless aerodynamic coefficients $C_t(J)$ and $C_q(J)$ tabulated as functions of the advance ratio, as described in section 3.1.2. Refer to equations (3.14-3.16) for coefficient relations. The angular velocity (ω) and RPM (n) are related through the following relation:

$$\omega = \frac{2\pi n}{60} \tag{3.25}$$

3. Determination of Rotational Speed:

For each time sample, the propeller's rotational speed n is determined depending on whether the operation is powered or windmilling.

(a) Powered Operation

When the motor delivers positive shaft power $P_{\text{shaft}} > 0$, n is found by solving the nonlinear power balance equation:

$$P_{\text{shaft}} = \rho\, n^3 d^5\, C_p(\frac{V}{nd}) \tag{3.26}$$

where P_{shaft} is the shaft power, ρ the air density, n the propeller rotational speed, C_p the power coefficient, V the aircraft velocity, and d the propeller diameter.

Since C_p depends on n through advance ratio, this equation cannot be solved analytically. Therefore, a numerical root-finding method is used to obtain the value of n that satisfies the equation for each time step.

Brent's Method:

Brent's Method is a hybrid root-finding algorithm that combines the reliability of the bisection method with the rapid convergence of secant and inverse quadratic interpolation methods.

The solver begins with a lower bound, n_{min}, and upper bound, n_{max}. It evaluates the function:

$$r(n) = P_{\text{shaft}} - \rho\, n^3 d^5\, C_p\left(\frac{V}{nd}\right) \tag{3.27}$$

A valid bracket exists when the function values at the two ends have opposite signs:

$$r(n_{\text{min}})\, r(n_{\text{max}}) < 0 \tag{3.28}$$

This condition ensures that the true root lies between the bounds. Brent's method then iteratively refines the solution by selecting the next point using a combination of interpolation and bisection. When the function behaves smoothly, interpolation is used to accelerate convergence; otherwise, bisection guarantees progress toward the root.

The algorithm continues until the residual magnitude $|\, r(n)\,|$ is less than a predefined tolerance (typically 10^{-6}), indicating convergence. If a sign change cannot be found within the chosen bounds, a bounded minimization of $|\, r(n)\,|$ is performed to identify the rotational speed that minimizes the power mismatch.

Brent's method was selected because it provides both stability and speed. It is particularly effective for nonlinear aerodynamic equations that are continuous but not easily differentiable. Its robustness makes it suitable for real-time aerodynamic modelling and propeller simulations where the function behaviour is complex and coefficients are empirically derived [49].

(b) Windmilling / Idle Condition

When the shaft power becomes zero or negative ($P_{\text{shaft}} \leq 0$), the propeller is assumed to rotate freely under aerodynamic forces until the net torque on the blades equals zero. This condition is represented as

$$C_q(\frac{V}{nd}) = 0 \tag{3.29}$$

The same solver is applied to determine the corresponding rotational speed, n, or alternatively, the value that minimizes $| C_q |$ if a zero crossing cannot be found within the chosen range. This represents the equilibrium rotational speed at which the aerodynamic driving torque balances the resisting torque of the propeller system.

Note that even though regeneration is potentially possible during wind milling periods, this function is disabled in Velis Electro aircraft due to certification issues that are yet to be resolved.

4. Thrust Estimation:

After determining the rotational speed n from the powered or windmilling solver, the propeller thrust is computed directly from the coefficient table using n. The steps at each time sample are:

1. Advance ratio for thrust evaluation:

$$J_t = \frac{V}{nd}, \tag{3.30}$$

where J_t is the advance ratio corresponding to this thrust, V, the aircraft velocity, n the propeller rotational speed and d the propeller diameter.

2. Thrust coefficient determination:
   The thrust coefficient corresponding to this advance ratio is obtained from the thrust coefficient plot.

3. Dimensional thrust:
   Thrust is the computed from equation (3.14).

This yields the forward thrust acting along the longitudinal axis for the given power setting.

5. Accounting for Propulsive Efficiency:

Comparison between estimated and measured motor RPM revealed that their difference was not constant, but their ratio remained approximately constant throughout the flight. The ratio $\frac{\text{RPM}_{\text{actual}}}{\text{RPM}_{\text{estimated}}}$ stabilized around 0.75, indicating that the propeller operates at roughly 75% propulsive efficiency.

Hence, the estimated RPM is multiplied by this efficiency factor as given by (3.31).

$$\mathrm{RPM_{adj}} = 0.75 \times \mathrm{RPM_{estimated}}, \tag{3.31}$$

Physically, this means that only 75 % of the shaft power is effectively converted into propulsive power at the propeller. Since mechanical power is given by

$$P = Q\omega, \tag{3.32}$$

and torque Q remains constant for a given aerodynamic condition, the reduction in power due to efficiency directly affects the rotational speed:

$$\frac{P_{\text{actual}}}{P_{\text{ideal}}} = \frac{\omega_{\text{actual}}}{\omega_{\text{ideal}}} = 0.75 \tag{3.33}$$

Thus, the observed 0.75 ratio in RPM corresponds to the same 75% efficiency in power transmission from the motor to the propeller.

6. Aerodynamic Torque Estimation:

Two propeller torque values (estimated and actual) are computed at each time sample to ensure consistency between estimated value and actual data.

(a) Estimated Propeller Torque (from coefficients)

Using the adjusted rotational speed n_{eff}, the effective advance ratio is computed through (2.5) and the estimated aerodynamic torque through (3.15).

(b) Actual Propeller Torque (from measured RPM)

Using the actual RPM from the flight dataset, the corresponding actual aerodynamic torque is computed by first finding J through (2.5) and then Q through (3.15).

Both torque values are derived from the same coefficient curve to maintain consistency.

3.2.2 Simulation Results

The power command method is implemented on two flight profiles: a normal flight mission and a touch-and-go flight mission. Their simulation results are presented below.

Normal Flight Mission:

Figures (3.22–3.24) represent the input parameters used in the simulation for the normal flight mission, which includes a typical take-off, cruise, and landing sequence. These datasets were provided as inputs to the power command algorithm to evaluate the propeller performance for this flight profile.

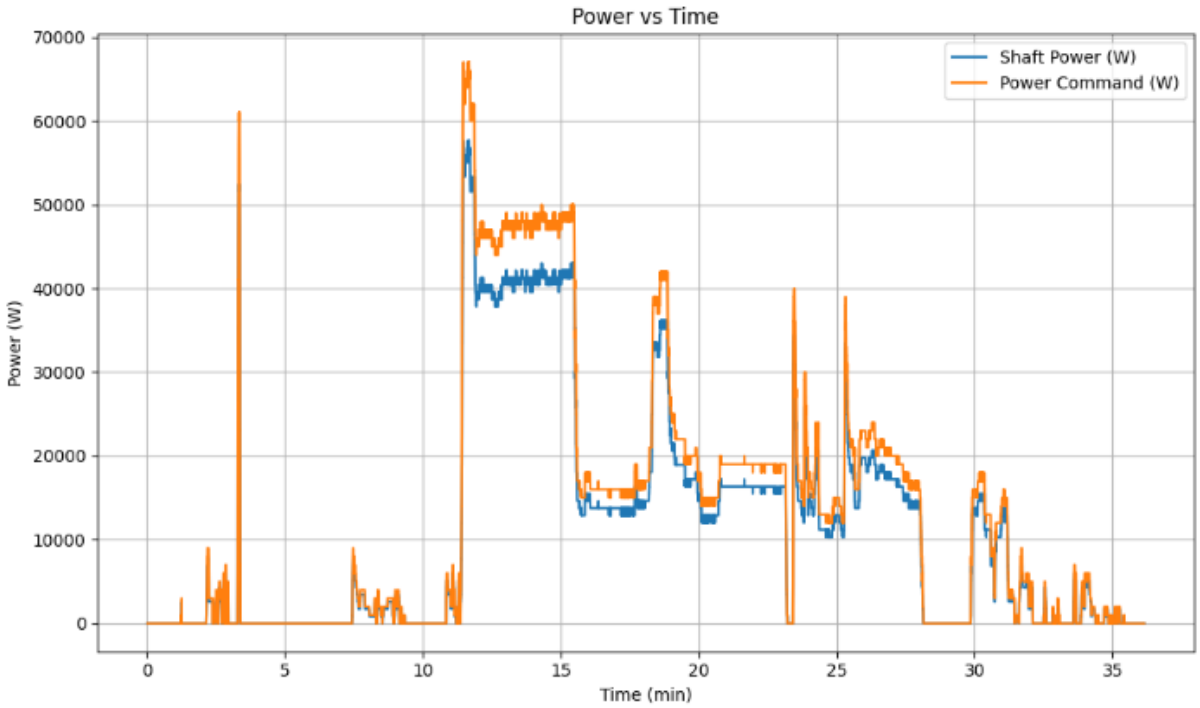


Figure 3.22 Pilot power command for normal flight.

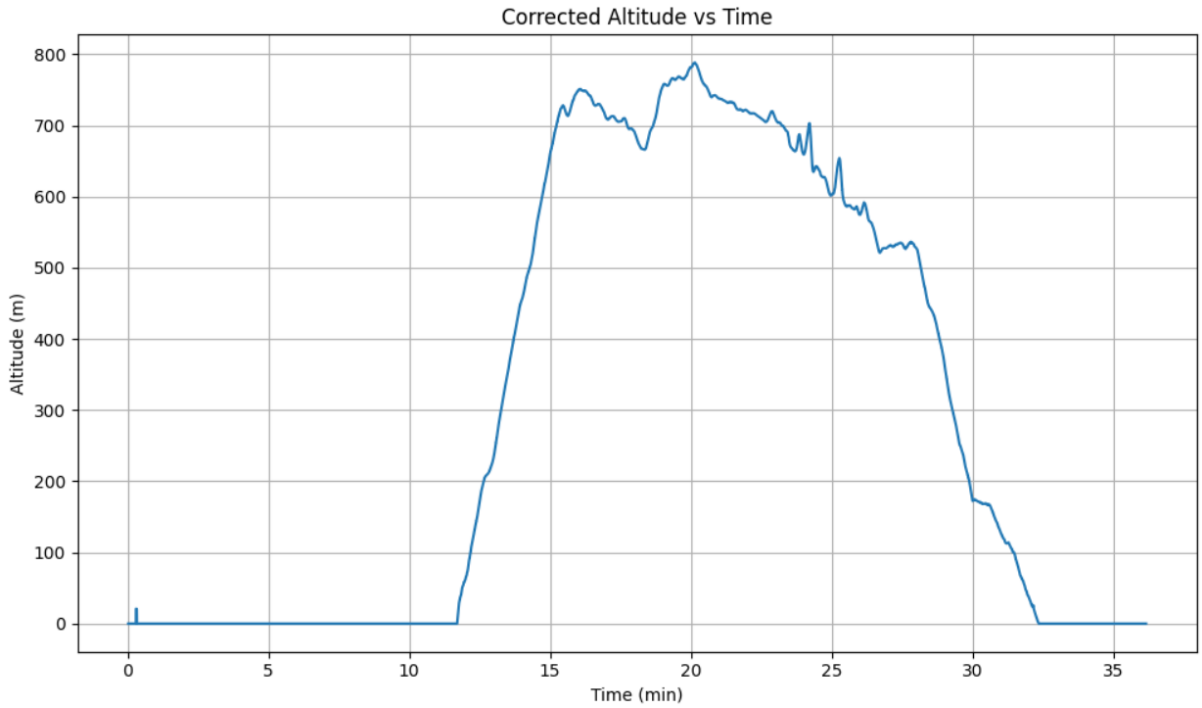


Figure 3.23 Aircraft altitude for normal flight.

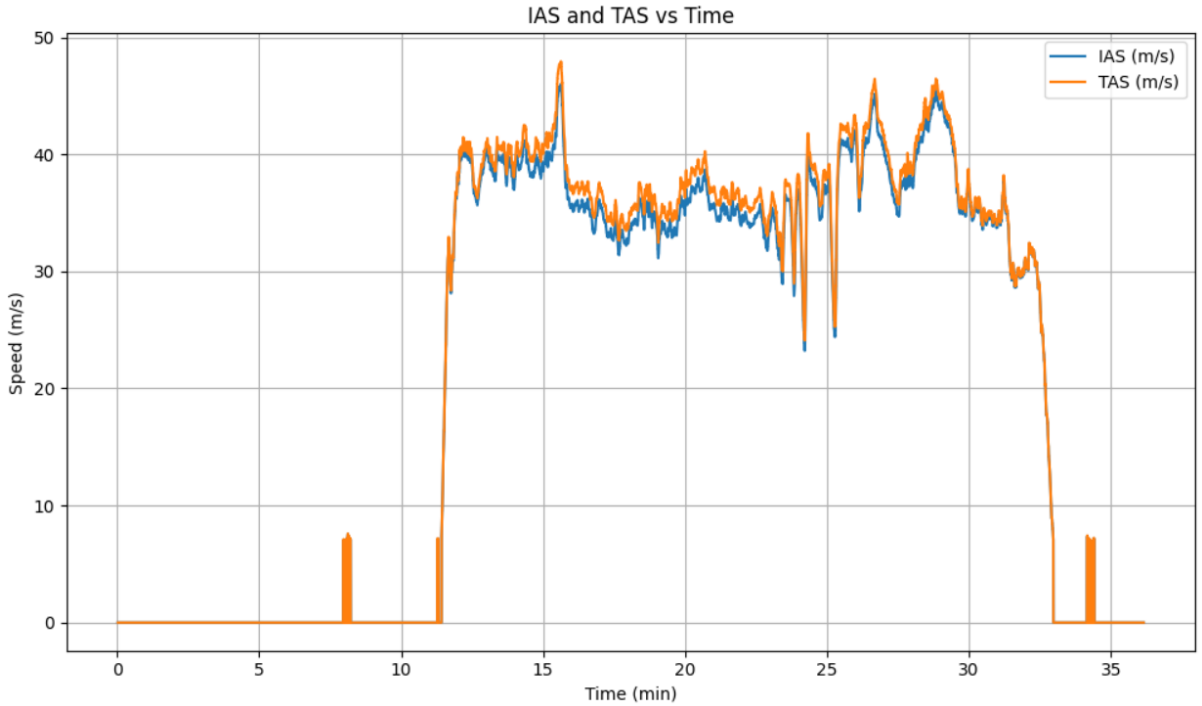


Figure 3.24 Aircraft's Indicated Air Speed (IAS) and True Air Speed (TAS) for normal flight.

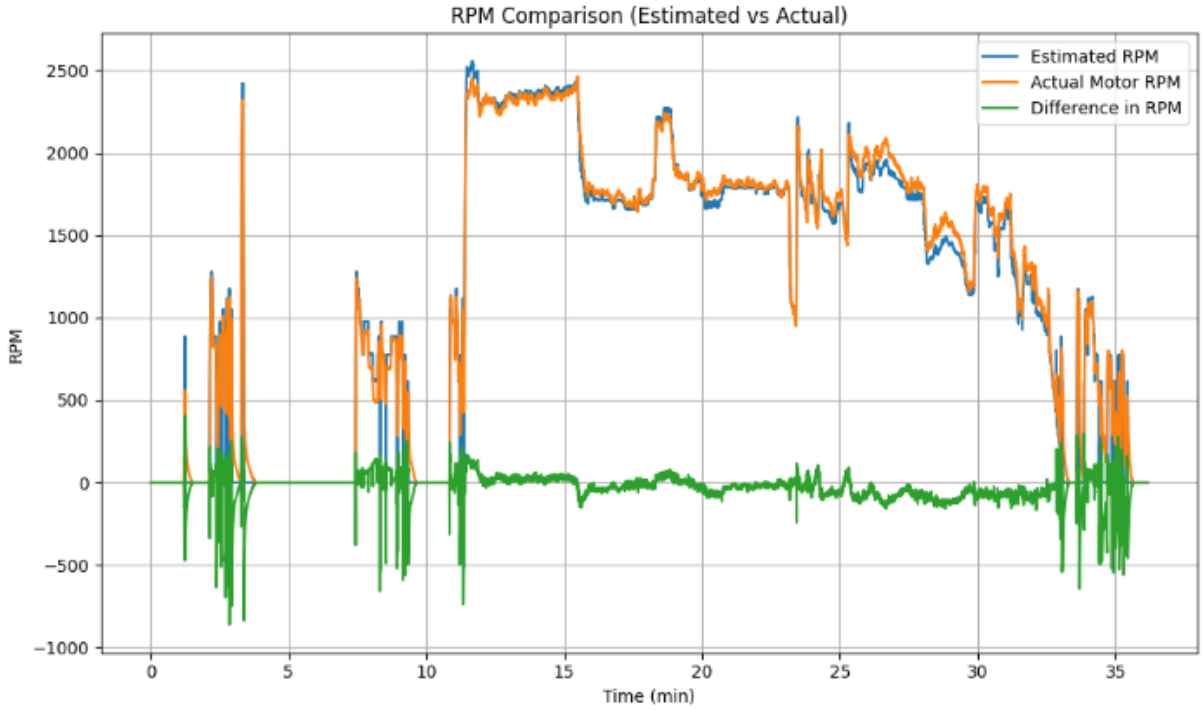


Figure 3.25 Comparison between actual and estimated motor rotational speed for normal flight.

During the powered portions of the flight (take-off, climb, and cruise) the estimated and measured motor speeds exhibit closely matching profiles, confirming the consistency of the numerical solver and coefficient interpolation. The small fluctuations between the two curves arise primarily from instantaneous variations in power input and airspeed, which affect the advance ratio and aerodynamic coefficients.

The estimated RPM remains slightly lower than the measured values throughout most of the flight, reflecting the combined influence of electrical and mechanical losses that are not explicitly modelled in the aerodynamic formulation. After applying the constant scaling adjustment established earlier, the difference between the two traces (shown in green) oscillates around zero, indicating that the solver accurately tracks the physical system dynamics. This agreement validates the reliability of the propeller speed estimation under pilot-commanded power conditions.

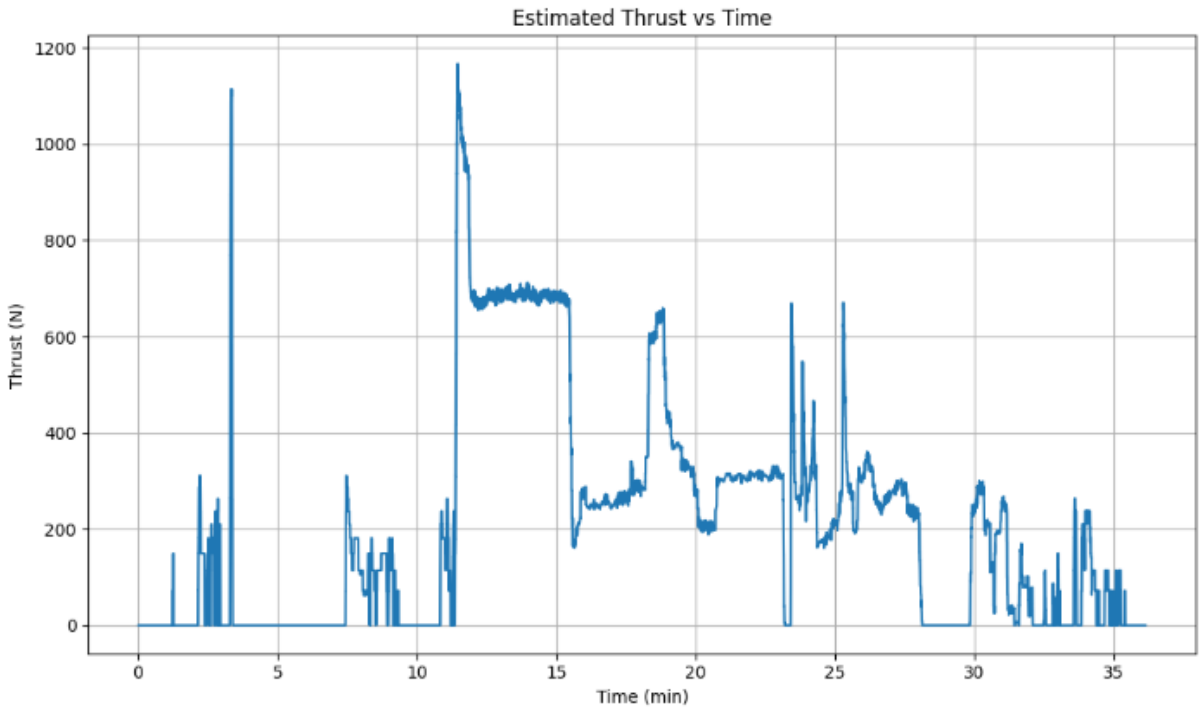


Figure 3.26 Estimated propeller thrust for normal flight.

At take-off (~10 min), thrust peaks at around 1000–1200 N, sufficient for aircraft acceleration and climb initiation. During steady cruise (15–25 min), thrust stabilizes between 300 and 700 N, balancing aerodynamic drag to maintain the desired altitude and speed. The reduction of thrust beyond 27 min indicates power-off descent and idle gliding, where thrust occasionally drops close to zero. The intermittent small spikes during descent correspond to brief power corrections or turbulence effects. These thrust levels are realistic for a light electric aircraft of the Velis Electro's mass (≈ 600 kg) and confirm that the propeller model reproduces plausible aerodynamic behaviour across all flight phases.

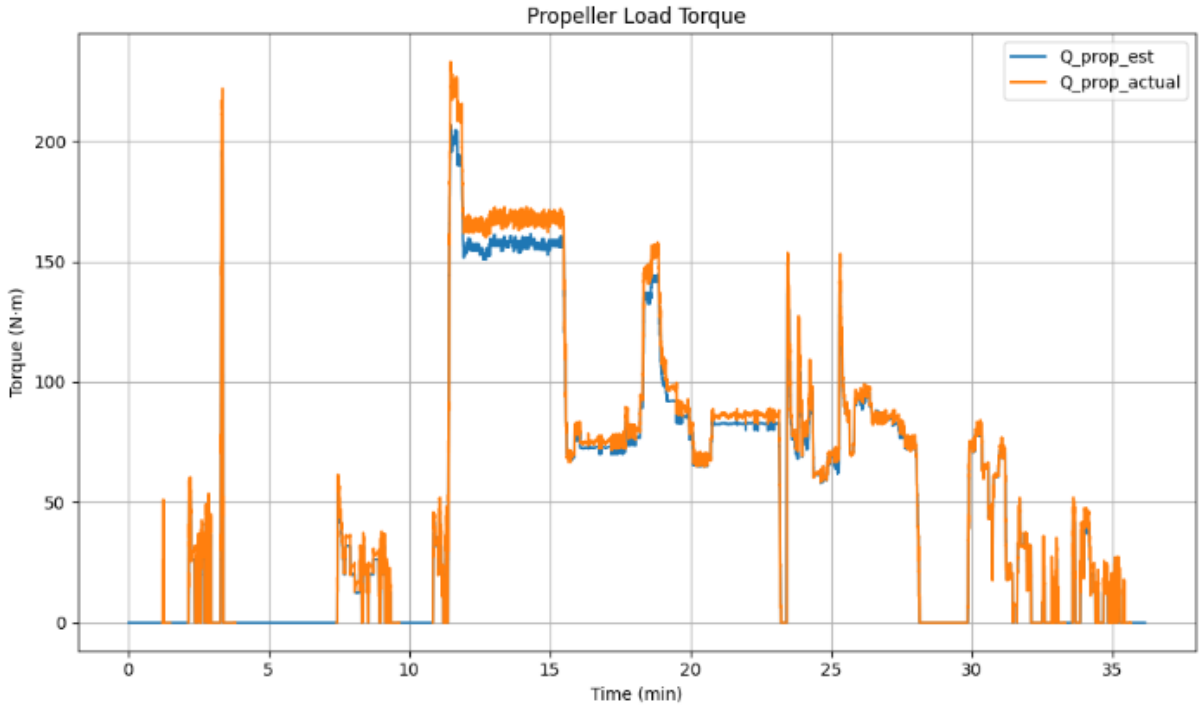


Figure 3.27 Estimated and actual load torque for normal flight.

The actual and estimated torque traces follow the same overall trend, confirming the consistency of the model. During take-off and climb, torque reaches around 200–220 N·m, corresponding to high thrust conditions and a large aerodynamic load on the motor shaft. During cruising (approximately 15–25 minutes), the torque varies between about 75 and 150 N·m, indicating reduced power demand under steady flight conditions. During descent and gliding, torque approaches zero, which is expected from the mechanical power relation given in equation (3.32), confirming that the propeller is windmilling with negligible net aerodynamic resistance. Although the aircraft continues to move due to its forward momentum, the absence of commanded power means that no mechanical work is transferred to the propeller. Since regeneration is not permitted in the Velis Electro due to certification requirements, the torque remains at zero instead of becoming negative when power input is removed. This explains the sections where torque values drop to zero even while the aircraft is still in motion.

Note that the spikes in thrust (Figure 3.26) and torque (Figure 3.27) at around 3 minutes correspond to a pre-flight test to make sure the propeller can produce its maximum power.

Touch-and-Go Flight Mission:

Figures (3.28–3.30) represent the input parameters used for the touch-and-go flight simulation. This flight mission consists of multiple take-offs, climbs, and descents, as evident from the repeated peaks and drops in altitude and power profiles.

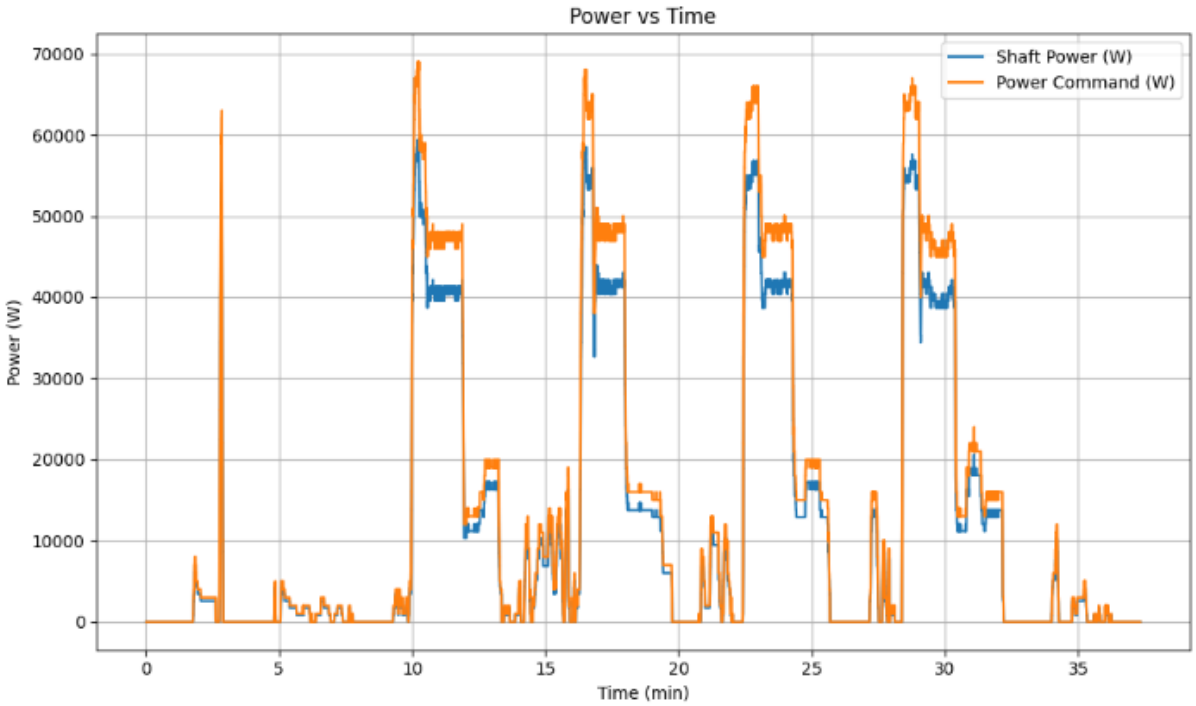


Figure 3.28 Pilot power command for touch-and-go flight.

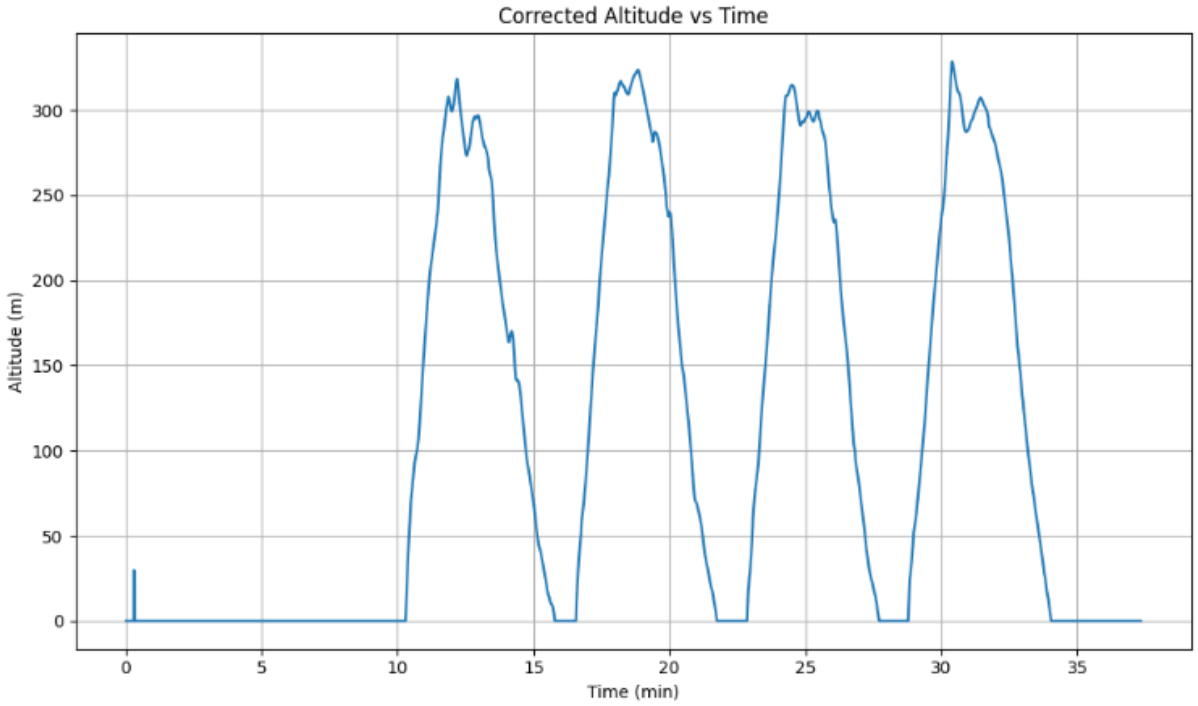


Figure 3.29 Aircraft altitude for touch-and-go flight.

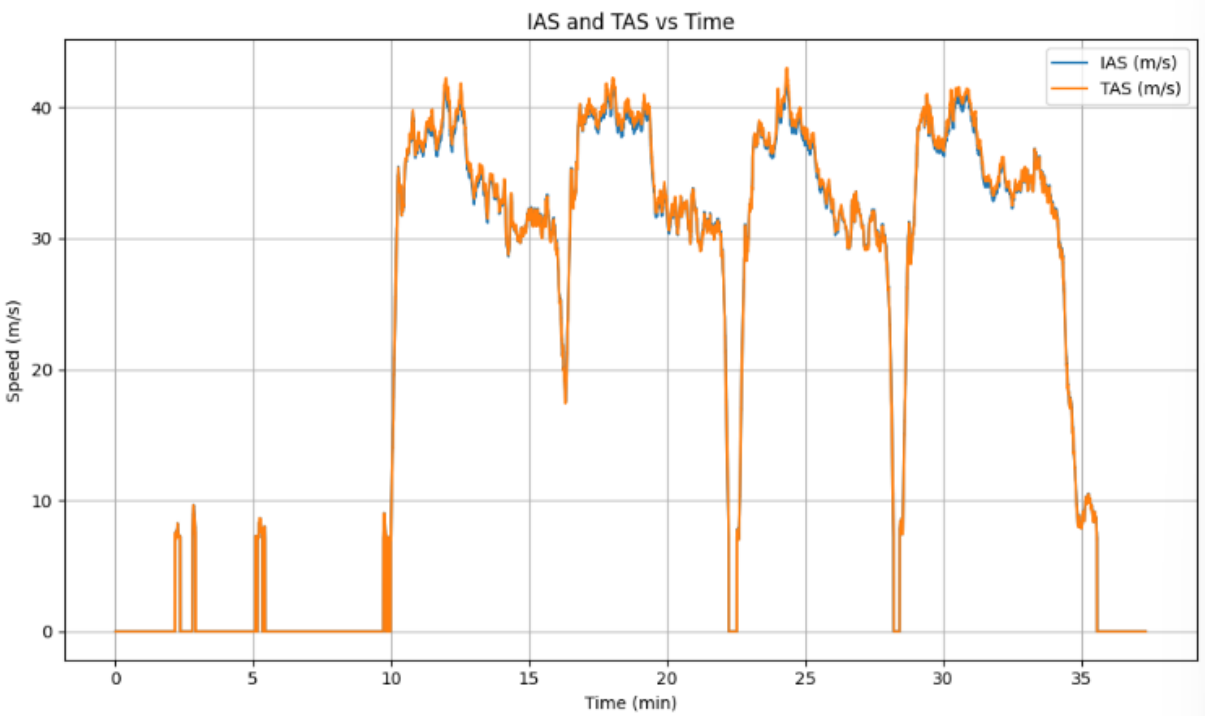


Figure 3.30 Aircraft IAS and TAS for touch-and-go flight.

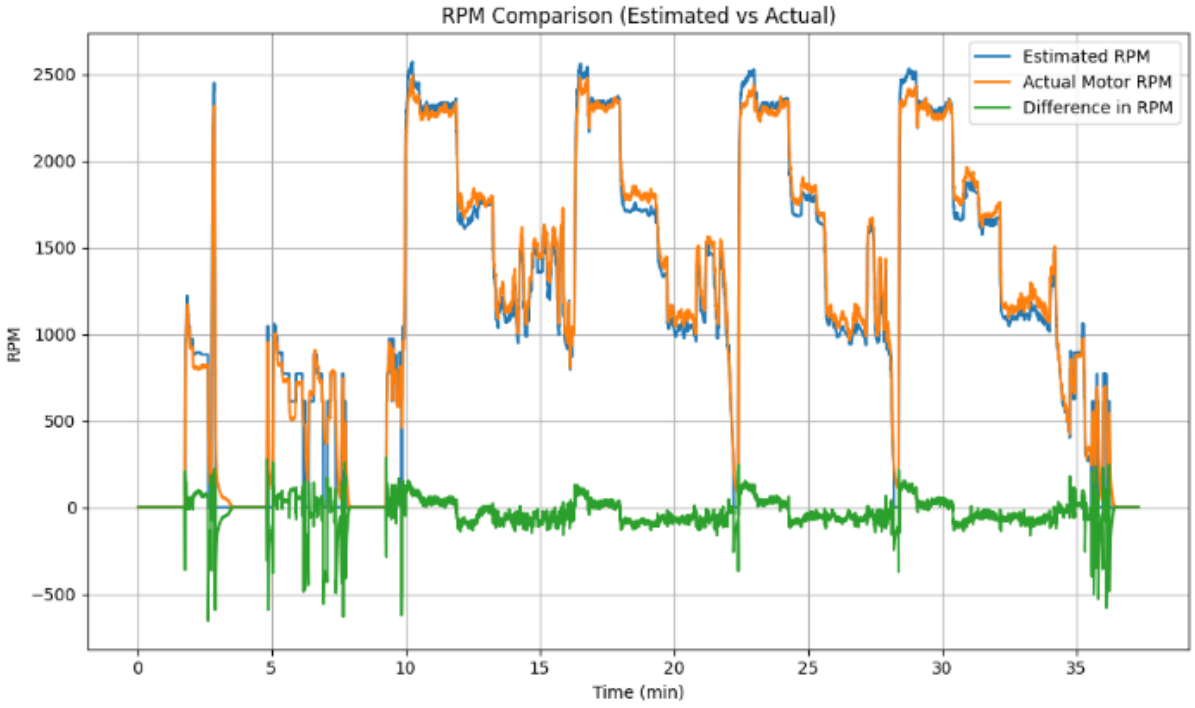


Figure 3.31 Comparison between actual and estimated motor rotational speed for touch-and-go flight.

The estimated RPM follows the measured motor speed closely across all manoeuvres, including sharp power changes during each take-off and descent. The alignment between the two RPM traces confirms that the solver responds well to fast variations in power and airspeed. The stable tracking across multiple cycles demonstrates that the model can reliably reproduce motor behaviour under dynamic flight conditions.

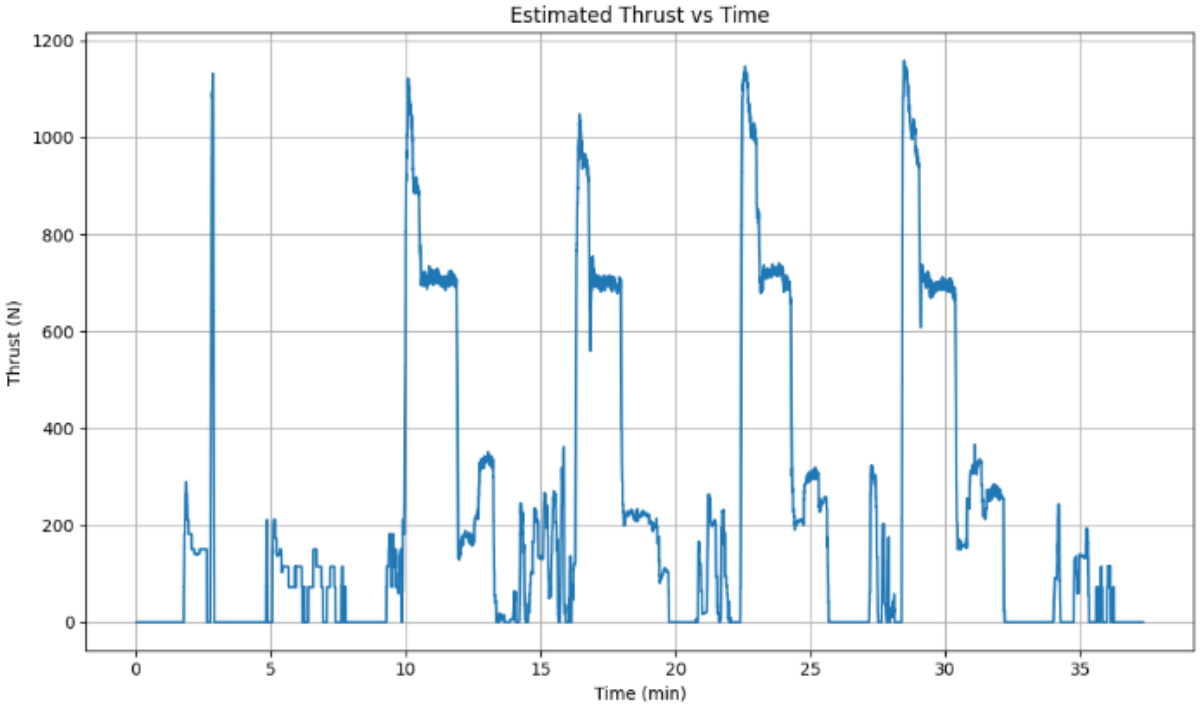


Figure 3.32 Estimated propeller thrust for touch-and-go flight.

The thrust curve rises and falls sharply during each take-off and descent, respectively, reflecting the expected aerodynamic response to throttle changes. The smooth transitions between power-on and power-off segments indicate that the solver correctly links propeller coefficients to fast-changing flight conditions. The results show that the model remains consistent and responsive across all phases of this rapidly changing flight profile.

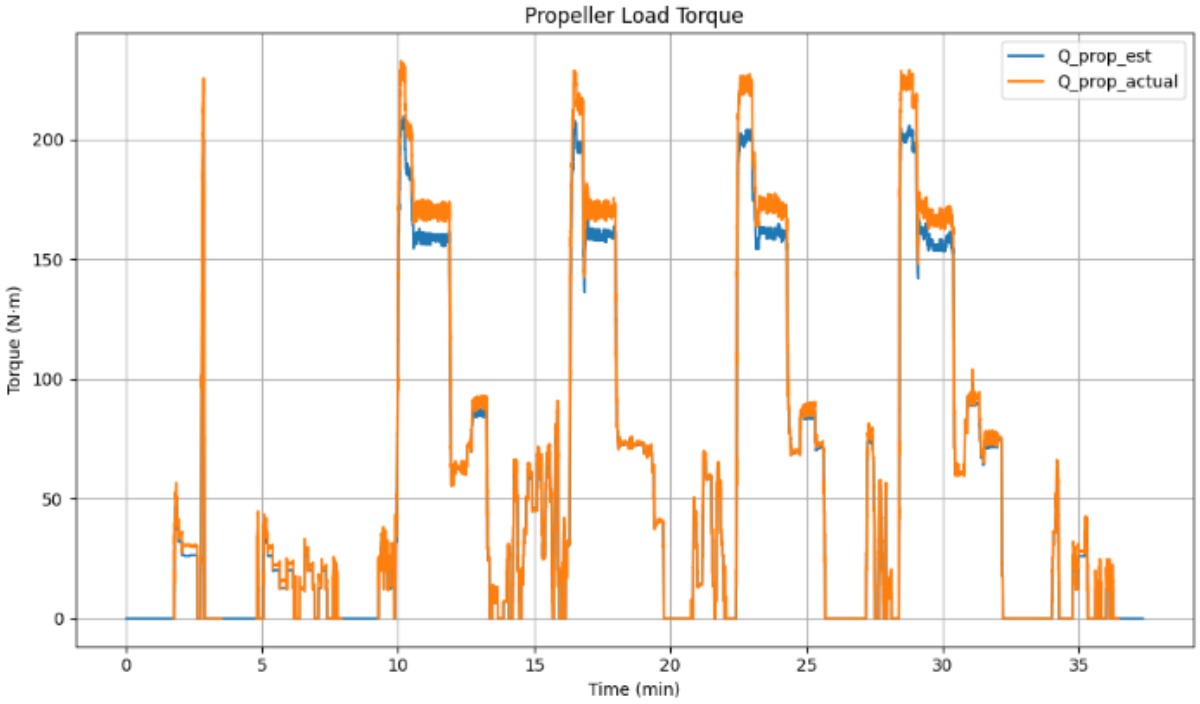


Figure 3.33 Estimated and actual load torque for touch-and-go flight.

The estimated torque aligns well with the torque derived from actual RPM data in every circuit. Both torque traces increase during take-off and decrease during descent, following similar trends throughout. This agreement confirms that the aerodynamic-coefficient-based approach captures real variations in propeller loading and maintains accuracy during consecutive manoeuvres. The results demonstrate that the methodology performs reliably even for quick, repeated operations such as touch-and-go missions.

3.2.3 RPM with Phase Regions

Normal Flight Mission:

The segmented RPM plot (Figure 3.34) for the normal flight mission illustrates the variation of estimated and measured motor speeds across all flight phases. The phase-coloured regions show that the model accurately identifies transitions between taxiing, take-off, climb, cruising, descent, and landing. The close agreement between the estimated and actual RPM values across these segments confirms that the solver captures the expected propulsion response throughout a standard mission profile.

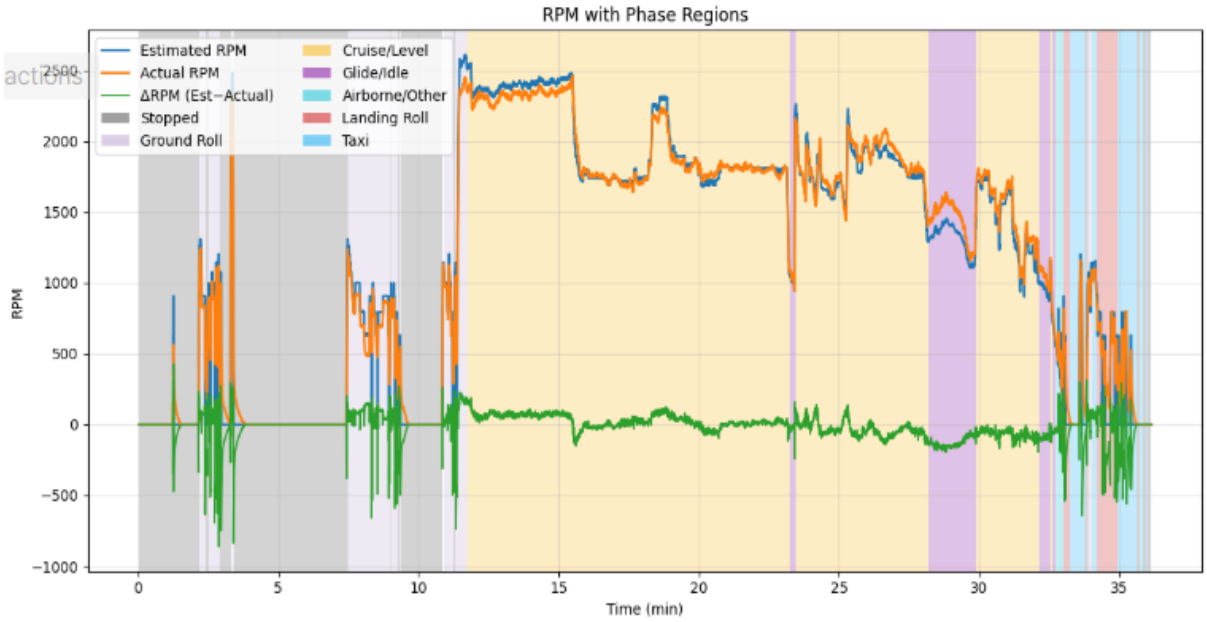


Figure 3.34 Normal flight RPM with phase distinction.

Touch-and-Go Flight Mission:

In the touch-and-go flight mission, the RPM profile displays multiple take-off and landing cycles characterized by rapid throttle variations (Figure 3.35). Despite these dynamic transitions, the model maintains stable and accurate tracking of motor speed while correctly identifying each phase change. The clearly defined coloured regions highlight the algorithm's ability to adapt to abrupt operational shifts, ensuring consistent and reliable phase classification even during successive touch-and-go manoeuvres.

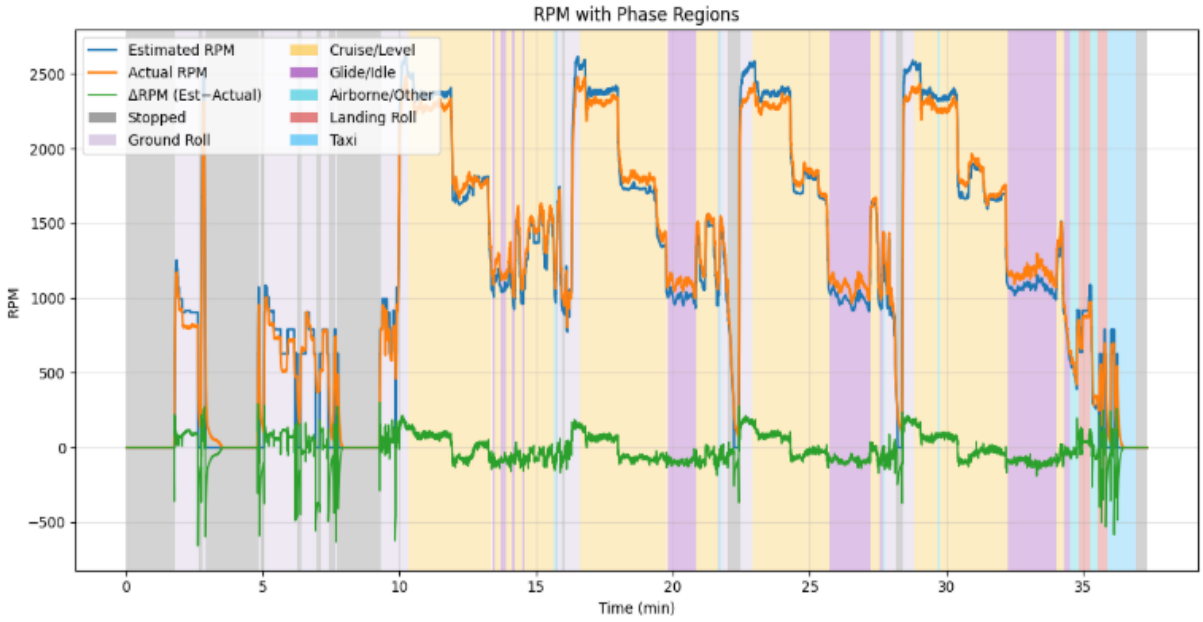


Figure 3.35 Touch-and-go flight RPM with phase distinction.

3.3 Conclusion

In this chapter, a mathematical propeller model was developed together with the aircraft dynamic equations to estimate the thrust, motor rotational speed (RPM), and load torque. Two different approaches were investigated to achieve this objective. The first approach, referred to as equation of motion (EOM) approach, relies on aircraft altitude, velocity, and orientation angles as primary inputs, from which the aerodynamic forces are determined. The second approach, referred to as motor power command (MPC) approach, uses the motor power as the main input, which represents the actual throttle behaviour of the aircraft. Along with this, the aircraft velocity and altitude are also provided to estimate the thrust, rotational speed, and torque.

In the EOM approach (also called aerodynamic equation-based approach), the model was able to predict the general aerodynamic behaviour of the propeller. However, it exhibited several oscillations in the estimated RPM and thrust due to rapid variations in the orientation angles and the coupled aerodynamic effects between the axes. This method also required lengthy computations, and in some regions of the flight, the predicted values did not align closely with the measured data.

In contrast, the MPC approach produced accurate and stable estimations of RPM, thrust, and torque, achieving more than 90% accuracy with respect to the actual flight measurements. It successfully

replicated the throttle response and aerodynamic performance. The inclusion of a propulsion efficiency factor of 0.75 further improved the results by compensating for transmission and aerodynamic losses.

The developed algorithm was tested using two different flight profiles, namely a normal flight mission and a touch-and-go mission. In both cases, the MPC approach produced consistent and realistic performance trends. The RPM plots with phase regions confirm that the algorithm is capable of correctly identifying different flight phases such as taxiing, take off, climb, cruising, descent, and landing based on variations in altitude, velocity, and power input.

Overall, the power command approach, which represents the actual situation in controlling a piloted aircraft, demonstrated higher accuracy, stability, and physical consistency compared to the aerodynamic equation-based method. The results from this model, specifically estimated torque, and rotational speed, will be used as inputs for the next stage of this study, which involves integration of the propeller model within the electric powertrain system. This integration will be discussed in the following chapter.

Chapter 4
Electric Powertrain Model

In this chapter, the model for the electric powertrain of the Pipistrel Velis Electro is developed and the battery behaviour across different parts of the flight is examined. The model represents two battery packs (one in the front and one at the rear) with terminals connected in parallel, an inverter, a permanent-magnet synchronous motor (PMSM), and a 3-blade, fixed-pitch propeller as the mechanical load, with direct connection to the shaft of the motor, with no gearbox. The motor is controlled based on the field-oriented control technique. Two modes of operation are considered for the aircraft in this study. In the autopilot mode, a predetermined flight mission is considered, and the motor is controlled based on the specified inputs of shaft speed reference and aerodynamic load torque. In the pilot-controlled mode, the pilot sets the desired power level by controlling the throttle position, and the controller generates the corresponding shaft speed reference. The gliding phase of the flight, representing the part of the mission where power is zero and the propeller is driven solely by airflow, is also included. Combining the motor-powered and gliding phases leads to a complete description of the propulsion behaviour over the full mission. The simulations are carried out in MATLAB Simulink environment.

4.1 Pipistrel Velis Electro Powertrain Configuration

In the following, different components of the powertrain are introduced.

4.1.1 Battery Packs

The two battery packs are identical in construction and electrical characteristics and form the high-voltage energy source of the aircraft. The battery pack part number is PB345V124E L, and each pack is built from Samsung INR18650 33G lithium-ion cells arranged in a 96S12P configuration (12 parallel branches, each composed of 96 series-connected cells). The battery pack specifications are provided in Table 4.1 [50].

In the powertrain model used in this study, each battery pack is modelled by an open-circuit voltage that is a function of SoC, a fixed series internal resistance of $R_{\text{int}} = 0.26\,\Omega$, which captures the instantaneous voltage drop due to internal losses, and two R-C branches that represent the dynamic polarization and diffusion effects of the battery, with values $R_1 = 0.2\,\Omega$, $C_1 = 250$ F, $R_2 = 0.05\,\Omega$,

and $C_2 = 100$ F. Note that the dependence of temperature has been neglected, assuming that the battery temperature is maintained within a narrow safe range. The relationship between the open circuit voltage and the state of charge is approximated by the fitted function given by (4.1) [51].

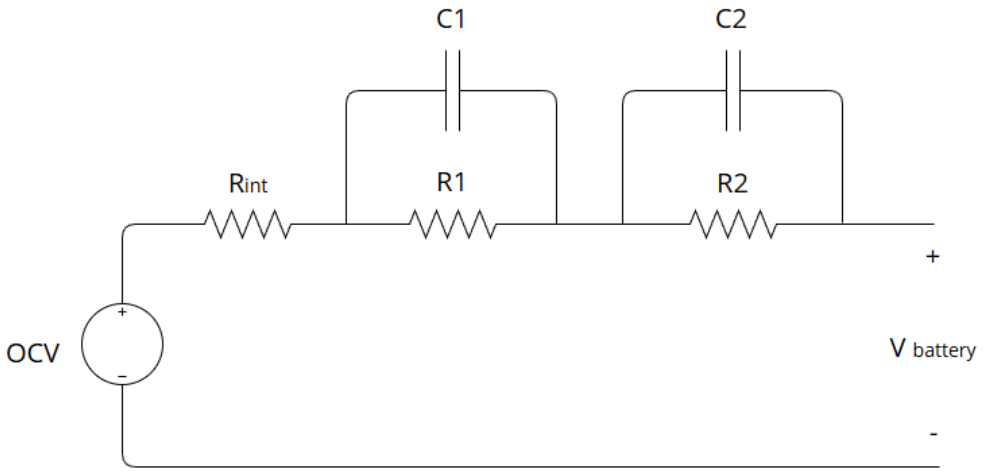
$$\mathrm{OCV(SoC)} = 3.2803e^{(0.1436\,\mathrm{SoC})} - 0.3136e^{(-15.3964\,\mathrm{SoC})} + 0.2167\,\mathrm{SoC}^2 \qquad (4.1)$$

Here, SoC denotes the state of charge on a normalised scale. This expression provides a smooth description of the open circuit voltage variations across the usable SoC range and is used to derive the equivalent circuit model in the simulation.

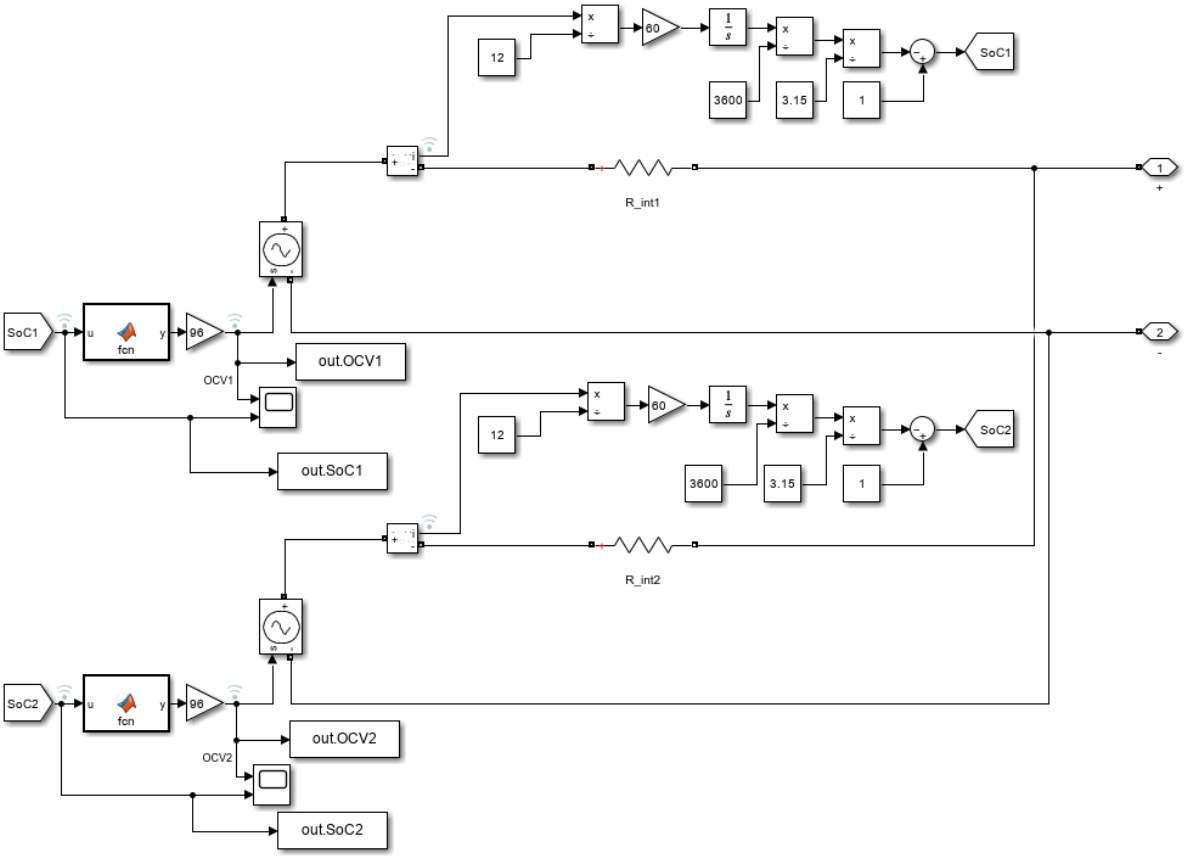
Table 4.1 Battery Pack Specifications [50]

Parameter	Value (per pack)
Battery designation	PB345V124E L
Cell type	Samsung INR18650 33G
Battery Pack configuration	96S12P
Minimum voltage	260 V
Nominal voltage	345 V
Maximum voltage	394 V
Maximum discharge current	120 A
Maximum continuous discharge power	40 kW
Maximum charging current	40 A
Rated capacity at 50 °C, 20 A	35 Ah, 12 kWh
Rated capacity at 23 °C, 20 A	33 Ah, 11 kWh
Rated capacity at 0 °C, 20 A	32 Ah, 10.5 kWh
Allowable discharge temperature range	0 °C to 58 °C
Allowable charge temperature range	0 °C to 45 °C
Allowable storage temperature range	0 °C to 30 °C

The equivalent circuit used for the battery pack model is given in Figure 4.1(a), and the corresponding Simulink block diagram is shown in Figure 4.1(b).



(a) Equivalent circuit diagram of battery pack model.



(b) Simulink block diagram.

Figure 4.1 Battery model.

Note: A scaling factor of 60 is introduced before the integrators in Figure 4.1 (b) to accelerate the battery discharge dynamics within the simulation. This allows one second of simulation time to represent one minute of real battery operation, enabling long-duration discharge behavior to be evaluated over a reduced simulation time.

4.1.2 Inverter

The propulsion system uses a three-phase inverter that converts the high voltage DC from the battery packs into three-phase AC voltages of variable magnitude and frequency required by the PMSM. The inverter is built up of insulated gate bipolar transistor (IGBT) switches that receive the pulse width modulated (PWM) gating signals generated by the motor controller. The inverter operates across the full battery voltage range of about 250 V to 400 V and delivers the phase currents required for different phases of flight. The switching frequency of inverter switches is set to 16 kHz, which provides a practical compromise among dynamic response, efficiency and thermal considerations.

4.1.3 State of Health (SoH) Evaluation

The battery state of health (SoH) is evaluated using a capacity fading model in which degradation is quantified with respect to the cumulative ampere-hours processed by the battery (Ah_{proc}), rather than by counting operating cycles [54]. The total processed charge is defined as:

$$Ah_{proc} = \frac{1}{3600}\int |ibat(t)|dt \tag{4.2}$$

where $i_{\text{bat}}(t)$ is the battery current.

The capacity fading is computed using a model that depends on battery temperature (T), average SoC, SoC deviation, and the processed ampere-hours (Ah_{proc}), and is given by (4.3):

$$\xi\left(T, SoC_{avg}, SoC_{dev}, Ah\right) = \sum_{i}\left(\left(k_{s1}\, SoC_{dev,i} \cdot e^{\left(k_{s2}\cdot SoC_{avg,i}\right)} + k_{s3}\, e^{\left(k_{s4}\cdot SoC_{dev,i}\right)}\right) \cdot e^{\left(-\frac{E_a}{R_{gas}}\left(\frac{1}{T_i}-\frac{1}{T_{ref}}\right)\right)}\right) \cdot Ah_i \tag{4.3}$$

where T_i is the battery temperature in kelvin, $E_a = 78{,}060\ \text{J/mol}$ the activation energy, $R = 8.314\ \text{J/(mol} \cdot \text{K)}$ the ideal gas constant, and $T_{\text{ref}} = 298\ \text{K}$ the reference temperature. The empirical constants are $k_{s1} = -4.092 \times 10^{-4}$, $k_{s2} = -2.167$, $k_{s3} = 1.408 \times 10^{-5}$, and $k_{s4} = 6.130$.

The average SoC over a charge-throughput interval $\Delta \mathrm{Ah}_m$ is defined as:

$$SoC_{avg} = \frac{1}{\Delta Ah_m} \int_{Ah_{m-1}}^{Ah_m} SoC(Ah) dAh \tag{4.4}$$

The SoC deviation and final SoH are computed through (4.5) and (4.6), respectively.

$$SoC_{dev} = \sqrt{\frac{3}{\Delta Ah_m} \int_{Ah_{m-1}}^{Ah_m} (SoC(Ah) - SoC_{avg})^2 dAh} \tag{4.5}$$

$$SoH_{final} = SoH_{initial} - \frac{\xi}{0.2Ah} \tag{4.6}$$

The summation index corresponds to the intervals where the temperature data changes. The SoH model accounts only for capacity fading due to cycling and does not include capacity loss during battery rest periods. The Simulink block diagram of the SoH model is shown in Figure 4.2.

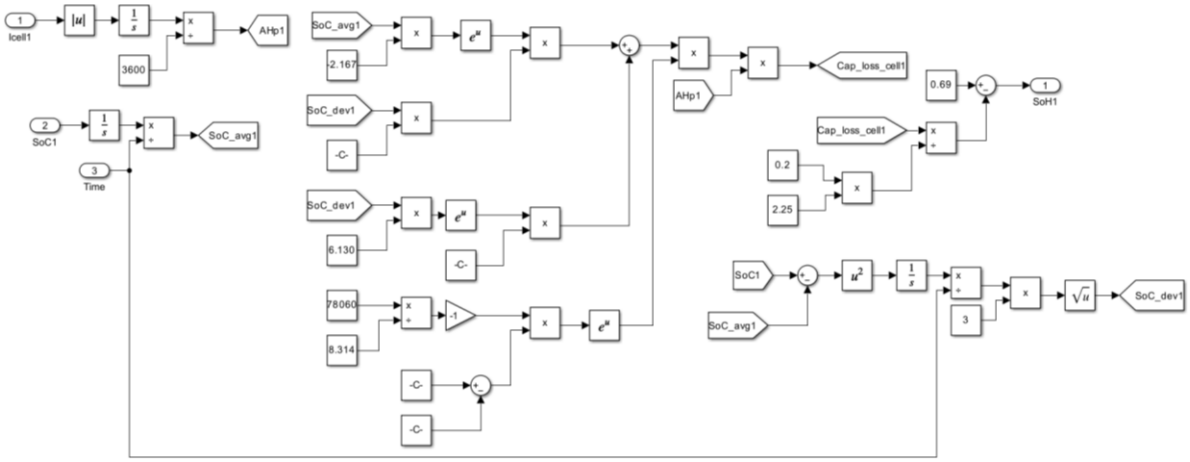


Figure 4.2 SoH model in Simulink.

4.1.4 Permanent Magnet Synchronous Motor (PMSM)

The electric drive in the aircraft is built around a permanent magnet synchronous motor (PMSM) from the EMRAX 268 MVLC series, referred to as the Pipistrel 268 MV LC VHML motor. The PMSM employed is an axial flux machine that is capable of producing high torque at low rotational speeds, which allows driving the fixed pitch propeller directly without any intermediate gearing. The main electrical and mechanical specifications of the PMSM, that are used in modelling, are given in Table 4.2.

Table 4.2 Velis Electro PMSM Specifications [50].

Parameter	Value
Motor designation	Pipistrel 268 MV LC VHML
Motor family	EMRAX 268 MVLC axial flux PMSM
Maximum take-off power	65 kW
Maximum continuous power	48 kW
Maximum speed	2500 RPM
Peak torque	220 N·m
Motor efficiency	89%
Motor mass	23 kg
Stator phase resistance ($\boldsymbol{R_{stator}}$)	0.004925 Ω
Inductances ($\boldsymbol{L_d} = \boldsymbol{L_q}$)	0.00014 H
Flux linkage ($\boldsymbol{\lambda_f}$)	0.06099 V·s
Rotor inertia ($\boldsymbol{J}$)	0.05769 kg·m^2
Pole pairs ($\boldsymbol{p}$)	10

The torque produced by a PMSM in the synchronously rotating reference frame is given by [52]

$$T_e = \frac{3}{2} p(\lambda_f i_q + (L_d - L_q) i_d i_q), \tag{4.7}$$

where p is the number of pole pairs, λ_f the flux linkage due to the rotor magnets, i_d and i_q the currents in the d and q axes, and L_d and L_q the corresponding inductances.

Since the model assumes $L_d = L_q$, the reluctance torque term vanishes, and the expression reduces to the much simpler form of

$$T_e = \frac{3}{2} p \lambda_f i_q \tag{4.8}$$

This relation is used in the simulation to compute the instantaneous electromagnetic torque produced by the machine. It shows that with equal d- and q-axis inductances, all torque comes from the q-axis current, which is consistent with a surface mounted permanent magnet machine. The block diagram of the inverter and PMSM in Simulink is shown in Figure 4.3.

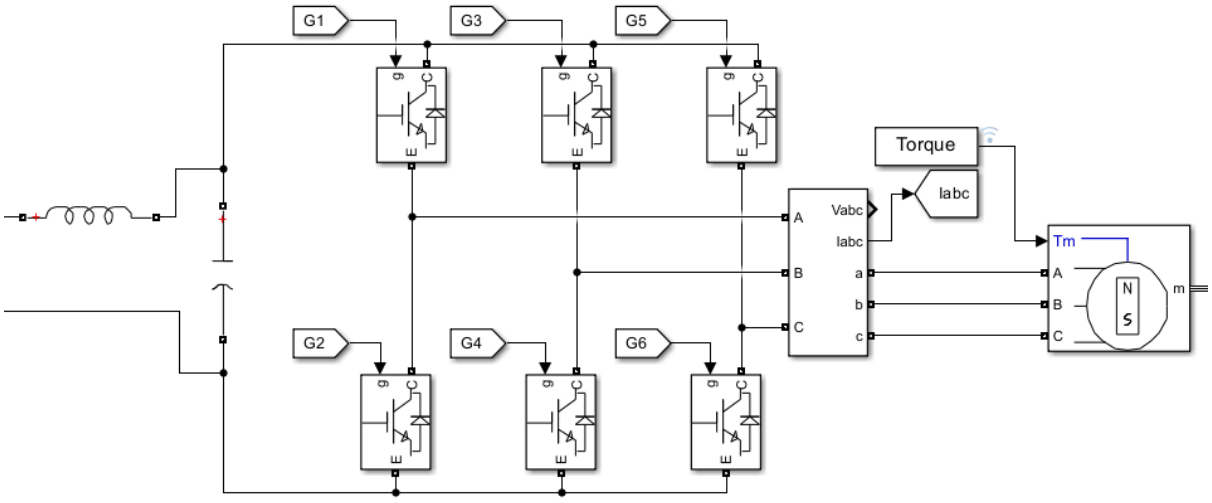


Figure 4.3 Inverter and PMSM Simulink model.

4.1.5 Field-Oriented Control

Field oriented control is used to control the PMSM in this study. The idea is to express the stator currents in a d-q reference frame that rotates synchronously with the rotor magnetic field. When the PMSM stator currents are represented in this frame, they appear as a direct-axis component and a quadrature-axis component, and the controller can adjust each of them independently. The q-axis current governs the torque, and the d-axis current influences the flux. For this motor, the d-axis current is kept at zero (due to the fact that it is a permanent magnet motor and the flux is independently produced by the permanent magnets on the rotor), and only the q-axis component is used to produce torque. The only time the d-axis current needs to be set to a non-zero value is when field weakening has to be implemented to allow motor speed to exceed the base speed. This can happen during take-off and climb, when a rather high power is commanded by the pilot asking for a motor speed higher than base speed. In such a case, a negative reference is set for the d-axis current.

The measured phase currents ($i_a, i_b,$ and i_c) are first transformed from *a-b-c* frame to the stationary α-β frame through Clarke transformation. This step is described by [53]

$$\begin{bmatrix} i_\alpha \\ i_\beta \end{bmatrix} = \frac{2}{3}\begin{bmatrix} 1 & -\frac{1}{2} & -\frac{1}{2} \\ 0 & \frac{\sqrt{3}}{2} & -\frac{\sqrt{3}}{2} \end{bmatrix}\begin{bmatrix} i_a \\ i_b \\ i_c \end{bmatrix} \tag{4.9}$$

The resulting components are then transformed to the synchronously rotating *d-q* frame using the Park transformation, given by

$$\begin{bmatrix} i_d \\ i_q \end{bmatrix} = \begin{bmatrix} \cos\theta_e & \sin\theta_e \\ -\sin\theta_e & \cos\theta_e \end{bmatrix} \begin{bmatrix} i_\alpha \\ i_\beta \end{bmatrix} \tag{4.10}$$

where θ_e is the electrical rotor position. This sequence allows the controller to access the torque and flux components of the current directly.

The inner current control loop regulates the d- and q-axis currents. The reference currents are generated by the current reference generator, and the current controller computes the corresponding voltage references required to force the actual currents to follow their commands. These voltage references are then transformed from the d–q frame back to the stationary frame using the *dq0*-to-*abc* transformation block. The space vector modulation (SVM) block uses these voltage commands to generate the inverter switching signals. The gating signals are applied to the inverter at a switching frequency of 16 kHz.

An outer speed control loop is implemented to regulate the motor speed. The speed controller generates the torque reference T_{ref} based on the difference between the commanded speed and the measured motor speed. This torque reference is then processed by the current reference generator to produce the reference q-axis current. In the autopilot mode, the speed reference is obtained directly from the specified flight condition. In the pilot-controlled mode, the commanded power is converted into an equivalent speed reference and supplied to the speed controller. The complete FOC structure ensures stable and accurate tracking of the demanded motor speed in both operating modes. The overall FOC architecture implemented in this work is illustrated in Figure 4.4. The individual Clarke (*a–b–c* to *α–β*) and Park (*α–β* to *d–q*) transformation stages are not shown explicitly in Figure 4.4. These coordinate transformations are implemented within the *abc*–to–*dq0* block and are therefore assumed as part of the internal signal processing.

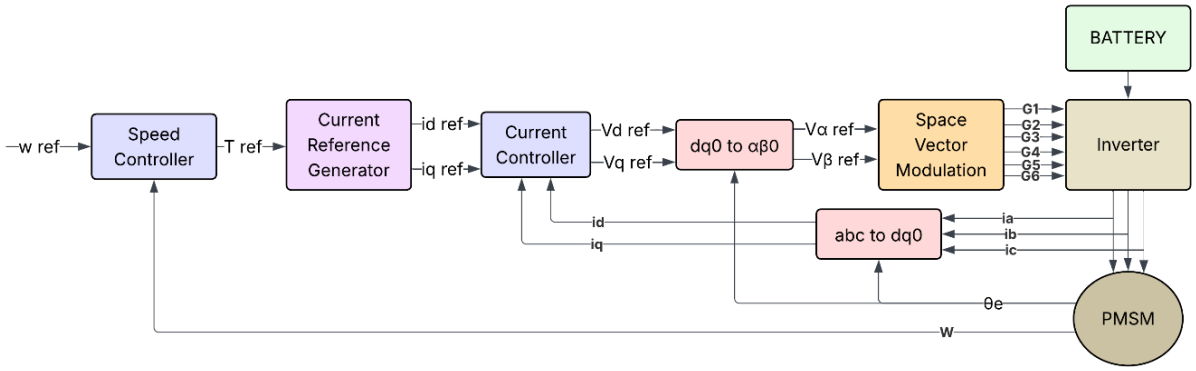


Figure 4.4 Field-oriented control architecture.

4.2 Methodology

This section describes the methodology used to study the electric powertrain's behaviour under two modes of operation, the autopilot flight mode and the pilot-controlled mode. Although both modes follow the same motor control structure, they differ in how the speed reference is supplied to the controller. The powertrain model operates in conjunction with the aerodynamic propeller formulations developed in Chapter 3. The profiles of the load torque acting on the motor shaft and the rotational speed are used as the external inputs to the powertrain model. An overall diagram of the powertrain, combined with the aerodynamic model, is shown in Figure 4.5.

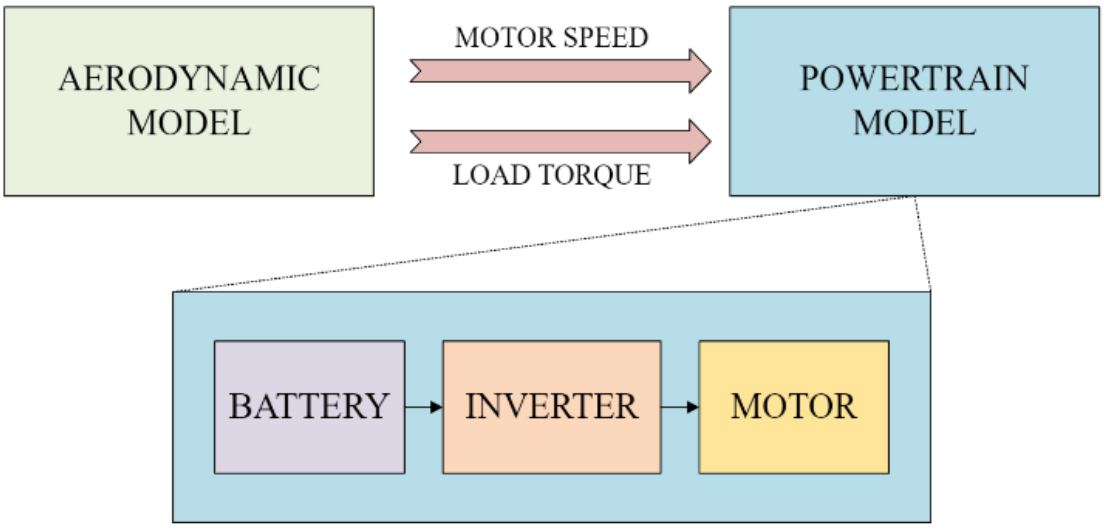


Figure 4.5 Powertrain model integrated with aerodynamic model.

4.2.1 Autopilot Flight Mode

In the autopilot flight mode, the flight behaviour is dictated by a prescribed profile rather than by pilot inputs. The motor speed reference and load torque follow directly from the aerodynamic model formulations introduced earlier, and together they represent the operating conditions at each point of the mission.

These predefined signals are supplied to the electric powertrain to examine how the system responds when the operating conditions are fully specified. This allows the behaviour of the motor, inverter and battery to be observed without the additional variability introduced by manual control. In particular, it enables study of the battery discharge characteristics, such as the state of charge and the open circuit voltage variations, in a controlled manner.

This mode is useful when assessing how the battery would perform for a specific flight mission before the mission is actually carried out. Once the references for motor speed and load torque are computed from the aerodynamic model, they are applied directly to the powertrain to predict how much energy the flight would require and how the battery parameters would evolve over the mission. This provides a practical way to evaluate the battery load and endurance for any planned flight profile. The Simulink model used for simulating this mode is shown in Figure 4.6. The controller parameters used for this mode are listed in Table 4.3.

Table 4.3 Controller Parameters in Autopilot Flight Mode.

Controller	Parameter	Value
Speed Loop	Proportional gain ($K_{p,\omega}$)	60
	Integral gain ($K_{i,\omega}$)	6
	Anti-windup gain ($K_{aw,\omega}$)	6/60
Current Loops (I_d and I_q)	Proportional gain ($K_{p,i}$)	60
	Integral gain ($K_{i,i}$)	15
	Anti-windup gain ($K_{aw,i}$)	15/60

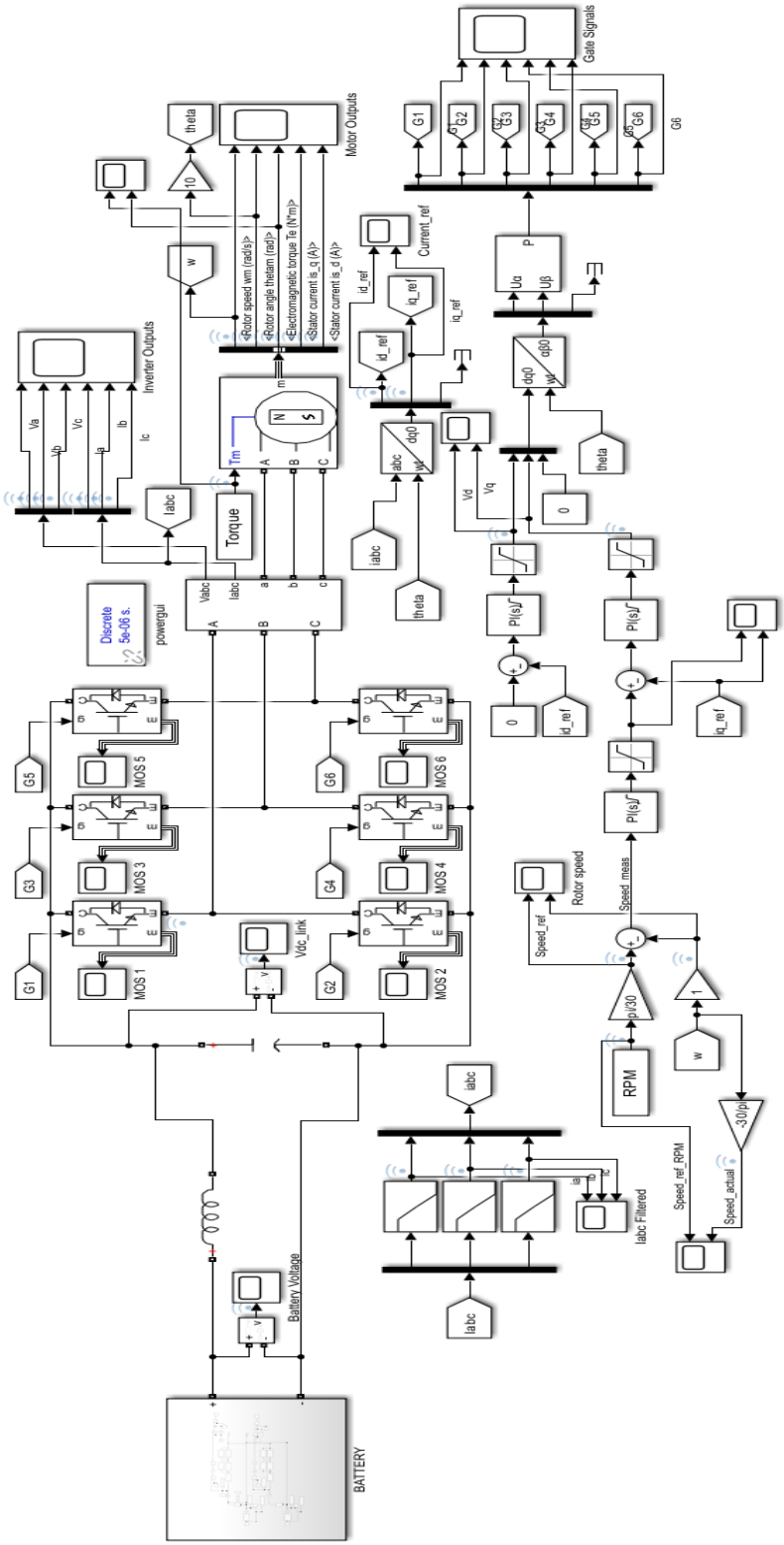


Figure 4.6 Autopilot Flight Mode Simulink Model.

4.2.2 Pilot-Controlled Mode

In the pilot-controlled mode, the simulation setup is the same as in the autopilot flight mode. The load torque follows the aerodynamic propeller formulations described previously, and all motor and controller parameters remain unchanged. The difference lies only in how the motor speed reference is obtained. Instead of obtaining the reference for the motor speed from the aerodynamic propeller formulations, the reference is generated from the pilot's power command extracted from the dataset.

The pilot command represents the electrical power requested by the pilot. This value is first converted to its equivalent mechanical power. The mechanical power is then divided by the load torque, giving the corresponding motor angular velocity. In this way, the pilot power command is converted into a speed reference that is supplied to the field-oriented control system.

A separate case arises during gliding. When the aircraft enters a glide, both the pilot power command and the load torque drop to zero. If the motor speed were computed directly from the mechanical power divided by torque, the result would be undefined. To address this issue, the simulation identifies the point at which the shaft power becomes zero. From this instant onward, the motor speed is no longer obtained from the power command. Since, presently, regeneration is disabled in Velis Electro aircraft, the inverter does not influence the motor during this phase, and the rotational speed is determined instead from the windmilling condition derived in Chapter 3. The windmilling formulation from subsection 3.2.1 is applied to compute the motor speed directly from the propeller aerodynamic coefficients.

Based on the above discussions, the pilot-controlled mode consists of two cases. When the power command is greater than zero, the speed reference is obtained from the mechanical power calculation and the field-oriented control operates normally. When the power command is zero, the motor speed is obtained from the windmilling relations. This approach allows the powered and gliding portions of the flight to be represented within a single simulation model.

In the actual aircraft, the pilot's throttle lever setting is translated into an analogue voltage signal (through a potentiometer), that is used as an input for the motor controller. Each position of the throttle corresponds to a specific voltage within a 0-5 V range. This voltage is internally scaled by the controller to produce a target speed command. Although the pilot sees only the power indication on the cockpit display, the underlying hardware simply reads a calibrated voltage that reflects the throttle position and converts it into the corresponding speed reference. Since the exact scaling used in the certified aircraft

is not available, the same approach cannot be replicated directly in this study. Instead, the pilot power command from the dataset is converted into a speed reference by following the basic mechanical relation between power and torque. This provides a consistent and physics-based way of constructing the speed reference from the available flight data, which is equivalent to what is done in the actual flight.

4.3 Simulation Results

To evaluate the performance of the Simulink powertrain model, the same flight mission is applied to both operating modes, that is, the autopilot mode and the pilot-controlled mode, so that their responses under identical conditions can be compared. The flight profile used in these simulations was previously introduced in Section 3.2.2 as the normal flight mission and is reused here as the input for the powertrain simulations. The results obtained from these simulations are presented in the following subsections.

4.3.1 Autopilot Flight Mode Simulation Results

Figure 4.7 compares the rotational speed reference generated from the aerodynamic propeller model (Speed_ref) with the simulated motor speed produced by the powertrain model (Speed_est) in the autopilot mode. The two curves show very close agreement across the full mission profile. A small delay is visible during the takeoff segment between approximately 11 and 13 minutes, where the commanded speed rises sharply, but the overall response still follows the reference well. Outside of this short interval, no noticeable mismatch is observed, and the simulated motor speed tracks the prescribed trajectory with high accuracy throughout the remainder of the mission.

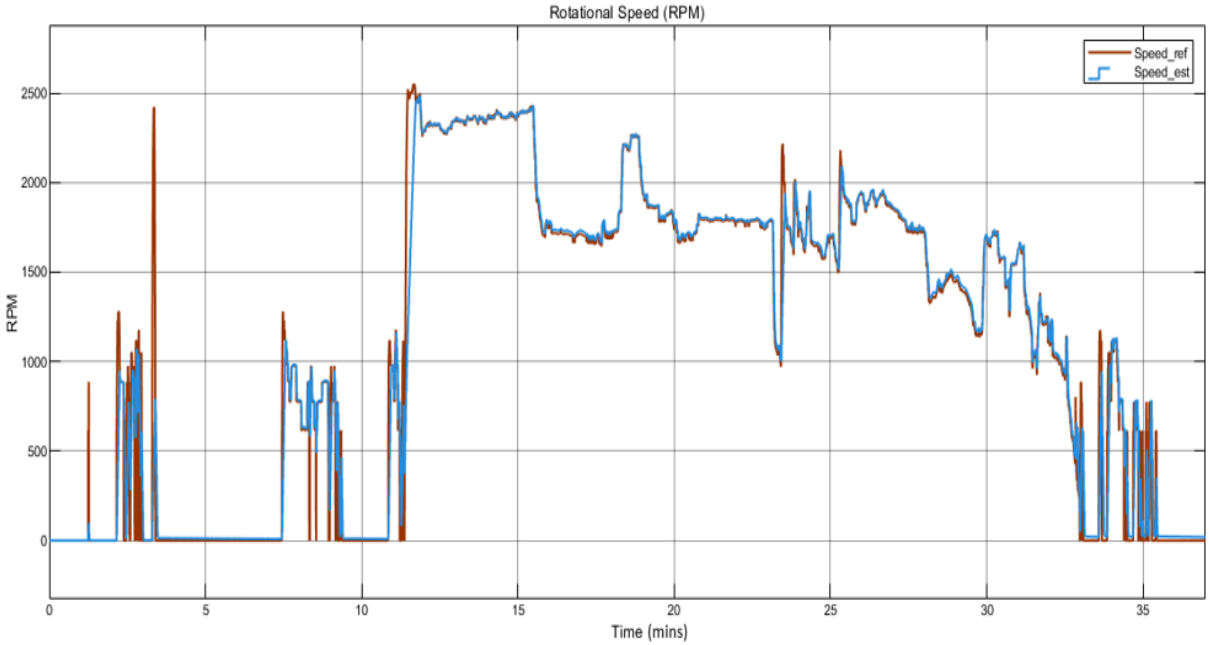


Figure 4.7 Reference and simulated (estimated) motor speed in rpm.

Figure 4.8 shows the profiles of the electromagnetic torque produced by the motor and the load torque. The electromagnetic torque follows the changes in the load torque with good agreement over the entire mission. The controller responds rapidly to the variations in the torque demand, and the overall trend of the simulated torque matches the aerodynamic load obtained from the propeller model. The main deviations appear as short-duration oscillations and sharp spikes that arise because the speed reference undergoes sudden transitions at several points in the mission (as observed in Figure 4.7), leading to rapid adjustments in the current command, leading to transient swings in the electromagnetic torque. Although these oscillations do not affect the general tracking performance, they indicate that the controller experiences fast current variations during rapid changes in operating conditions. Adjusting the current loop gains or smoothing the speed reference could reduce these spikes to some extent.

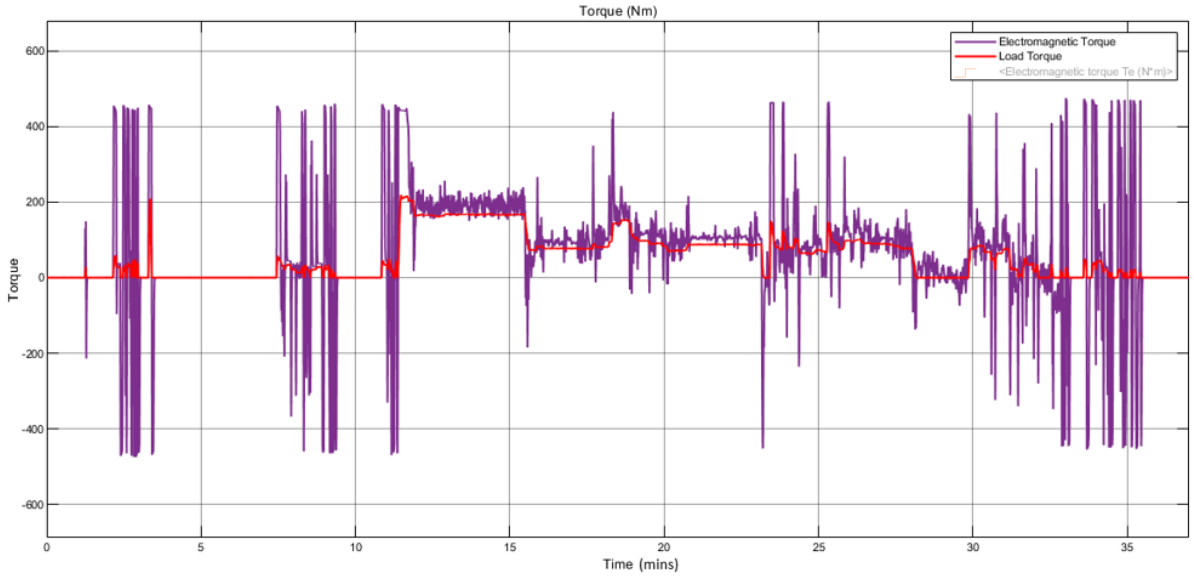


Figure 4.8 Electromagnetic torque and load torque.

The SoC and OCV profiles of the front and rear battery packs are shown in Figures 4.9 and 4.10, respectively. In these two figures, Actual SoC and Estimated SoC refer to the SoC values obtained from the flight data and simulation, respectively. The OCV shows the simulation results. The behaviours of the two packs are identical, as expected, since they are subjected to the same electrical loading throughout the mission. The overall discharge pattern reflects the power demand of the aircraft at each stage of the flight, and the SoC falls to below 60% by the end of the 36-minute mission, similar to the actual SoC data.

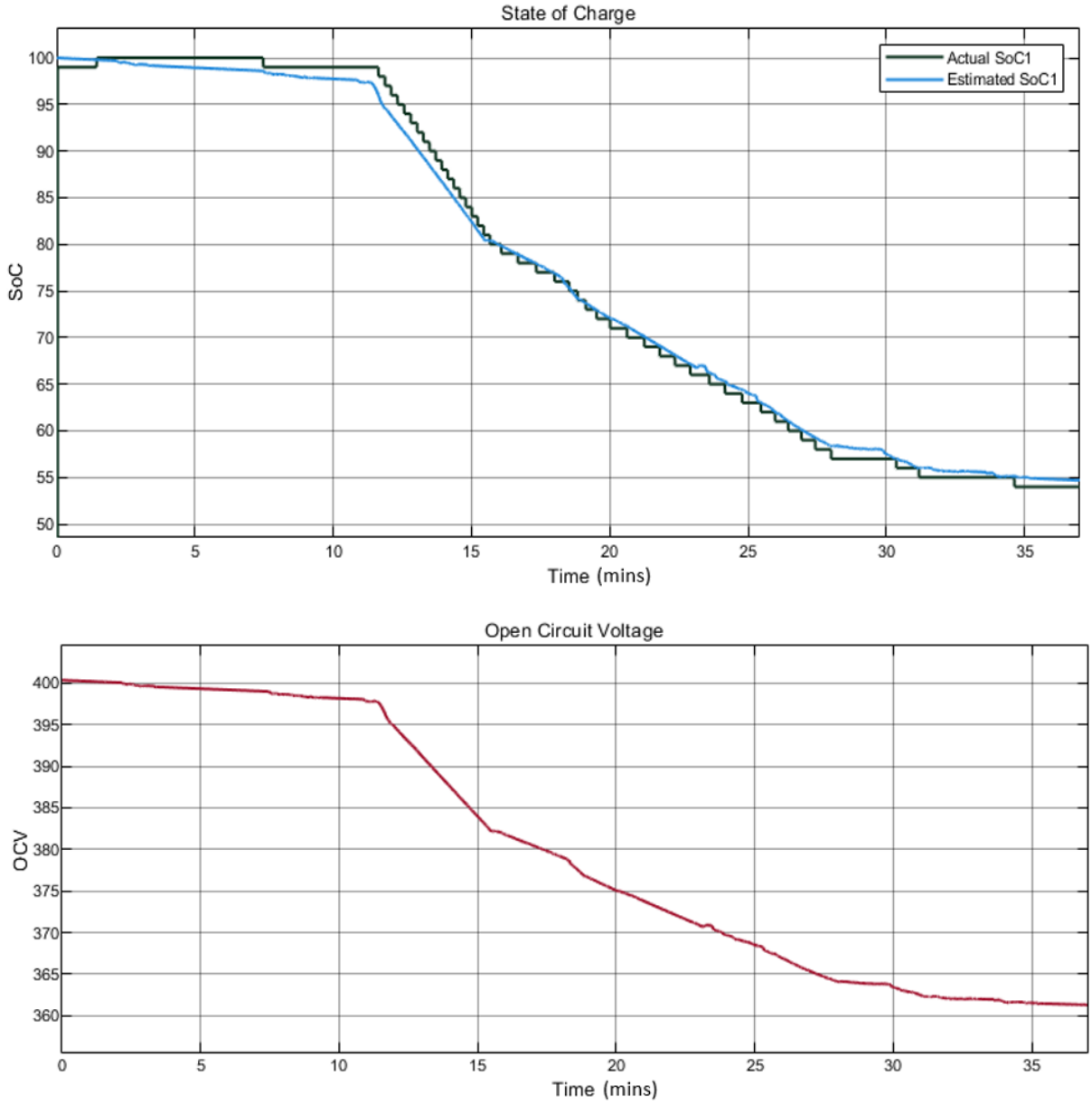


Figure 4.9 Front Battery Pack's SoC and OCV.

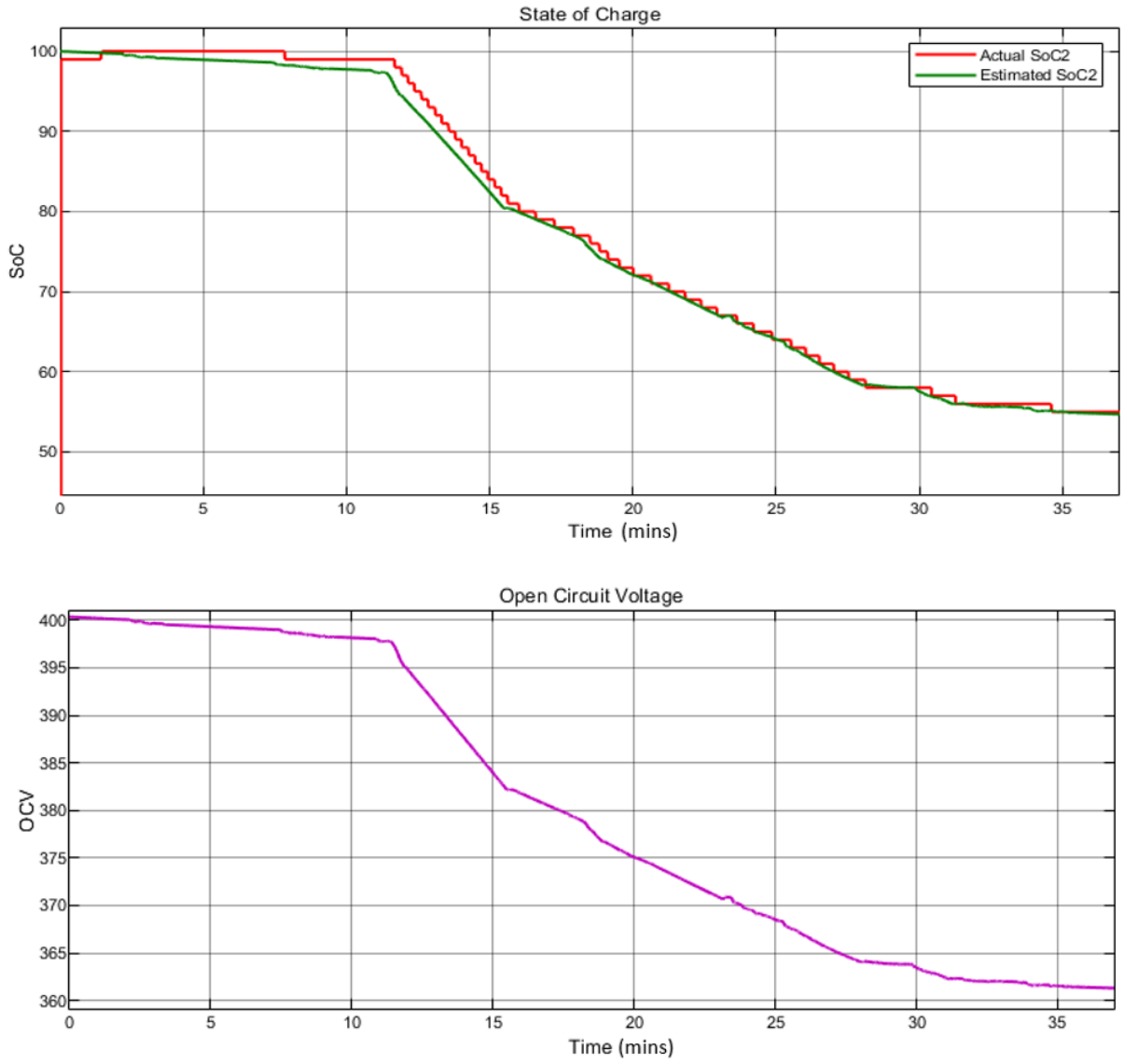


Figure 4.10 Rear Battery Pack's SoC and OCV.

At the start of the flight, during taxiing phase, when the aircraft is operating at very low power, the SoC decreases at very low rate. Once the aircraft transitions to take-off, beginning shortly after the 11-minute mark, the rate of discharge gets much larger. This region corresponds to the highest power requirement of the mission, and the rapid drop in SoC reflects the significant torque and speed demanded from the motor during take-off and the initial climb. The OCV follows the same trend, showing a noticeable reduction in this interval, consistent with the increased current draw.

During the subsequent cruising phase, the SoC decreases at a lower rate. The slope of the curve in this region is steady, indicating that the motor power is relatively stable and the electrical load is moderate. This behaviour aligns with the RPM profile of Figure 4.7, where the rotational speed settles to a nearly constant band after the take-off and climb manoeuvre. The corresponding OCV curve exhibits a gradual decline that mirrors the progressive depletion of the battery energy.

Later in the mission, between approximately 28 and 30 minutes, the aircraft enters a gliding segment. During this interval, the SoC curve flattens noticeably, showing that the battery is hardly being discharged. This behaviour arises because no electrical power is supplied during glide and the aircraft is sustained purely by aerodynamic forces. The OCV remains almost constant in this region as well, aside from the small variation associated with the open-circuit characteristics of the cells.

Overall, the SoC and OCV behaviours captured in the simulation are consistent with the expected performance of the Velis Electro batteries. The model clearly reflects the high-demand phase of take-off, the steady usage during cruising, and the negligible discharge during gliding. This confirms that the simulated discharge pattern matches the expected behaviour of the Velis Electro batteries across the different phases of flight.

Figure 4.11 shows the DC-link voltage variation across the mission. The slow downward trend reflects the reduction in the terminal voltages of battery packs as the SoC decreases, while the rapid spikes and dips are linked to sudden changes in motor demand, particularly during transitions in speed or torque. These short disturbances are expected when the inverter must adjust its switching instantaneously to follow changing references. Even with these fluctuations, the DC-link voltage remains well within a usable operating band, indicating that the inverter is able to respond to fast transients without losing regulation and stability in the supplied DC level.

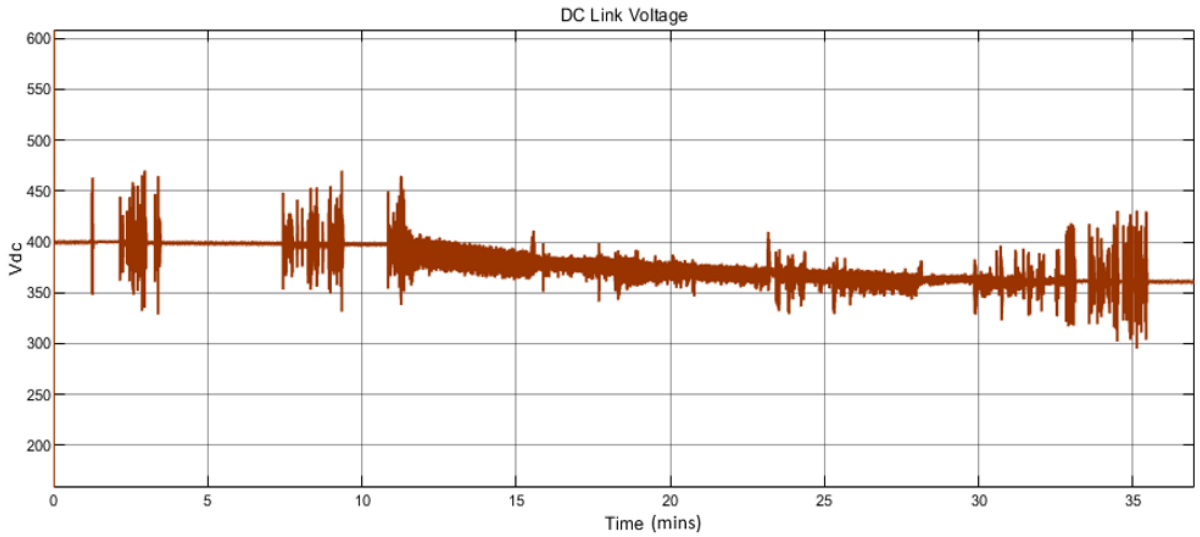


Figure 4.11 DC link voltage.

Figure 4.12 displays the d and q-axis components of the PMSM's stator current. The q-axis component experiences more significant variations because it is directly tied to torque production, rising sharply during take-off and settling to more moderate values during cruising phase. The d-axis current profile shows high-frequency ripples superimposed on a zero level, as expected for a surface-mounted PMSM where the goal is to keep flux-producing current near zero. If the motor speed is required to exceed the base speed of the PMSM during take-off/climb phase of the flight, enabling field weakening will become necessary. This is implemented by forcing the d-axis component of stator current to assume a negative value. The short spikes and uneven portions reflect the controller reacting to fast changes in operating conditions and the switching behaviour of the inverter. Overall, the current trajectories reflect the way the motor is being driven throughout the mission and how the current regulation adapts to the changing torque and speed demands imposed on the motor.

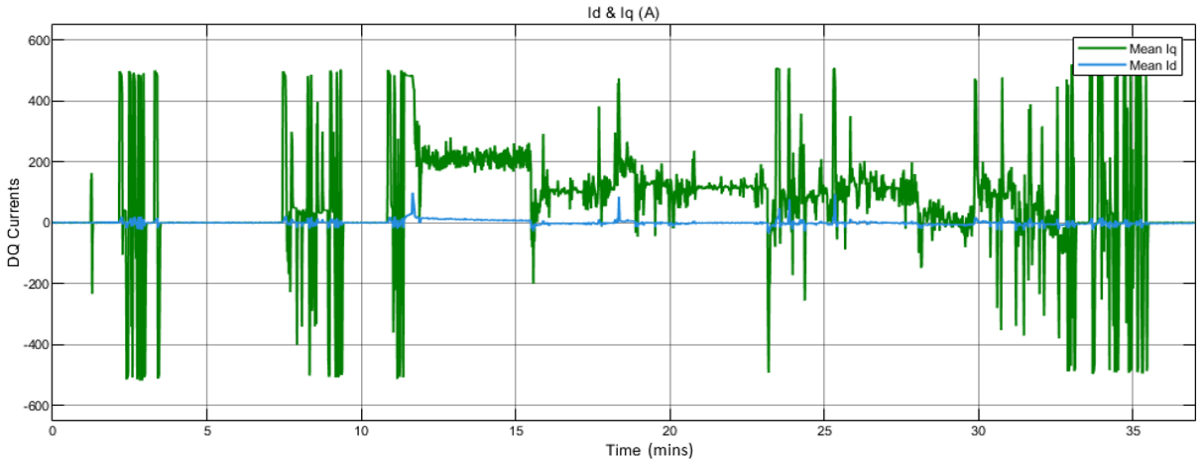


Figure 4.12 Stator currents (I_q and I_d).

Figure 4.13 provides an illustration of the phase currents and the corresponding phase-to-phase voltages of the inverter. The phase currents exhibit sinusoidal waveforms with proper phase separation, confirming that the FOC and SVM are regulating the motor currents correctly. The phase-to-phase voltages, on the other hand, display the high-frequency switching, which is characteristic of SVPWM, where the duty cycles of the pulses determine the effective voltage applied to each phase. The fundamental electrical frequency of the currents during this interval is approximately 400 Hz, while the inverter switching frequency is 16 kHz. This separation between the fundamental and switching frequencies is typical for high-performance motor drives and explains the presence of high-frequency ripple superimposed on the current waveforms. This combination of sinusoidal currents and high frequency switching voltages indicates that the inverter and controller are delivering the intended excitation to the motor during the take-off interval.

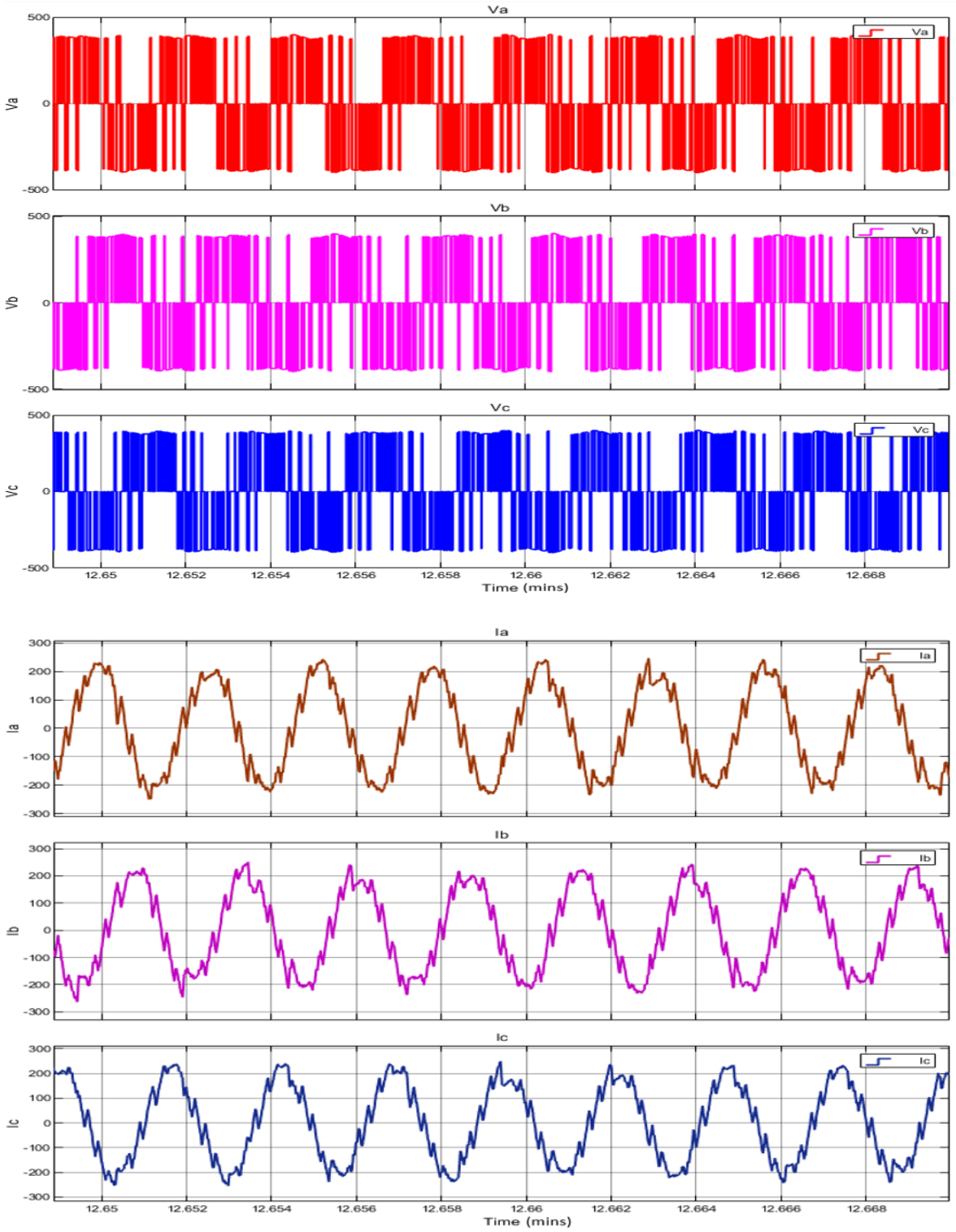


Figure 4.13 Inverter phase-to-phase voltages and currents.

As shown in Figure 4.14, the SoHs of both battery packs remain almost constant over the simulated time window. The estimated SoH closely tracks the actual SoH, and the difference between them remains negligible throughout the mission. This indicates that the capacity degradation accumulated during the simulated operation is minimal and that the SoH estimation is consistent.

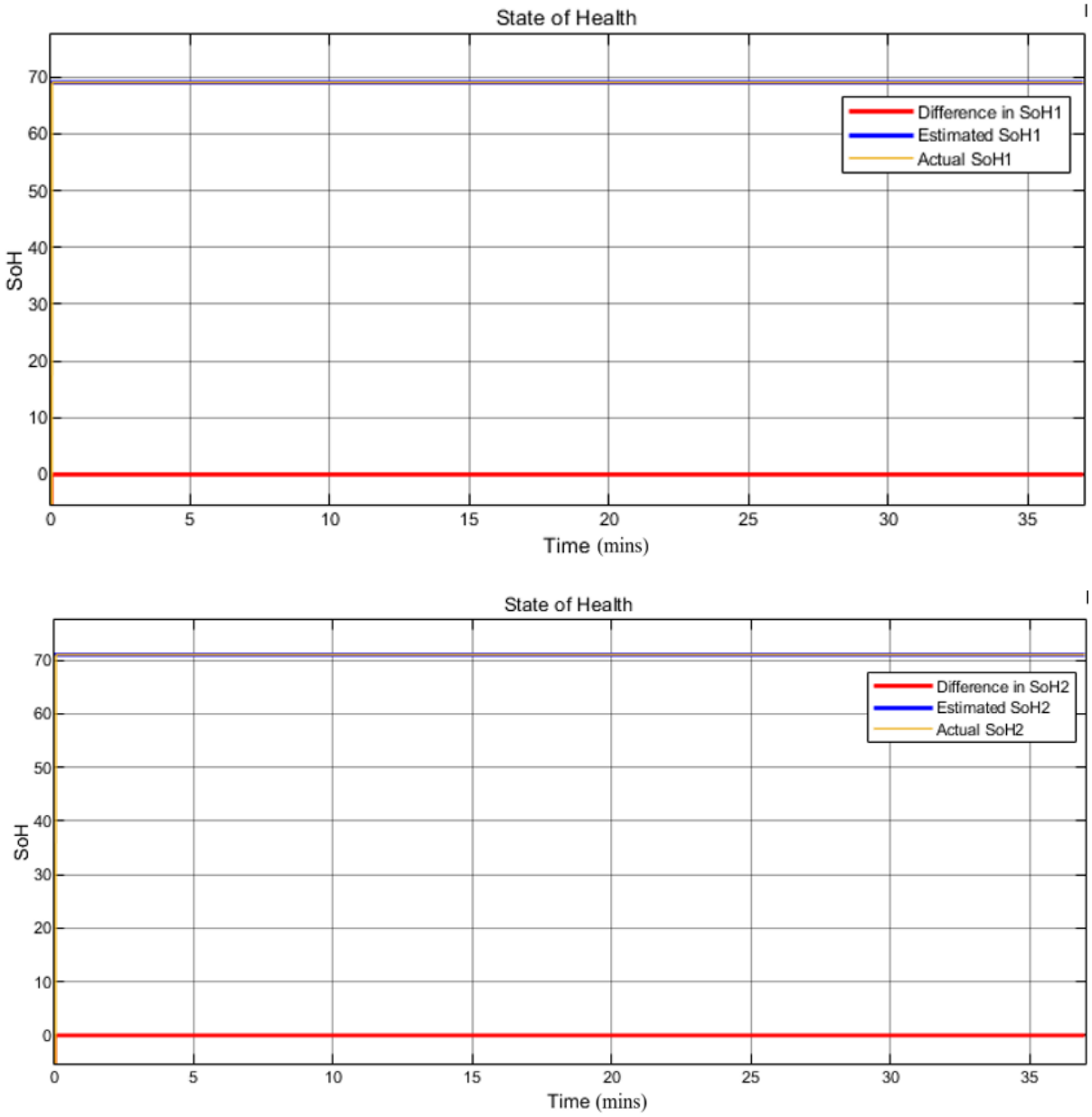


Figure 4.14 SoH of front and rear battery packs.

4.3.2 Pilot-Controlled Mode Simulation Results

Figure 4.13 shows the power commanded by the pilot in pilot-controlled mode over the mission. High power is commanded during takeoff and climb at around 11 to 15 minutes, followed by moderate and varying power levels during the cruise phase due to continuous manual throttle adjustments. Several intervals, especially between 22 to 25 minutes and 27 to 30 minutes, where the commanded power drops to zero, correspond to the glide segments.

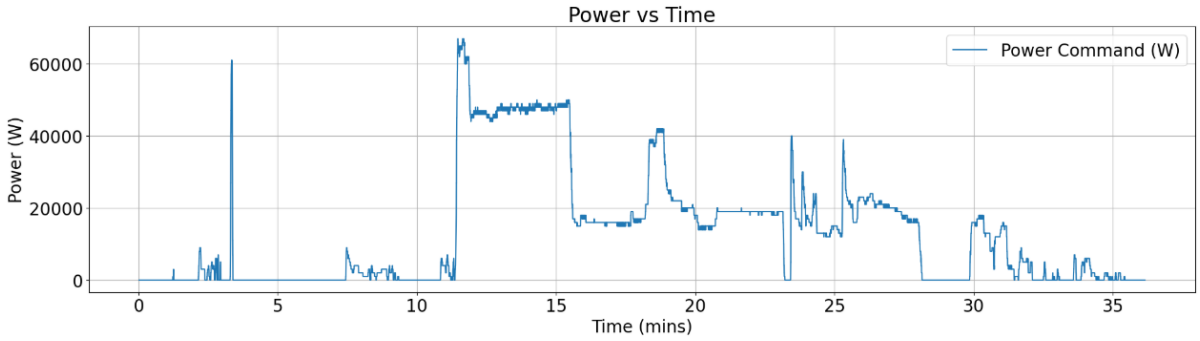


Figure 4.15 Power commanded by the pilot in W.

Figure 4.14 presents the rotational speed results for the pilot-controlled mode. Actual RPM represents the actual rotational speed of the aircraft propeller obtained from the flight data, and Estimated RPM represents the rotational speed obtained from the simulation. The simulation results and flight data are in close agreement throughout the mission, which shows that the controller is able to track the speed reference obtained from the aerodynamic propeller model with a high degree of accuracy. A few regions display noticeable deviations, particularly in the interval from about 11 to 12 minutes, again from 23 to 24 minutes, and from 29 to 30 minutes. These differences arise mainly from the controller settings at those points and can be reduced with additional tuning. Apart from these short segments, the match is consistent and the approach, which also includes the glide phase speed computation, is able to represent the behaviour of the actual aircraft. The accuracy of the tracking is above 90% across the full duration of the mission.

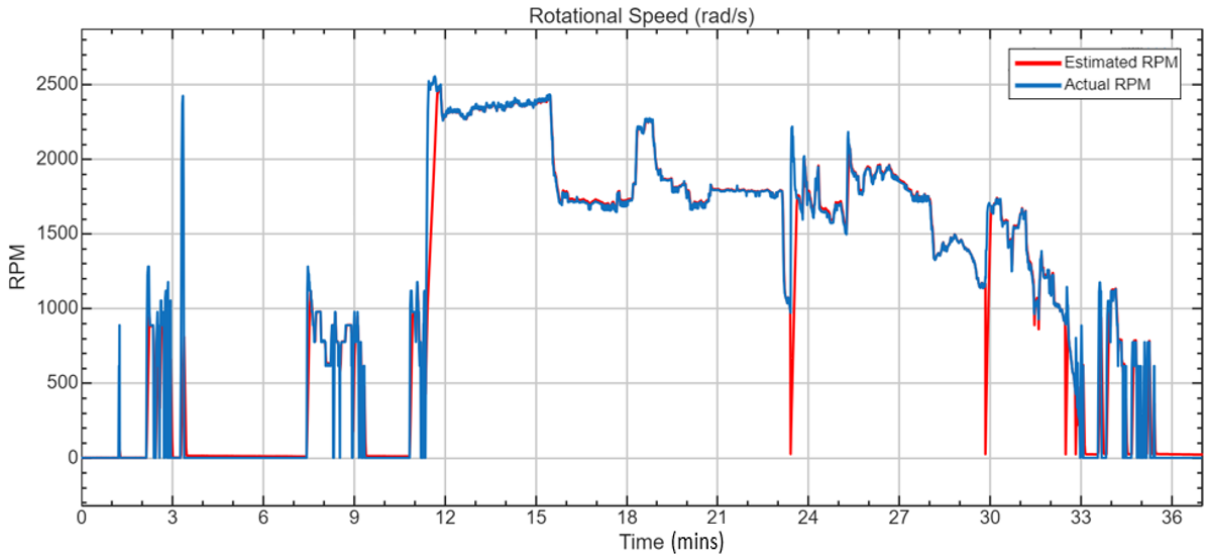


Figure 4.16 Actual and simulated (estimated) motor speed in rpm.

Figure 4.15 shows the load torque and the electromagnetic torque in the pilot-controlled mode. The load torque represents the torque that the propeller requires at each moment based on the flight conditions. The electromagnetic torque is the simulation results for the torque produced by the motor. For most of the mission, the electromagnetic torque follows the load torque closely, which shows that the motor is able to generate the torque needed to match the propeller demand.

There are some noticeable oscillations at certain points in the plot, especially during the early part of the mission and in a few short intervals later on. These come from the controller responding quickly to changes in the torque reference. With further tuning, these oscillations can be reduced. Apart from these short segments, the electromagnetic torque and the load torque reference stay well aligned, which confirms that the model is able to represent the torque behaviour accurately.

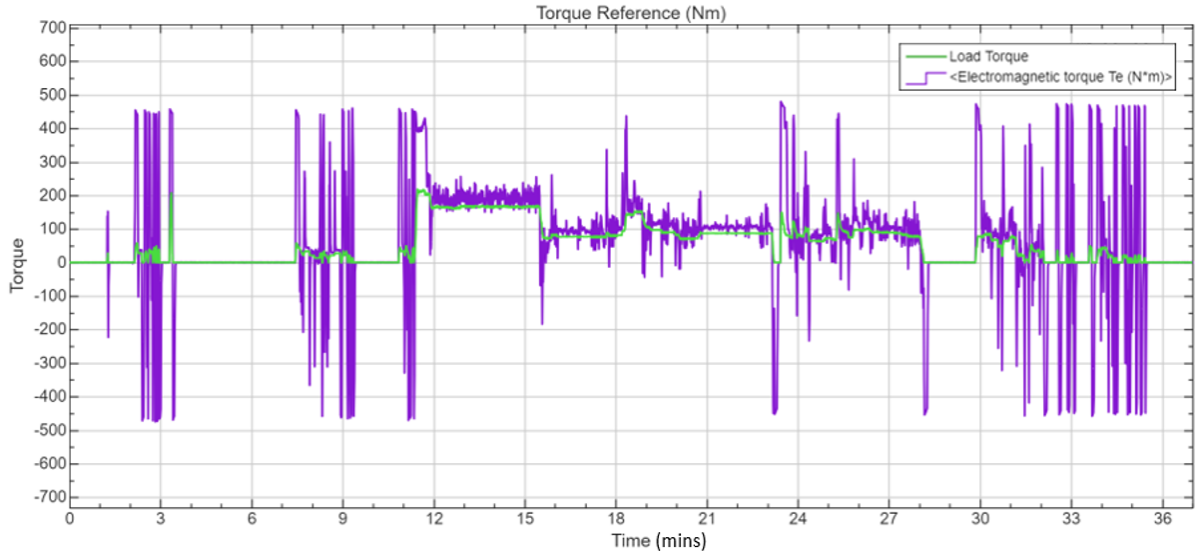


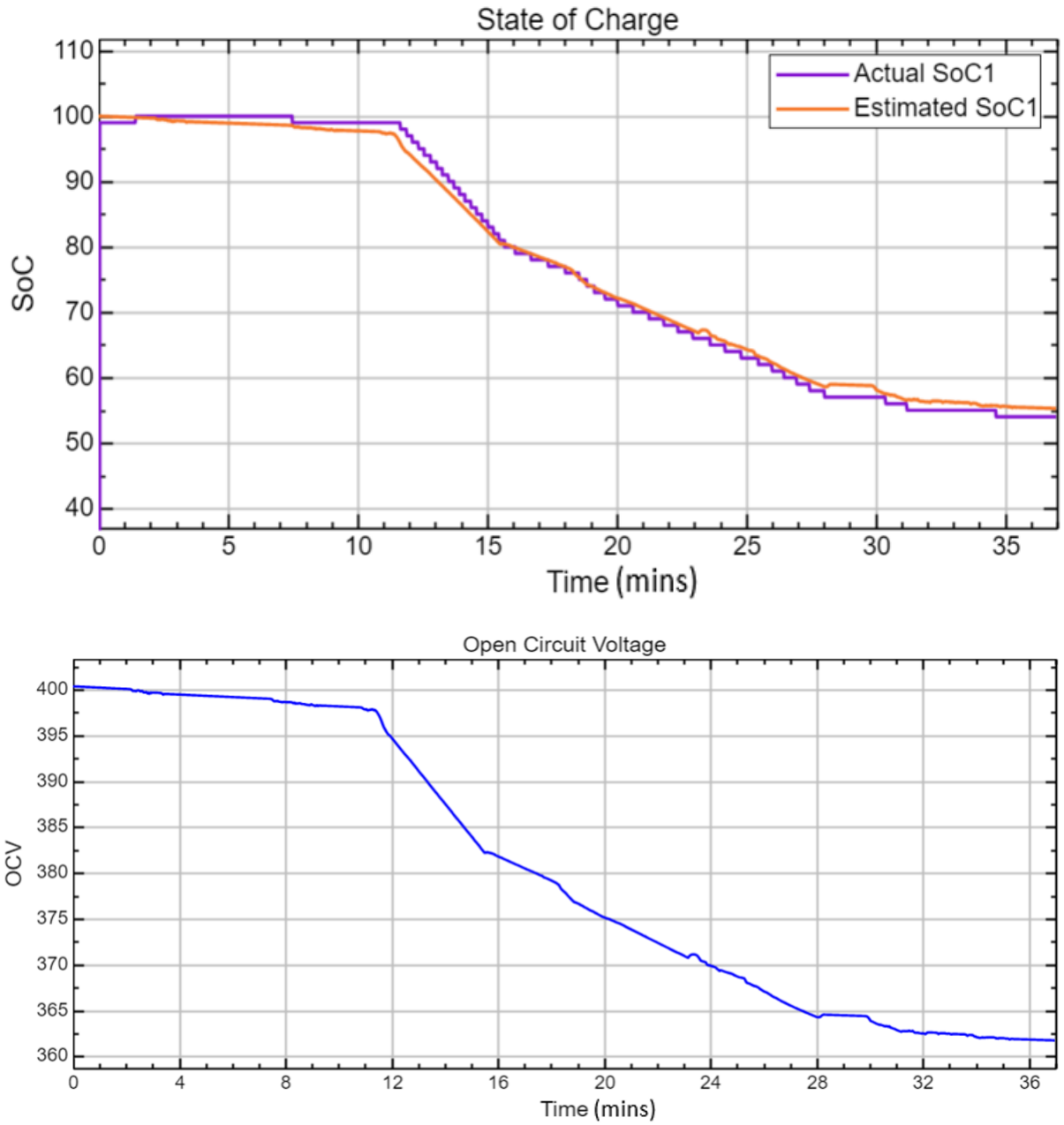
Figure 4.17 Electromagnetic torque and load torque.

Figure 4.16 compares the actual and estimated state of charge across the mission. The actual SoC is the state of charge recorded during the flight, and the estimated SoC is the SoC simulation results. The data and simulation results are in close agreement for almost the entire duration, which shows that the discharge predicted by the model is consistent with the measurements.

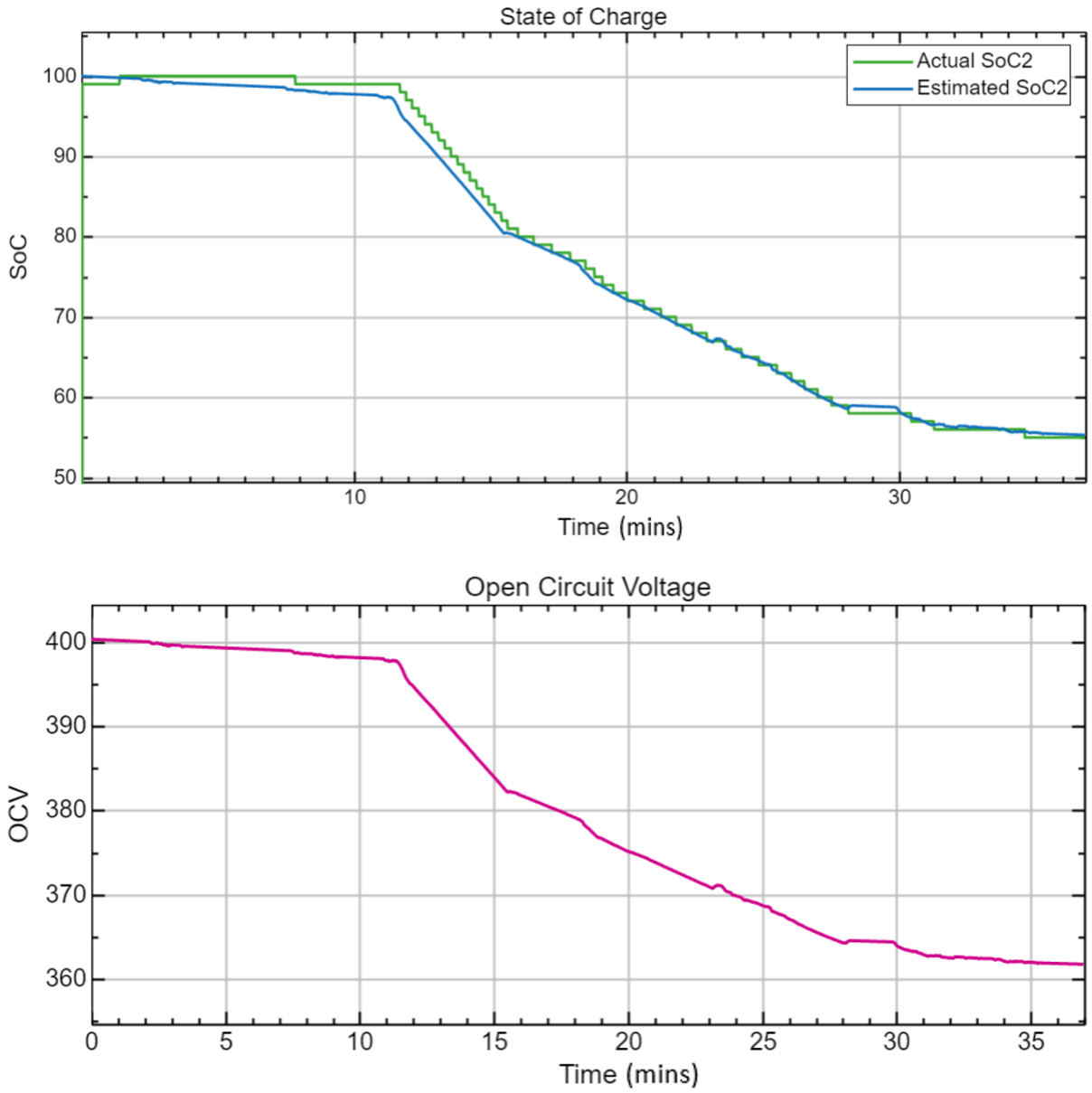
During the initial segment, the curves show moderate drop in SoC due to low power draw. As the aircraft enters the higher power region, both curves show sharp reduction in state of charge, and the estimated SoC follows the timing and slope of the measured SoC. In the later part of the mission, where the discharge rate becomes more gradual, the estimated curve continues to match the measured data trend, with only small differences.

The estimated state of charge remains in close agreement with the actual SoC even during the glide regions, where the discharge rate is lower and the powertrain operates differently from the powered segments. This shows that the estimation remains stable throughout both powered and glide portions of the mission.

The corresponding open circuit voltage follows the same overall decreasing trend as the state of charge across the mission. Higher voltage levels are observed during the initial high SoC region, while a steady voltage decline is seen as the battery discharges, with a more gradual variation during the later stages of the flight. This behavior is consistent with the expected OCV–SoC relationship of the battery.



(a) SoC and OCV of front battery pack.



(b) SoC and OCV of rear battery pack.

Figure 4.18 Actual and estimated SoC with OCV for both battery packs.

Figure 4.17 shows the variation of the DC link voltage (battery pack ensemble terminal voltage) during the mission. The voltage begins at a high value when the battery is fully charged and decreases steadily as the flight progresses. Small fluctuations appear at certain points due to changes in power demand, but the overall trend is smooth.

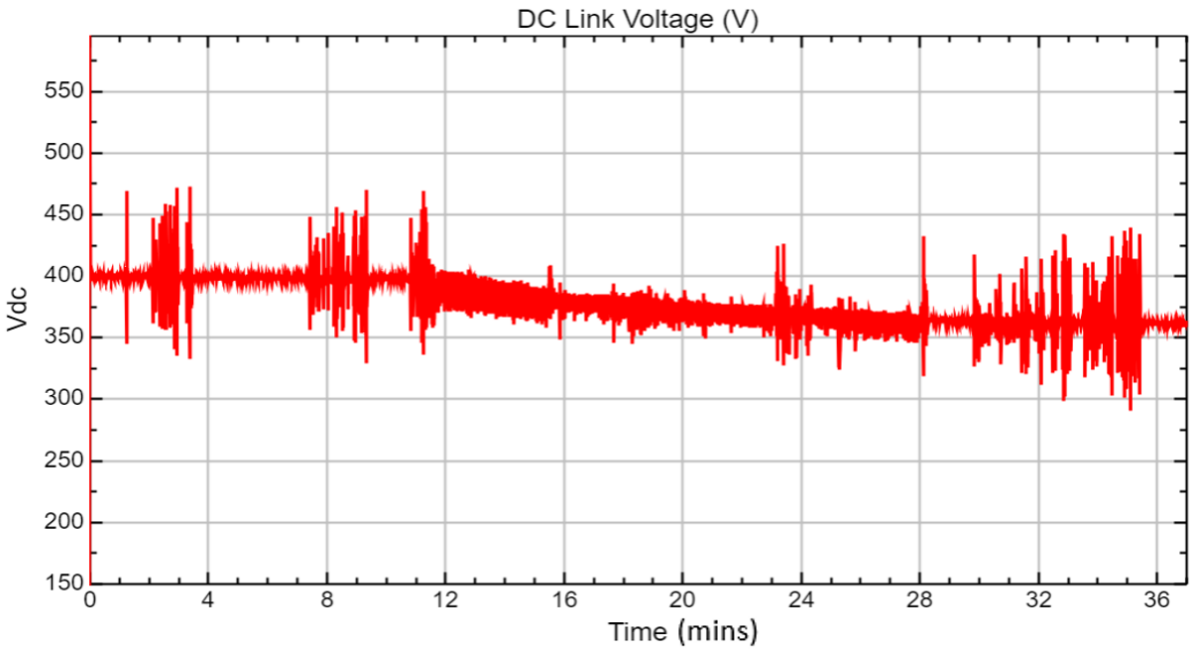


Figure 4.19 DC Link Voltage in pilot-controlled mode.

Figure 4.18 shows the three-phase inverter phase-to-phase voltages and the corresponding phase currents. The phase-to-phase voltages exhibit the expected switching pattern produced by space vector modulation, with the duty ratio variations creating the required fundamental components. The phase currents follow the general sinusoidal shape but contain visible ripple and small high frequency distortions. These fluctuations come from the switching action of the inverter and the fact that the currents are displayed without any filtering. Even with the ripples present, the three-phase currents maintain the correct relative phase and amplitude, confirming that the inverter and the modulation strategy operate as intended for the motor drive.

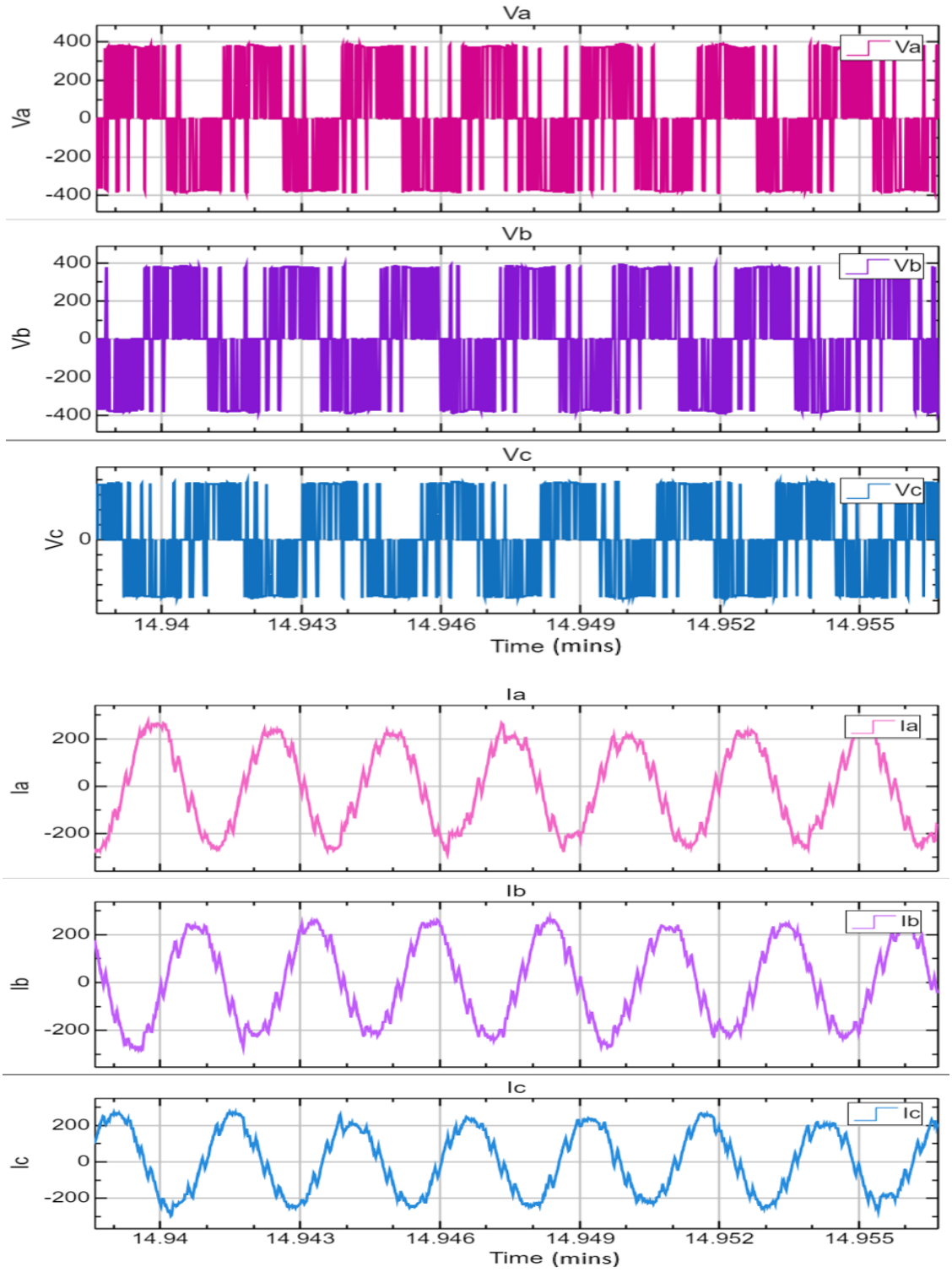


Figure 4.20 Inverter phase-to-phase voltages and currents in pilot-controlled mode.

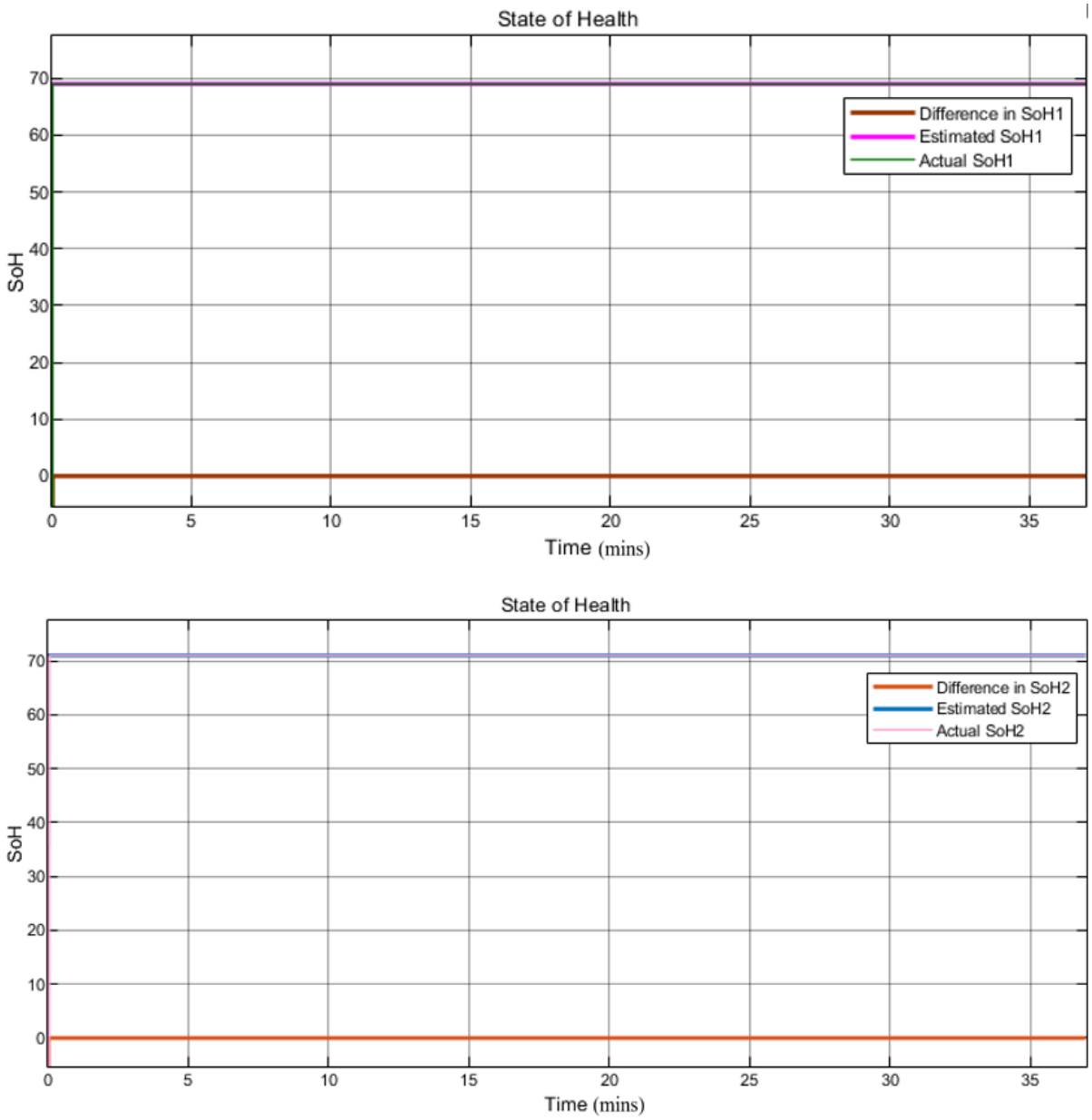


Figure 4.21 SoH of front and rear battery packs in pilot-controlled mode.

Figure 4.21 shows that the battery SoH remains effectively unchanged during pilot-controlled operation. The SoH trajectory exhibits no observable deviation from its initial value over the mission, indicating that the operating conditions in this mode do not result in measurable capacity loss within the simulated duration.

4.3.3 Pilot-Controlled Mode Simulation Results for an Additional Flight Mission

The following flight profile is like the nominal flight mission introduced in section 3.1.4. The electric powertrain model is simulated using this profile for additional model validation. Figures (4.22–4.24) present the aircraft altitude, IAS and TAS, and power command, respectively.

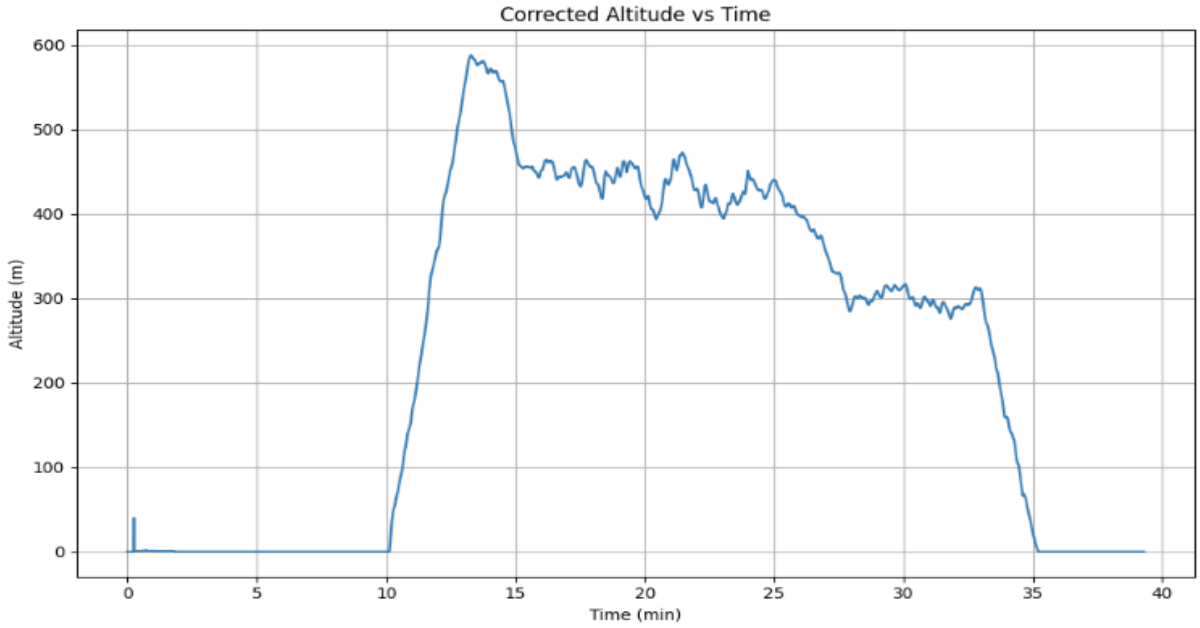


Figure 4.22 Aircraft altitude.

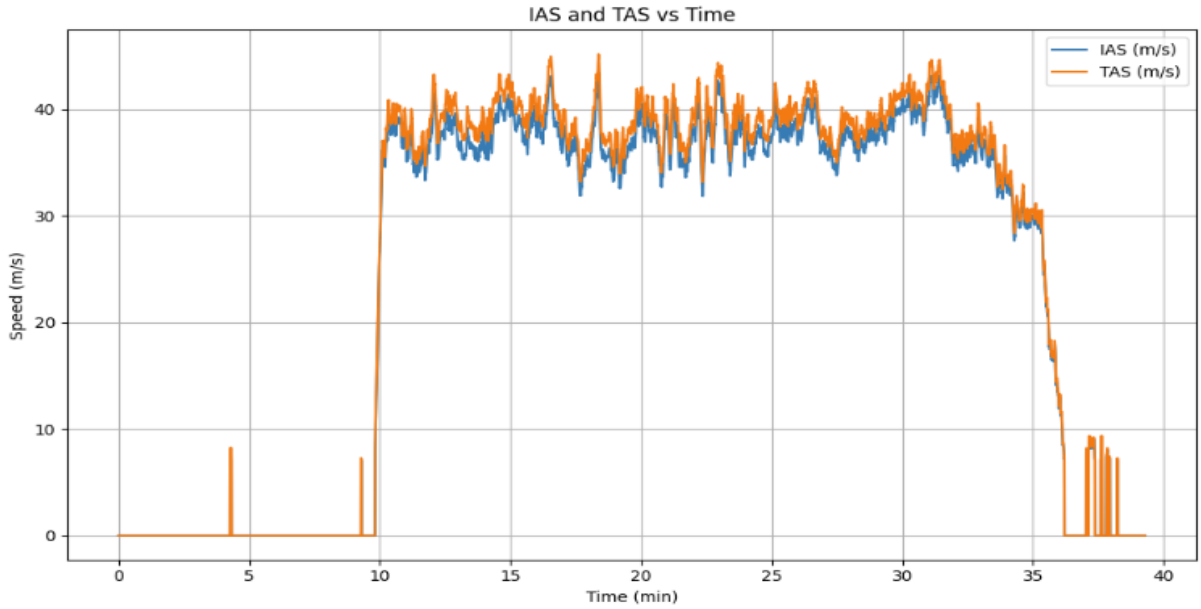


Figure 4.23 Aircraft indicated air speed and true air speed.

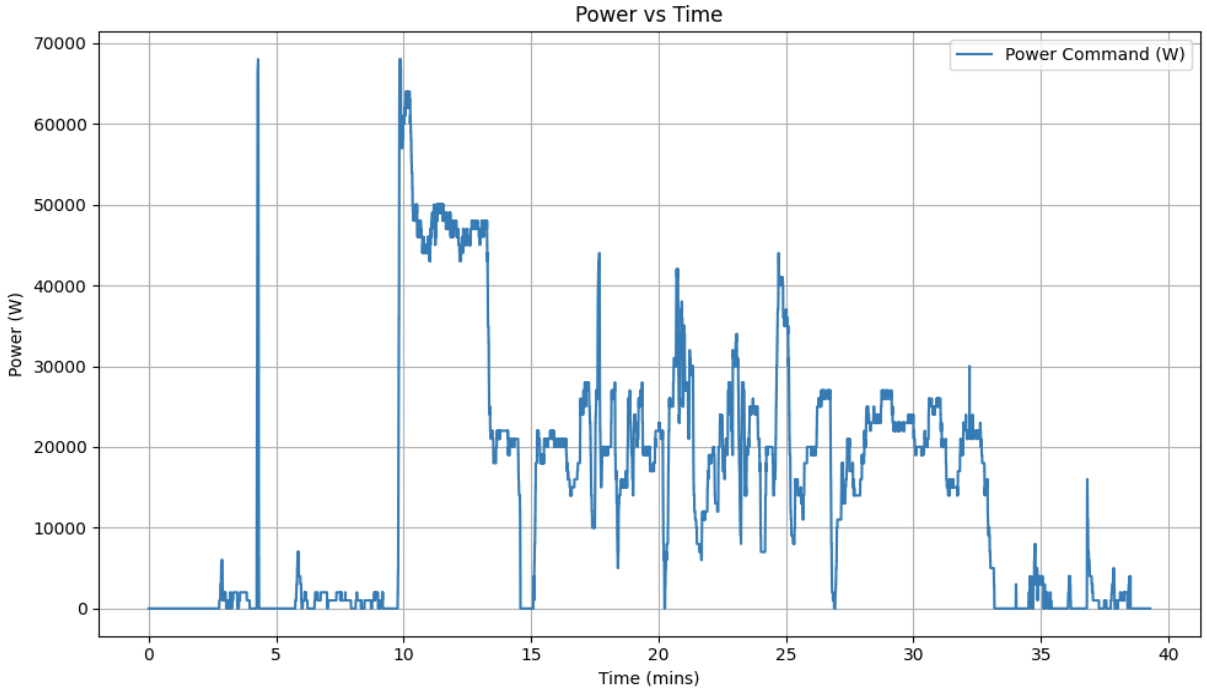


Figure 4.24 Power commanded by the pilot.

Figures (4.25-4.31) illustrate the results obtained for the additional flight mission in the pilot-controlled mode.

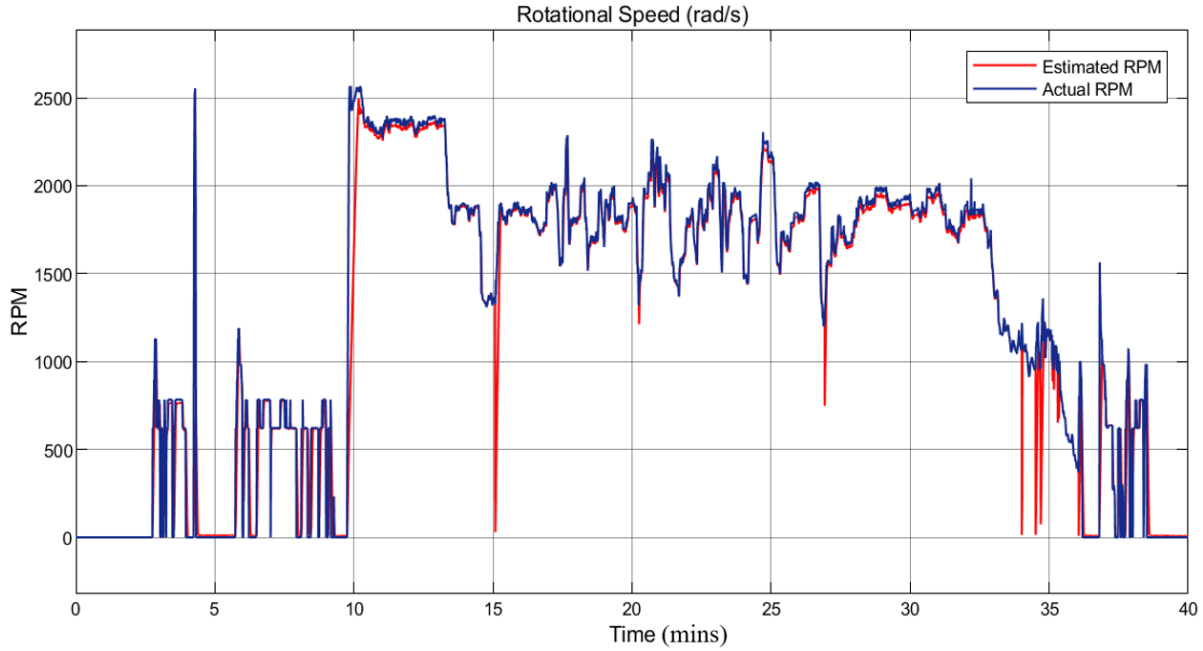


Figure 4.25 Estimated and actual RPM for the additional flight mission.

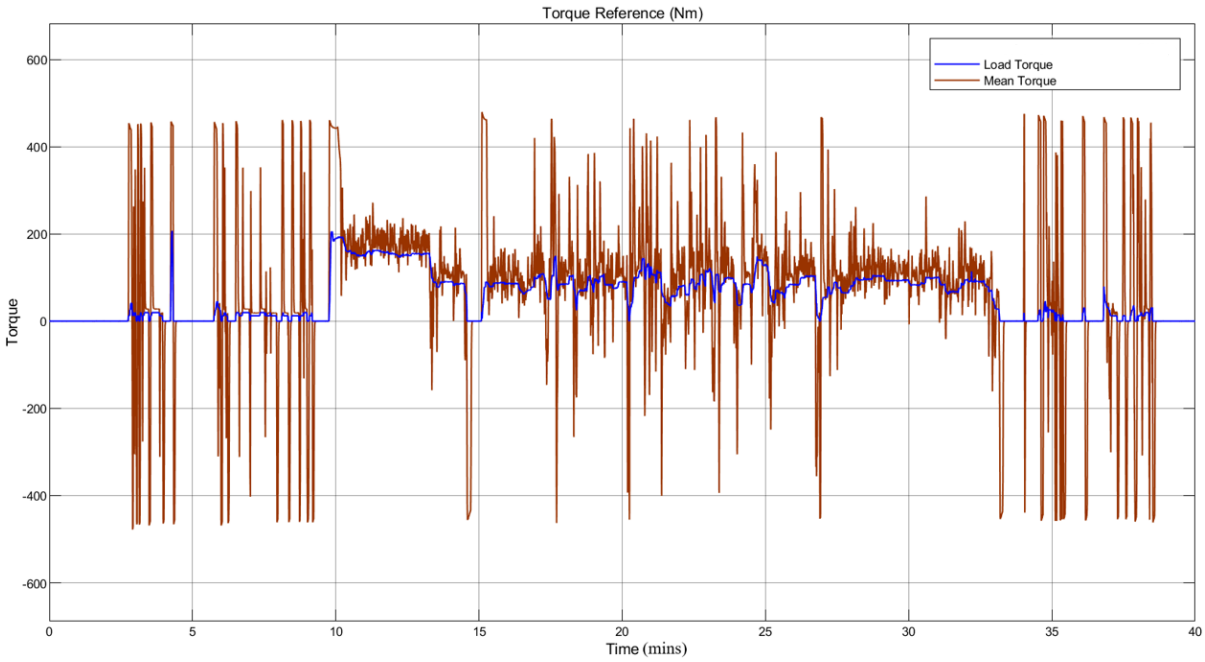


Figure 4.26 Actual load torque and mean electromagnetic torque for the additional flight mission.

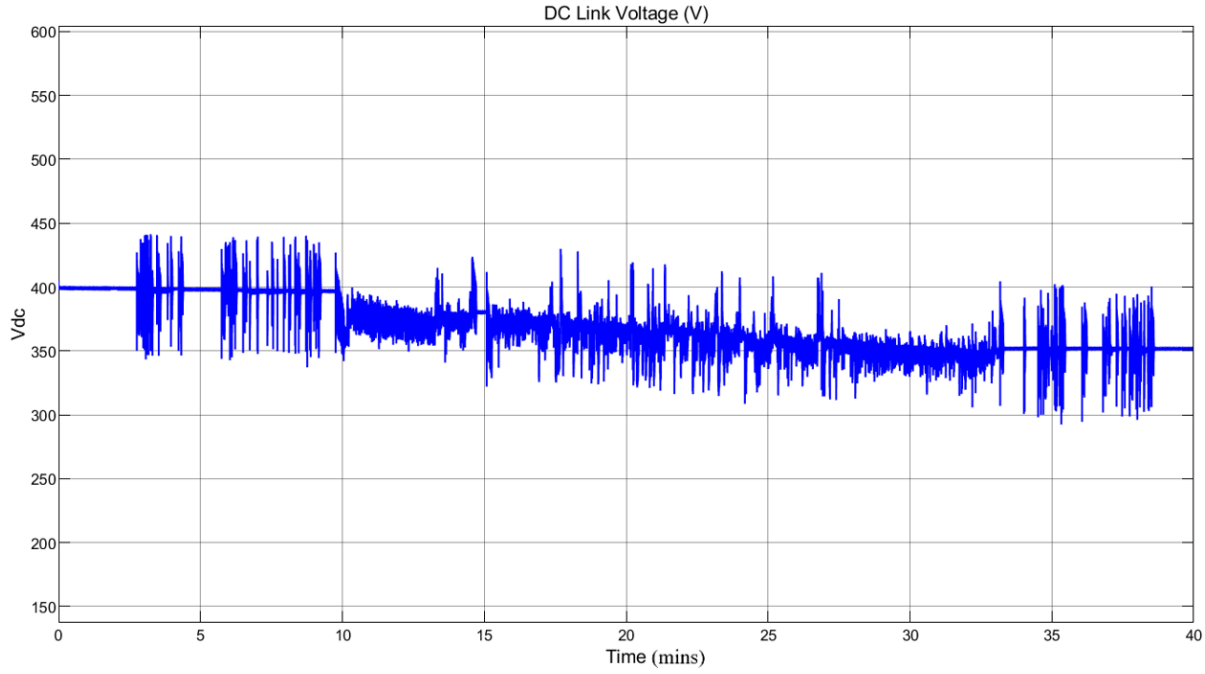


Figure 4.27 DC link voltage for the additional flight mission.

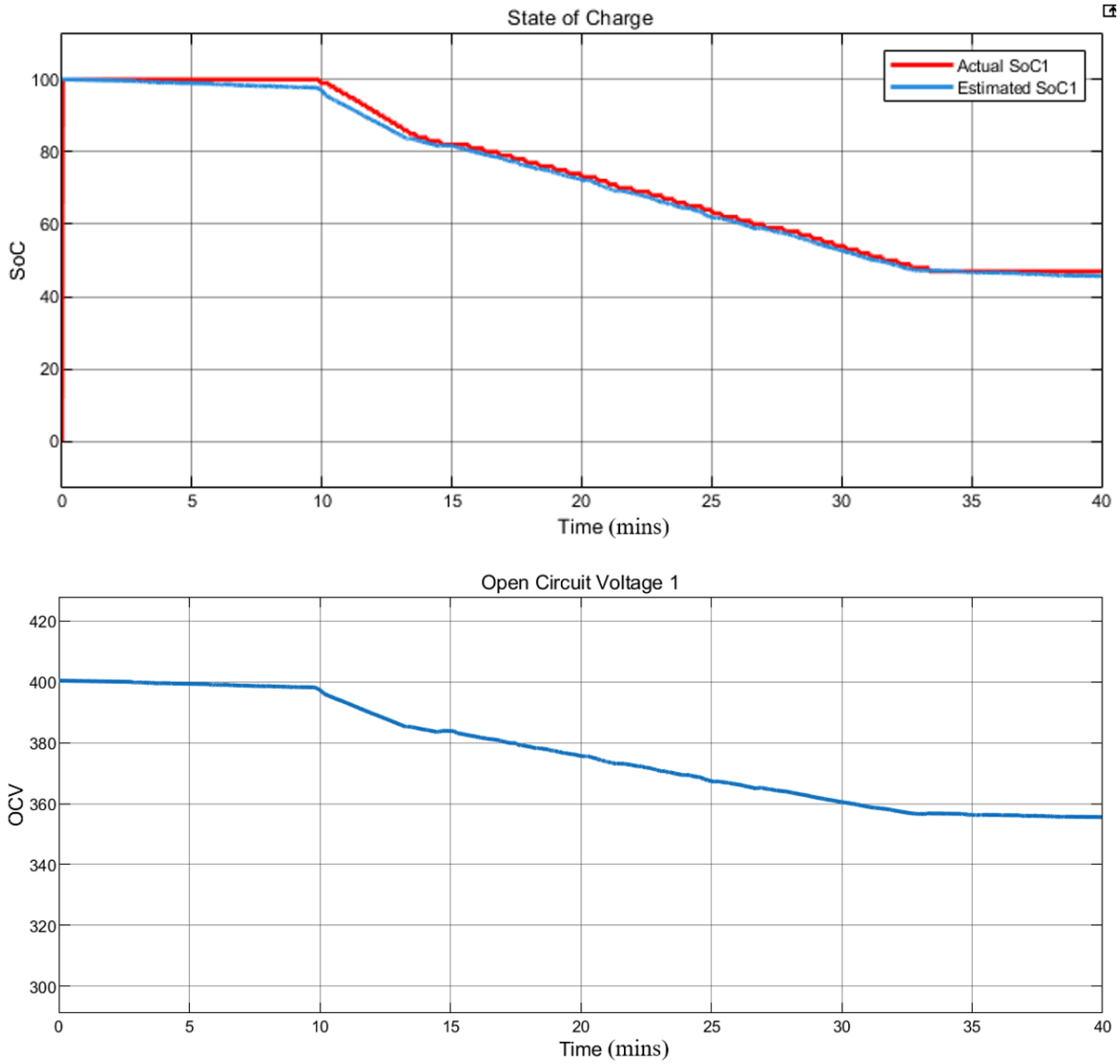


Figure 4.28 SoC and OCV of the front battery pack for the additional flight mission.

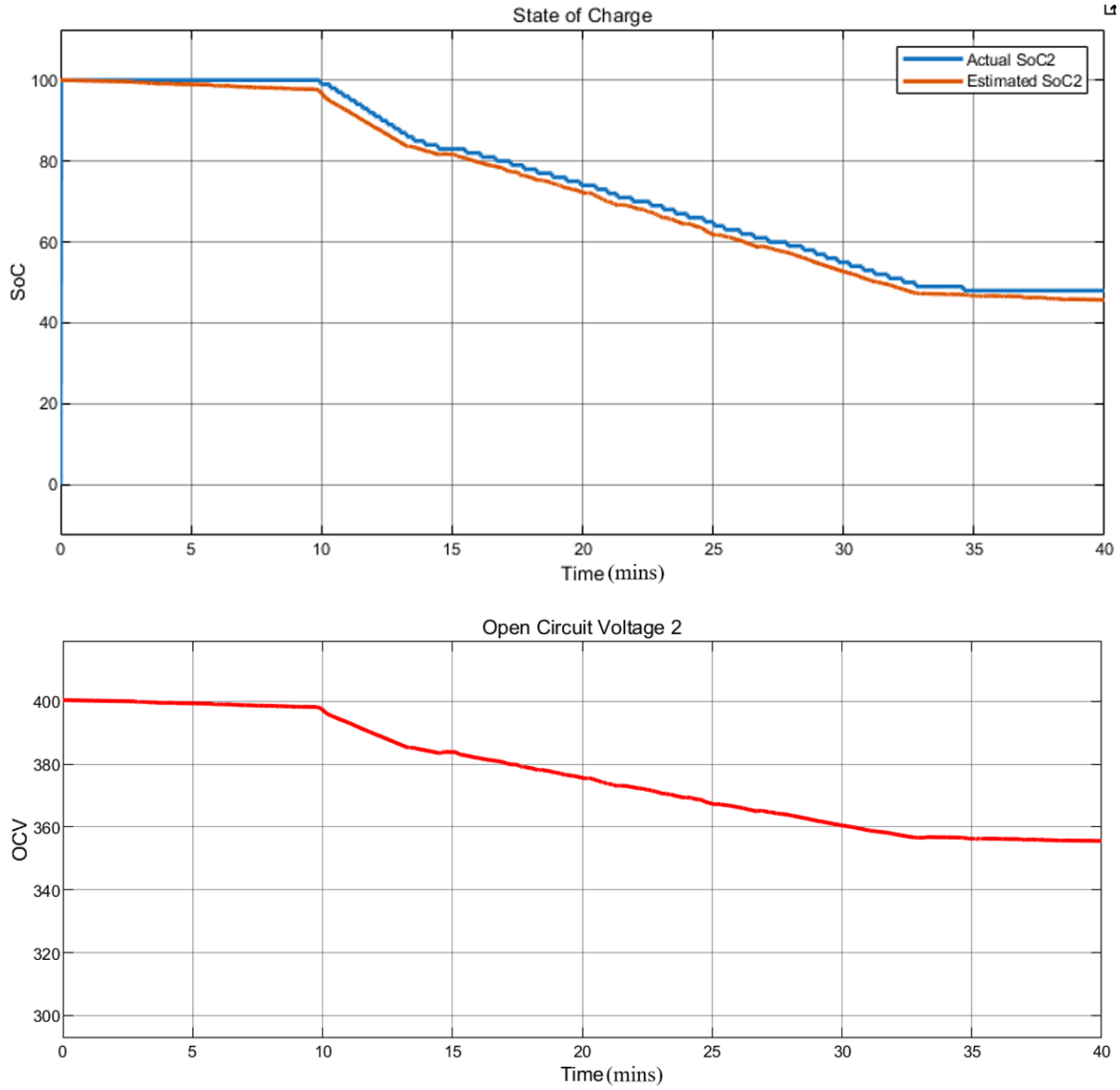


Figure 4.29 SoC and OCV of the rear battery pack for the additional flight mission.

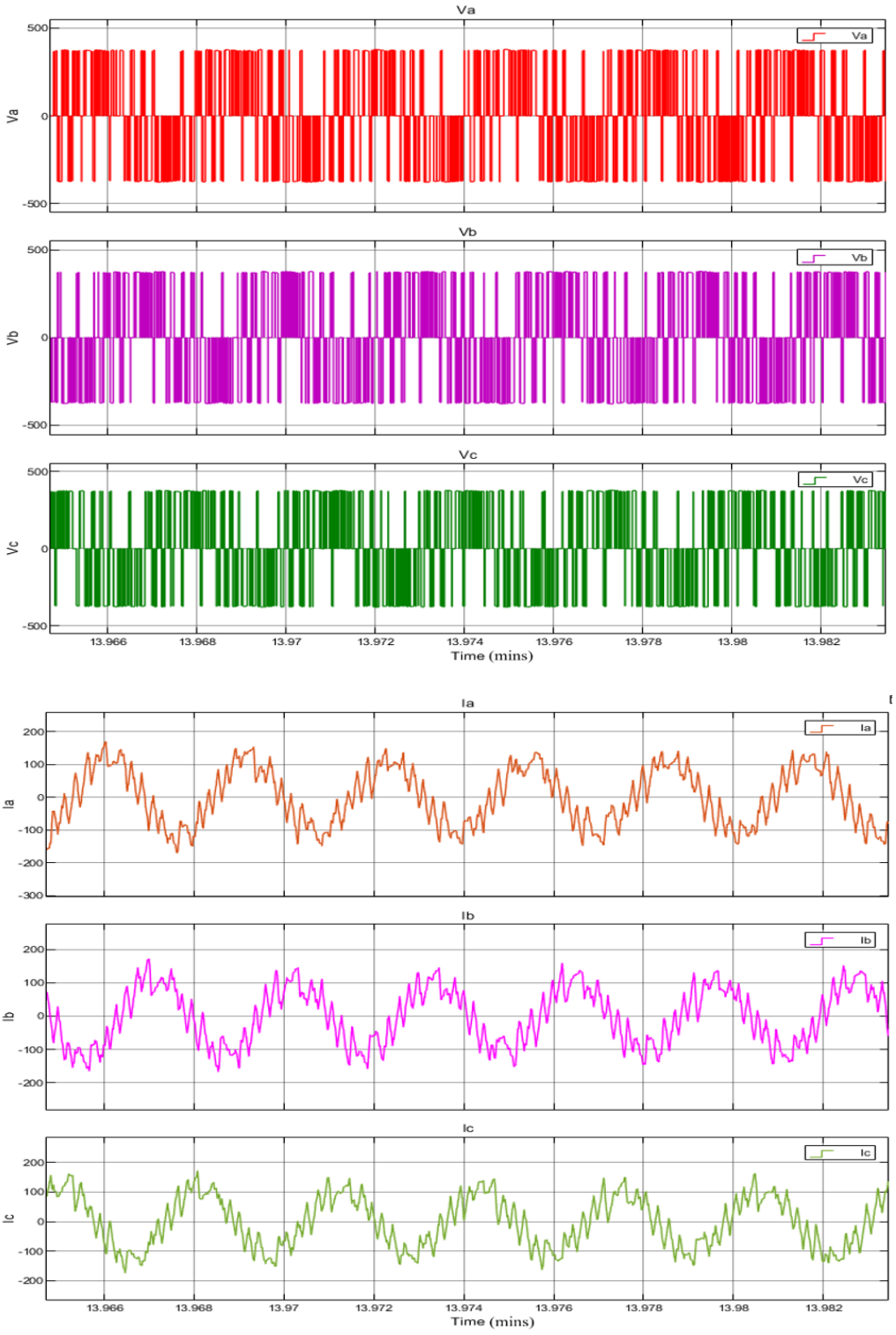


Figure 4.30 Inverter voltages and currents for the additional flight mission.

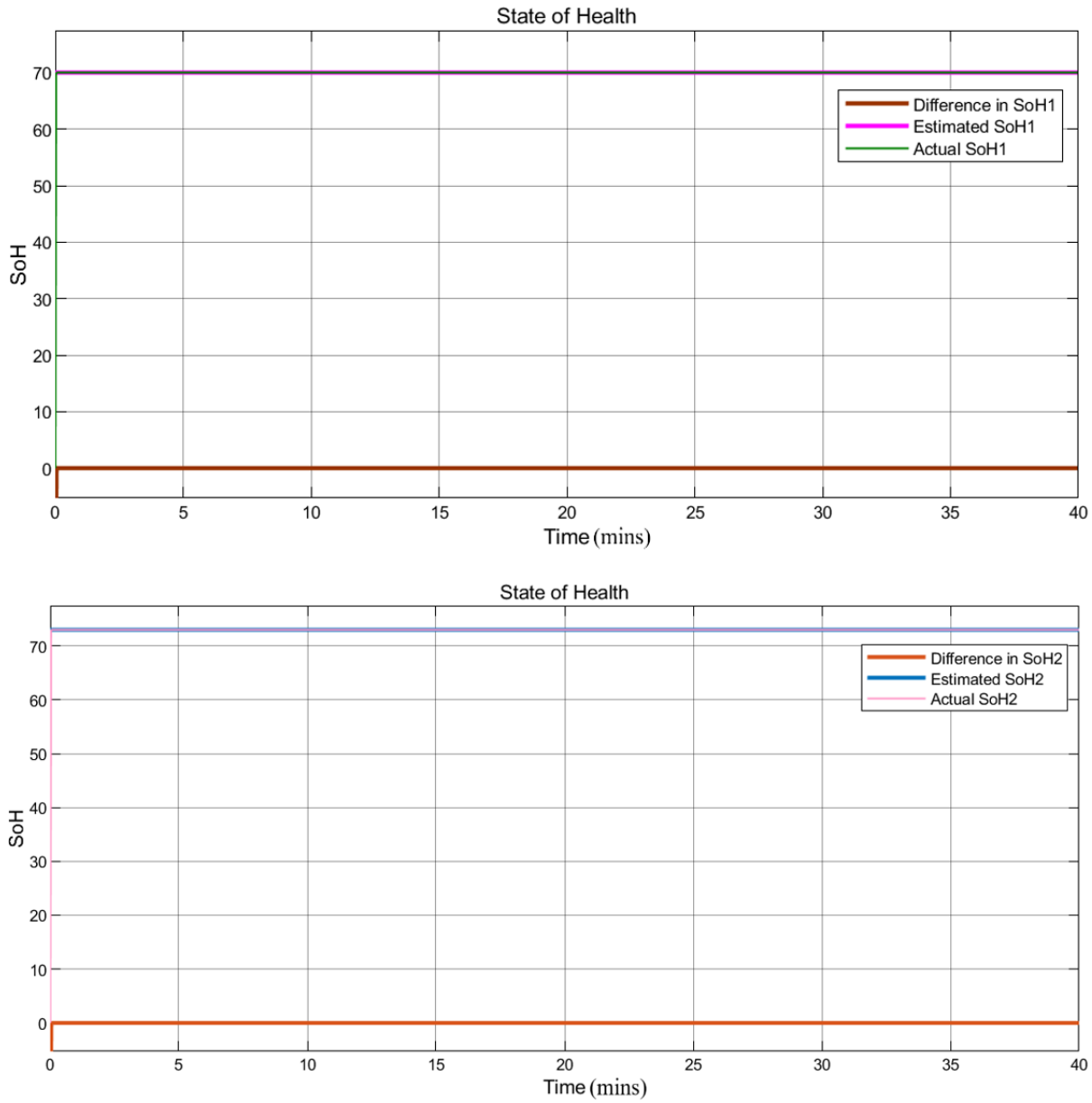


Figure 4.31 SoH profiles of the front and rear battery packs for the additional flight mission.

4.4 Conclusion

This chapter introduced the full electric powertrain model of the Pipistrel Velis Electro and evaluated its behaviour under two operating modes: the autopilot mode, where the speed and torque references are prescribed, and the pilot-controlled mode, where the speed reference is generated from the recorded power command.

The results show that both modes reproduce the aircraft's behaviour with strong agreement to the flight data. In the autopilot mode, the simulated motor responses follow the reference profiles closely, with only brief deviations during rapid transitions. In the pilot-controlled mode, the simulated propeller speed aligns well with the measured values for almost the entire mission, demonstrating that the conversion of pilot power input into a speed reference is similar to how it is done in the actual aircraft and the speed computation method in the glide phase is also accurate.

The battery response also verifies the validity of the model. The estimated state of charge remains very close to the measured SoC throughout the mission, indicating that the SoC estimation method captures the characteristics of the real battery packs. Similarly, the estimated SoH closely follows the actual SoH throughout the mission, indicating that the evaluation method is consistent with the observed battery behavior. The inverter voltage and current waveforms exhibit the expected behaviour under space-vector modulation.

For operating points where the motor is required to run above its base speed, field-weakening control can be introduced to extend the speed range. In a PMSM, the air-gap flux is fixed by the rotor magnets; therefore, the only way to reduce the effective flux linkage is producing a demagnetizing effect by applying a negative d-axis current.

Overall, the close correspondence between the simulation results and the flight measurements confirms that the developed powertrain model captures the essential electrical and mechanical behaviour of the Velis Electro and accurately reflects its performance over the entire mission profile.

Chapter 5
Conclusions and Recommendations for Future Work

This chapter makes conclusive remarks on the key findings of the thesis and provides recommendations for future work.

5.1 Conclusions

This thesis presented a modelling approach for a small electric aircraft, the Pipistrel Velis Electro, by combining detailed models of the propeller and electric powertrain. The propeller was represented by its aerodynamic characteristics and coefficient curves, and two methods were proposed for computing the thrust, rotational speed, and torque. In the equations-of-motion (EOM) approach, the aircraft velocity, altitude, and orientation angles were used as inputs, whereas in the motor power command (MPC) approach, the pilot throttle power command, aircraft velocity, and altitude were used as inputs. Both approaches employed flight phase detection based on aircraft altitude and velocity to distinguish between the different stages of the mission and to compute the corresponding quantities for each phase.

The EOM-based approach was validated using a normal 37-minute flight mission; however, it exhibited oscillations, and some estimated regions did not fully align with the actual data. The MPC approach showed promising results, with more than 90% accuracy when compared with the measured data for the same normal flight mission profile as well as for a touch-and-go mission. The outputs of the MPC approach were used as references for the powertrain control system. The powertrain was simulated for both autopilot and pilot-controlled modes of operation. Although autopilot operation is not available in the Velis Electro, this case was studied for research purposes. In both modes, the simulated motor speed and torque were able to track the corresponding references high precision.

The battery model successfully reproduced the evolution of the state of charge, and the results showed strong agreement with the actual flight data. This indicates that the proposed model is capable of capturing the electrical behaviour of the propulsion system and accurately reflecting the overall performance of the aircraft during the mission. The developed model can therefore be used to conduct various studies, such as battery usage, motor behaviour, and propeller response for different mission profiles, and can serve as a reliable resource for evaluating the forecasted/expected aircraft performance prior to flight.

5.2 Recommendations for Future Work

- Although regeneration is currently disabled in the Pipistrel Velis Electro, harnessing the propeller windmilling energy during unpowered phases of flight, such as gliding, presents a potential opportunity for energy recovery and efficiency improvement. The developed simulation models can be used to analyze this operating scenario in detail and to study the battery behaviour under regenerative conditions. This can help assess the feasibility of controlled regeneration in future aircraft designs and evaluate its impacts on the battery performance, safety, and overall energy efficiency.
- The modelling approach can also be applied to study battery operation under different flight profiles and to optimize these profiles for improved battery utilization and extended flight range. By analyzing the battery current, voltage, and state of charge across various flight missions, the model can support more efficient mission planning and contribute to enhanced operational performance.
- Furthermore, since sufficient flight mission data are available, machine learning and neural-network-based methods can be explored in future work to learn about the patterns and relationships within the flight data. Such data-driven models can be used alongside the physics-based approach to provide fast approximations of certain system behaviors, help identify trends, and support tasks such as fault detection, parameter estimation, and mission prediction.

References

[1] H. Ritchie, "What share of global CO_2 emissions come from aviation?," *Our World in Data*, Oct. 2020. [Online]. Available: https://ourworldindata.org/global-aviation-emissions [Accessed: Mar. 25, 2025].

[2] U.S. Environmental Protection Agency, "Control of Air Pollution From Airplanes and Airplane Engines: GHG Emission Standards and Test Procedures," *Federal Register*, vol. 86, no. 6, pp. 2136–2161, Jan. 11, 2021. [Online]. Available: https://www.federalregister.gov/documents/2021/01/11/2020-28882 [Accessed: Mar. 25, 2025].

[3] International Civil Aviation Organization (ICAO), "CORSIA – Carbon Offsetting and Reduction Scheme for International Aviation," 2023. [Online]. Available: https://www.icao.int/environmental-protection/CORSIA/Pages/default.aspx [Accessed: Jul. 01, 2025].

[4] International Civil Aviation Organization (ICAO), "Aircraft CO_2 Emissions Standard," 2017. [Online]. Available: https://www.icao.int/environmental-protection/Pages/CO2-Standard.aspx [Accessed: Jul. 01, 2025].

[5] European Commission, "Aviation and the EU ETS," *Climate Action*, 2024. [Online]. Available: https://climate.ec.europa.eu/eu-action/transport-emissions/reducing-emissions-aviation/aviation-and-eu-ets_en [Accessed: Jul. 01, 2025].

[6] European Commission, "Fit for 55: Delivering the EU's 2030 Climate Target on the Way to Climate Neutrality," *European Green Deal Policy Package*, Jul. 2021. [Online]. Available: https://ec.europa.eu/info/sites/default/files/chapeau_communication.pdf [Accessed: Jul. 01, 2025].

[7] J. Benzaquen, J. He, and B. Mirafzal, "Toward more electric powertrains in aircraft: Technical challenges and advancements," *CES Transactions on Electrical Machines and Systems*, vol. 5, no. 3, pp. 177–193, Sep. 2021, doi: 10.30941/CESTEMS.2021.00022.

[8] M. T. Fard, J. He, H. Huang, and Y. Cao, "Aircraft Distributed Electric Propulsion Technologies—A Review," *IEEE Transactions on Transportation Electrification*, vol. 8, no. 4, pp. 4067–4090, Dec. 2022, doi: 10.1109/TTE.2022.3197332.

[9] P. Thalin, R. Rajamani, J.-C. Maré, and S. Taubert, “Introduction and a Brief History of Electric Aircraft,” in *Fundamentals of Electric Aircraft: Revised Edition*, SAE International, 2023, pp. 1–11.

[10] K. Rajashekara, “Power Electronics for More Electric Aircraft,” in *Power Electronics for Renewable Energy Systems, Transportation and Industrial Applications*, Wiley, 2014, pp. 365–373.

[11] M. I. Alam, Z. W. Thu, N. Nguyen, M. Tyan, and J.-W. Lee, “Integrated Propulsion System Analysis Framework for designing Advanced Air Mobility Aircraft,” *IEEE Transactions on Transportation Electrification*, vol. 10, no. 4, pp. 10219–10238, Dec. 2024.

[12] P. Thalin, “Aircraft Applications—Part II: Hybrid-Electric Propulsion,” in *Fundamentals of Electric Aircraft*, SAE International, 2023, pp. 181–184.

[13] P. Thalin and S. Taubert, “Aircraft Applications—Part I: Electric Propulsion and Electric Taxiing,” in *Fundamentals of Electric Aircraft*, SAE International, 2023, pp. 153–157.

[14] P. Thalin et al., “Battery Electric Propulsion—Small General Aviation,” in *Fundamentals of Electric Aircraft*, SAE International, 2023, pp. 153–156.

[15] D. Lawhorn, V. Rallabandi, and D. M. Ionel, “Electric Aircraft System Co-Simulation Including Body, Propeller, Propulsion, and Energy Storage Models,” *2019 IEEE Transportation Electrification Conference and Expo (ITEC)*, Detroit, MI, 2019, pp. 1–5, doi: 10.1109/ITEC.2019.8790529.

[16] E. Fornaro, M. Cardone, V. D’Agostino, and A. Dannier, “An Aircraft Hybrid Electric Propulsion Model Experimentally Validated,” *2024 International Symposium on Power Electronics, Electrical Drives, Automation and Motion (SPEEDAM)*, Napoli, Italy, 2024, pp. 1197–1203, doi: 10.1109/SPEEDAM61530.2024.10609099.

[17] Y. Liang, D. Bodnár, G. R. C. Mouli, D. Ragni, and P. Bauer, “Charging Demand Prediction: Small All-Electric Aircraft and Electric Vertical Takeoff and Landing Aircraft,” *IEEE Transactions on Transportation Electrification*, vol. 11, no. 1, pp. 2732–2747, Feb. 2025, doi: 10.1109/TTE.2024.3427841.

[18] S. M. Beedie, C. M. Harris, J. A. Verberne, C. Y. Justin, and D. Mavris, "Modeling Framework for Identification and Analysis of Key Metrics for Trajectory Energy Management of Electric Aircraft," *AIAA AVIATION 2021 FORUM*, Jul. 2021, doi: 10.2514/6.2021-3171.

[19] B. Sarlioglu and C. T. Morris, "More Electric Aircraft: Review, Challenges, and Opportunities for Commercial Transport Aircraft," *IEEE Trans. Transp. Electrific.*, vol. 1, no. 1, pp. 54–64, Jun. 2015, doi: 10.1109/TTE.2015.2426499.

[20] P. Thalin, R. Rajamani, J.-C. Maré, and S. Taubert, "Introduction and a Brief History of Electric Aircraft," in *Fundamentals of Electric Aircraft: Revised Edition*, SAE International, 2023

[21] G. Buticchi, P. Wheeler, and D. Boroyevich, "The More-Electric Aircraft and Beyond," *Proc. IEEE*, vol. 111, no. 4, pp. 355–373, Apr. 2023, doi: 10.1109/JPROC.2023.3236470.

[22] R. Rajamani and P. Thalin, *Fundamentals of Electric Aircraft, Revised Edition*. Warrendale, PA, USA: SAE International, 2023.

[23] S. Sahoo, X. Zhao, and K. Kyprianidis, "A Review of Concepts, Benefits, and Challenges for Future Electrical Propulsion-Based Aircraft," *Aerospace*, vol. 7, no. 4, Art. no. 44, Apr. 2020, doi: 10.3390/aerospace7040044.

[24] K. Dahal, S. Brynolf, C. Xisto, J. Hansson, M. Grahn, T. Grönstedt, and M. Lehtveer, "Techno-Economic Review of alternative fuels and propulsion systems for the Aviation Sector," *Renewable and Sustainable Energy Reviews*, vol. 151, p. 111564, Nov. 2021.

[25] J. Shi, J. Zhou, and L. Wu, "Aerodynamic investigation of a general aviation aircraft with distributed electric propulsion," *2021 IEEE International Conference on Advances in Electrical Engineering and Computer Applications (AEECA)*, pp. 672–676, Aug. 2021.

[26] H. Benyamen and S. Keshmiri, "Flight test validation verification of @AIR Distributed Electric Propulsion Aircraft Dynamic model," *2022 International Conference on Unmanned Aircraft Systems (ICUAS)*, pp. 821–830, Jun. 2022.

[27] M. M. Rivera and L. B. Gutierrez, "Dynamic model of an aircraft propulsion system with electric motor and propeller," *2021 IEEE 5th Colombian Conference on Automatic Control (CCAC)*, pp. 157–162, Oct. 2021.

[28] S. V. Serokhvostov and T. E. Churkina, "One useful propeller mathematical model for MAV," *Proceedings of the International Micro Air Vehicles Conference 2011 Summer Edition*, pp. 108–114, 2011.

[29] K. Takahashi, H. Fujimoto, Y. Hori, H. Kobayashi, and A. Nishizawa, “Modeling of propeller electric airplane and thrust control using advantage of electric motor,” *2014 IEEE 13th International Workshop on Advanced Motion Control (AMC)*, pp. 482–487, Mar. 2014.

[30] T. Niinomi, H. Fujimoto, Y. Watanabe, A. Nishizawa, and H. Kobayashi, “Total thrust control method with propeller and electrically driven wheel for electric aircraft,” *2018 IEEE 15th International Workshop on Advanced Motion Control (AMC)*, pp. 281–286, Mar. 2018.

[31] K. Biber, “Flight Dynamics Modeling of a propeller-driven cargo airplane,” *54th AIAA Aerospace Sciences Meeting*, Jan. 2016.

[32] S. Tedeschini, S. Mohamadian, and C. Cecati, “A multi-phase multilevel powertrain for full electric aircraft,” *IECON 2021 – 47th Annual Conference of the IEEE Industrial Electronics Society*, pp. 1–6, Oct. 2021.

[33] Y. Ding, X. Zhang, B. Li, G. H, W. Fan, F. Luo, B. Hai, and Q. Zhao, “Modeling of a permanent magnet synchronous motor for an aircraft based on Simulink,” *IET Conference Proceedings*, vol. 2024, no. 13, pp. 954–961, Jan. 2025.

[34] M. Porru, A. Serpi, A. Floris, and A. Damiano, “Modelling and real-time simulations of electric propulsion systems,” *2016 International Conference on Electrical Systems for Aircraft, Railway, Ship Propulsion and Road Vehicles & International Transportation Electrification Conference (ESARS-ITEC)*, pp. 1–6, Nov. 2016.

[35] G. Ariante, U. Papa, S. Ponte, and G. Del Core, “Velocity and attitude estimation of a small unmanned aircraft with micro pitot tube and inertial measurement unit (IMU),” *2020 IEEE 7th International Workshop on Metrology for AeroSpace (MetroAeroSpace)*, pp. 314–318, Jun. 2020.

[36] T. Yu, H. Bai, Y. Huangfu, P. Li, W. Shi, and Z. Zhang, “System-level modeling and Energy Management Strategy Design for fuel cell electric aircraft,” *2022 IEEE Transportation Electrification Conference & Expo (ITEC)*, pp. 1070–1075, Jun. 2022.

[37] R. M. Figueiredo, “Aircraft electric propulsion systems: Alternative energy storage and electric motors,” *M.S. thesis*, Dept. of Electrical and Computer Engineering, Universidade de Lisboa, Lisbon, Portugal, Nov. 2022.

[38] R. H. Kersjes, “Dual-DC-port inverter for a fuel cell electric aircraft,” *M.Sc. thesis*, Faculty of Electrical Engineering, Mathematics and Computer Science, University of Twente, Enschede, The Netherlands, Sept. 2023.

[39] M. Wilde, B. Kish, C. Y. Justin, and J. Merkt, “Trajectory energy management systems for EVTOL Vehicles: Modeling, simulation and testing,” *AIAA AVIATION 2022 Forum*, Jun. 2022.

[40] R. D. Falck, J. Chin, S. L. Schnulo, J. M. Burt, and J. S. Gray, “Trajectory optimization of electric aircraft subject to subsystem thermal constraints,” *18th AIAA/ISSMO Multidisciplinary Analysis and Optimization Conference*, Jun. 2017.

[41] J. D. Anderson, “Three-Dimensional Incompressible Flow,” in *Fundamentals of Aerodynamics*, 6th ed, McGraw-Hill Education, 2017, p. 515.

[42] T. R. Yechout, S. L. Morris, D. E. Bossert, and W. F. Hallgren, “Aircraft Equations of Motion,” in *Introduction to Aircraft Flight Mechanics: Performance, Static Stability, Dynamic Stability, and Classical Feedback Control*. Reston, VA, USA: American Institute of Aeronautics and Astronautics, 2003, p. 145.

[43] T. R. Yechout, S. L. Morris, D. E. Bossert, and W. F. Hallgren, “Aircraft Equations of Motion,” in *Introduction to Aircraft Flight Mechanics: Performance, Static Stability, Dynamic Stability, and Classical Feedback Control*. Reston, VA, USA: American Institute of Aeronautics and Astronautics, 2003, pp. 148–150.

[44] T. R. Yechout, S. L. Morris, D. E. Bossert, and W. F. Hallgren, “Aircraft Equations of Motion,” in *Introduction to Aircraft Flight Mechanics: Performance, Static Stability, Dynamic Stability, and Classical Feedback Control*. Reston, VA, USA: American Institute of Aeronautics and Astronautics, 2003, p. 147.

[45] T. R. Yechout, S. L. Morris, D. E. Bossert, and W. F. Hallgren, “Aircraft Equations of Motion,” in *Introduction to Aircraft Flight Mechanics: Performance, Static Stability, Dynamic Stability, and Classical Feedback Control*. Reston, VA, USA: American Institute of Aeronautics and Astronautics, 2003, pp. 153–155.

[46] T. R. Yechout, S. L. Morris, D. E. Bossert, and W. F. Hallgren, “Aircraft Equations of Motion,” in *Introduction to Aircraft Flight Mechanics: Performance, Static Stability, Dynamic Stability, and Classical Feedback Control*. Reston, VA, USA: American Institute of Aeronautics and Astronautics, 2003, pp. 160–163.

[47] B. W. McCormick, "Propeller Analysis," in Aerodynamics, Aeronautics and Flight Mechanics, 2nd ed., Toronto, ON, Canada: John Wiley & Sons, Inc., 1995.

[48] A. L. Andwan, “Characterizing Climb and Propeller Performance for a Fixed pitch, Single-Engine, Electric Aircraft,” thesis, Florida Institute of Technology, Melbourne, Florida, 2022.

[49] D. Ingraham and R. D. Falck, “Blade and takeoff trajectory optimization of a propeller-driven electric aircraft with acoustic constraints,” AIAA SCITECH 2025 Forum, Jan. 2025.

[50] Pipistrel Aircraft, Velis Electro Pilot’s Operating Handbook, Document No. POH-128-00-40-001, Rev. 0, Jun. 10, 2020.

[51] R. H. Kersjes, “Dual-DC-port inverter for a fuel cell electric aircraft,” M.Sc. thesis, Faculty of Electrical Engineering, Mathematics and Computer Science, University of Twente, Enschede, The Netherlands, Sept. 2023.

[52] R. Krishnan, “Chapter 3: Dynamic Modeling of Permanent Magnet Synchronous Machines,” in *Permanent Magnet Synchronous and Brushless DC Motor Drives*, 2nd ed., Boca Raton, Florida: CRC Press, 2010, pp. 242–248.

[53] R. Krishnan, “Chapter 3: Dynamic Modeling of Permanent Magnet Synchronous Machines,” in *Permanent Magnet Synchronous and Brushless DC Motor Drives*, 2nd ed., Boca Raton, Florida: CRC Press, 2010, pp. 225–239.

[54] A. Abuaish, “Assessment of Battery Capacity Fading in Partially-Decoupled Battery–Supercapacitor Hybrid Energy Storage System Topologies for Electric Vehicles”, M.A.Sc. thesis, Department of Electrical and Computer Engineering, University of Waterloo, Waterloo, ON, Canada, 2016.